8-1-2018

Characterizing Targeted Therapeutic Delivery and Cellular Dynamics using In Vitro Cancer Disease Models

Christopher George Uhl
Lehigh University, cguhl@rcn.com

Recommended Citation

Uhl, Christopher George, "Characterizing Targeted Therapeutic Delivery and Cellular Dynamics using In Vitro Cancer Disease Models" (2018). *Theses and Dissertations*. 4326.
https://preserve.lehigh.edu/etd/4326

Characterizing Targeted Therapeutic Delivery and Cellular Dynamics using *In Vitro* Cancer Disease Models

by

Christopher Uhl

A Dissertation
Presented to the Graduate and Research Committee
of Lehigh University
in Candidacy for the Degree of
Doctor of Philosophy

in

Bioengineering

Lehigh University

August 2018

Approved and recommended for acceptance as a dissertation in partial fulfillment of the requirements for the degree of Doctor of Philosophy in Bioengineering.

Student: Christopher Uhl

Dissertation Title: Characterizing Targeted Therapeutic Delivery and Cellular Dynamics using *In Vitro* Cancer Disease Models

Date

Yaling Liu, Dissertation Advisor and Committee Chairman

Accepted Date

Committee Members:

Xuanhong Cheng

Sabrina Jedlicka

Linda Lowe-Krentz

Acknowledgement

Upon reflection, the road leading to my PhD degree was filled with times of struggle and triumph. Throughout the journey, I have had the wonderful opportunity to meet, work with, and befriend many amazing people who have helped me along in many different ways and deserve recognition and thanks.

First and foremost, I would like to thank my advisor, Dr. Yaling Liu who provided me the opportunity to pursue my PhD. His expectations of excellence and his scientific foresight provided motivation and support throughout my time at Lehigh while always ensuring that my work provided meaningful result for practical real-world applications. Again, I would like to thank him for his support and for all of the wonderful experiences that have resulted from my time at Lehigh.

Besides my advisor, I would like to thank the rest of my dissertation committee: Dr. Xuanhong Cheng, Dr. Sabrina Jedlicka, and Dr. Linda Lowe-Krentz, for their support and insightful suggestions that widened my scientific perspective and improved my research endeavors. In addition, I would like to extend many thanks to Dr. Susan Perry for all of her help and guidance throughout my PhD and for all of the fun-filled student picnics and gatherings.

Next to all of my peers, colleagues and friends at Lehigh University, I have enjoyed the times we have all spent together and will cherish them forever. Thank you all for the happy times we have spent over the past 5 years and for all of the support and motivation. Special thanks to Dr. Wentao Shi for all of his suggestions and help related to both research and life outside of the lab. Thanks also to all of my previous labmates, Dr. Ran He for his suggestions and good times in the lab, Dr. Jifu Tan, Dr. Shunqiang Wang, Dr. Salman Sohrabi, Dr. Doruk Yunus, Dr. Antony Thomas, Dr. Jia Hu, Yuyuan Zhou, Shen Wang, and Meghdad Razizadeh for all of their help throughout my time at Lehigh. I will always hold the times we have spent together in warm regards forever. Outside of the lab, I would like to thank Dr. Robert Becker, Andrew Glaser, Dr. Vladimir Muzykantov, and everyone who I have worked in collaboration with on my various research efforts throughout the years. In addition, I would like to thank all of the staff and administration of the BioEngineering Department for their continuous support throughout my journey.

Last but certainly not least, I would like to dedicate this dissertation to my family including my mother, Melinda Uhl, my brother, Austin Uhl, my dog, Benny Uhl, and my father, Bruce Uhl who I know is always watching over me in spirit. It was all of you along with all of my other family and friends who supported me unconditionally throughout all of the high and low times during my PhD. I thank you all for helping to carry me through and for celebrating the successes which you all have been such a large part of over the past 5 years. I am forever grateful for all that you have done for me.

Contents

List of Tables

List of Figures

Abstract

Cancer is a significant health risk to people living in developed and developing countries, which continues to prove difficult to treat. Common treatment options of cancers include surgical removal, radiation, and chemotherapies, which are often used in combination to improve the likelihood of successful treatment. Such combinatory approaches towards treatment are often taken because each approach is not targeted enough to function perfectly on its own. Being able to delivery therapeutic loads in a more targeted manner to sites of cancer has the capability of improving therapeutic efficiency and improving patient responses. The development of improved therapeutic delivery vehicles and screening systems can help serve the goal of improved targeted therapeutic delivery. The use of microfluidic devices for the study of therapeutic delivery has become popular over the past few decades because of the many benefits that they offer. Specifically, microfluidic devices only require small volumes of therapeutics for testing, which is often ideal because of limited drug supply during screening. Additionally, the high degree of control over channel geometries, ease of fabrication and low cost make microfluidic therapeutic testing devices well suited for higher throughput screening when run together in parallel. The ability to generate shear flow within the microfluidic channels also offers a means of more closely mimicking vascular physiology and conditions that would be experienced during drug delivery in the human body. Lastly, the use of microfluidic in therapeutic testing enables micro-scale data on characteristics such as binding, uptake, cellular permeability and others to be easily collected due to the transparent nature of the devices and ability to facilitate cell cultures. As such, the focus of this dissertation is mainly based around the establishment of microfluidic systems capable of mimicking

cancerous environments and testing of various therapeutic vehicles and delivery methods targeted for cancer. In brief, the dissertation demonstrates a few methods of establishing cancerous environments within microfluidic systems of increasing complexity, and how screening of various nanoparticle vehicles and therapeutics is performed.

First, a single layer microfluidic device is developed to facilitate the growth of cancer monolayers for the screening of solid lipid nanoparticle drug delivery performance. The device is designed to assist in identifying an optimal ratio of antibody to polymer chains exposed on the surface of the nanoparticles. Improved targeting of nanoparticles to cancer cells is achieved by increasing target specific binding through addition of cancer antibody while reducing non-specific binding through addition of polymer chains on the nanoparticles surface. Conditions for optimal targeting specifically to cancer cells were identified for nanoparticles with 37% of their surface area occupied by polyethelyene glycol (PEG). The cancer cell targeting efficiency for the 37% coated nanoparticles was determined to be a maximum of 81% when a cancer specific antibody was used in conjunction on the nanoparticles surface.

Next, to improve the physiological relevance of the microfluidic screening system, a bi-layer setup was fabricated. The nature of the bi-layer device is designed to facilitate the co-culture of cancer and endothelial cells (ECs) in different compartments while still permitting signaling and chemical interactions to occur between the two cell types. The presence of ECs in the device is designed to mimic a blood vessel, as therapeutic delivery within the body relies heavily on the circulatory system from drug transport. As such, understanding the mechanics of therapeutic delivery from mimicked vasculature to cancer is an important consideration. Conditions in the bi-layer system influencing therapeutic transport include endothelial permeability, therapeutic size, system flow rate, and treatment time. Improved therapeutic delivery was achieved using smaller molecules, slower system flow rates, and when the EC monolayer was highly permeabilized. Increased treatment times, resulted in less and less therapeutic transport from the mimicked vessel to the cancer environment as the EC monolayer regained confluency. It was shown that the bi-layer microfluidic system functions to screen therapeutic delivery to a mimicked cancer environment under more physiologically relevant conditions.

The next progression with the system was to test nanoparticle delivery and transport from the mimicked vessel to the cancer environment. This was accomplished utilizing the same bi-layer microfluidic setup in conjunction with a range of nanoparticle shapes that were utilized to identify characteristics that facilitate the greatest degree of therapeutic delivery. Specifically, spherical, short rod and long rod/worm-like nanoparticles were tested for their ability to transport therapeutic loads to the cancer environment over the course of 5 day treatments. Optimal nanoparticle shapes for each flow rate varied based on treatment time. Overall, nanoparticle drug delivery should be varied based on the degree of EC permeability which changes with time as the cancer environment is treated.

Lastly, to improve the physiological relevance of cancer environments being used, a method for establishing and growing tumor spheroids within the microfluidic devices in an expedited fashion was developed. The ability to perform therapeutic and nanoparticle carrier screening on tumor spheroids as opposed to cancer monolayers provides feedback on efficiency and performance which more closely mimics outcomes observed in animal and clinical testing. In addition, the ability to form tumor spheroids in an expedited manner allows the screening process to be completed in a shorter period of time and with fewer initial cells. The use of convective driven nutrient flow is utilized to achieve such expedited cancer growth in a microfluidic system which also has the potential to facilitate therapeutic screening. The system has been shown to function with adherent and non-adherent cell types where 1.5 to 4.5 times faster growth can be achieved. The ability to cut tumor culturing times from 1 week to 3 days and reducing required cell counts from thousands to tens of cells has the potential to save lives in clinical settings when using patient derived samples.

Chapter 1: Introduction

1.1 Background and Motivation

Throughout the world 14.1 million people suffer from cancers of various types as of 2012, with an estimated increase to around 21.3 million by 2030 [1]–[3]. The average survival rate after diagnosis varies based on cancer type and the stage at which the cancer is identified [2], [3]. Due to its large societal impact, research into prevention and treatment of cancers has been the major focus of time, funding and resources by many companies and government institutions [4], [5]. Improving the likelihood of patient survival requires early diagnosis along with rapid development and implementation of treatment plans [2], [3].

The most common treatment plans utilized are classified as excision [6], radiotherapy [7], and chemotherapy [8], or some combination of the three. The first option of excision can function effectively if the cancer is in an early stage and has not yet begun to metastasize [9]. Later stages of cancer where metastasis may have begun to occur require the use of radiotherapy or chemotherapy. The wide use of chemotherapy for cancer treatment is the result of ample therapeutic options which can function on cancers from various tissue origins [7], [8], [10]–[12]. Chemotherapy development is a long and time-consuming process which overall has very low success rates. In addition, the use of *in vitro* and *in vivo* screening is required to identify viable therapeutic candidates [13]–[15]. Such chemotherapeutics can often have adverse side effects on patients, which occurs when the therapeutic agent interacts with healthy tissues within the body [16]–[19]. In an attempt to mitigate this issue, the use of targeted delivery systems such as nanoparticles has been employed to facilitate the treatment of cancers while limiting the occurrence and severity of side effects [16]–[21].

Nanoparticles have long been investigated for their use in therapeutic delivery [16]–[21]. The ability to store therapeutics in the cores of nanoparticles provides a means of securely shielding healthy tissue from adverse side effects [16]–[21]. This feature coupled with the ability to modify the surface chemistry of nanoparticles with proteins, antibodies and polymer coatings allows for targeted delivery specifically to diseased sites within the body [1]–[16]. The ability to fine tune nanoparticle characteristics such as shape, size, surface composition, surface charge, and dug release mechanism make nanoparticles well suited for targeted therapeutic delivery [32], [33]. However, such fine-tuning of nanoparticle performance requires intensive testing and screening within vasculature and disease microenvironments [17], [29], [32]–[35]. Testing on such a scale purely in traditional *in vitro* and *in vivo* models makes regular and consistent progress difficult. As such, more novel testing and screening systems are required such as microfluidic platforms [21]–[34].

Microfluidic platforms emerged and gained popularity in the past few decades. Microfluidics have found wide application in many fields including drug discovery, advanced cell growth, chemical synthesis, biomolecular analytics, environmental screening and many other [44], [50]–[54]. The use of microfluidics in many applications arises from their low costs to produce, small sample and reagent volume requirements, high degree of control over flow and geometry, ability to achieve concentration gradients, high throughput capabilities and relatively low waste [32], [38], [41]. All of these features make microfluidics ideal for drug screening applications, especially for cancer chemotherapeutics [47]. In particular, the requirement of small therapeutic sample sizes, ability to facilitate 3D *in vitro* cancer growth and ability to facilitate high throughput screening make microfluidics well suited for tumor microenvironment therapeutic screening and analysis [14], [15].

A wide range of organ-mimicking microfluidic systems have previously been developed for therapeutic screening [47], [49], [63]–[72], [55], [73]–[79], [56]–[62]. These organ-mimicking microfluidic system have been termed organ-on-chip (OOC) systems and are designed to capture many of the key characteristics of the specific organ being mimicked which are relevant to the function and delivery of therapeutics [36], [48], [80], [81],[47], [49], [63]–[72], [55], [73]–[79], [56]–[62]. Introduction of OOC systems engineered to enhance the predictive capabilities of *in vitro* drug performance at an early stage, have attempted to reduce wasted resources and time on non-viable drug candidates [36], [47], [70], [80]–[84], [84], [85], [48], [49], [61], [65]–[69]. Recent advances in OOC systems have mainly focused on mimicking physiologically relevant conditions, experienced within the given organ, which influence drug delivery or performance *in vivo* [55], [58], [82]–[84], [86], [59], [72], [73], [75]–[79]. The organs which often receive the most attention in this field include blood vessels, the lungs, the liver, and tumor environments [47], [49], [63]–[72], [55], [73]–[79], [56]–[62]. Specifically, focus is placed on tumor-on-chip devices and the improvements made for the devices utilized through the research of this dissertation.

Tumor-on-chip systems are often designed to allow for the growth of tumor models in physiologically relevant manners while allowing for the assessment of various therapeutics to observe how effectively they are able to treat the developed cancerous model [62], [65], [87]. Many of the tumor-on-chip devices employ the use of 3D cell culturing techniques to recreate the architecture and structural relations of solid tumors and neighboring tissues such as blood vessels [57]·[47], [59], [60], [63], [88]. Such microfluidic models aim to provide a means of studying certain aspects of treating a cancerous region within a model which is simplified when compared to the *in vivo* environment [47], [61], [63], [64], [88], [89].

There are many approaches adopted by tumor-on-chip devices to grow cancerous cells for various testing applications. Both 2D and 3D models have been developed including, cancer cell sheets, multicellular spheroids, multicellular layers, and hollow fibers, with each offering various advantages and disadvantages [47], [61], [63], [64], [88], [89]. Two dimensional culturing limits the physiological relevance of certain microfluidic systems, however offers improved capabilities when considering direct cellular imaging [60]. Three dimensional growth systems are capable of more accurately recreating tumor architectures and cellular interactions, processes such as imaging and cell maintenance can be troublesome [47], [63], [88]. Examples of some three dimensional growth microfluidic devices involve the capture of cancer cells in isolated regions where 3D spheroid formation can occur over time or through the addition of various growth factors [47], [63], [88]. Microfluidic devices developed by Wu *et al*, Hsiao *et al*, and Ong *et al* have utilized structures designed into the microfluidic devices to capture and retain cancer cells in order to facilitate three dimensional growth [47], [63], [88]. Such systems demonstrate spheroid heterogeneity which is a defining factor of most *in vivo* tumor cases while still allowing for media and therapeutic flow [47], [63], [88]. Flows of single or combinatory therapeutics can be introduced in order to test the effectiveness of treatments. However, despite such capabilities, such models often lack additional biological barriers typically encountered when delivery anti-cancer therapeutics *in vivo* [47], [63], [88]. Incorporation of associated surrounding tissues and vasculature would serve to improve the capabilities and predictive nature of such platforms. It is of course recognized that doing so, often greatly increases the complexity of the system. Despite this drawback, the current systems are capable of quantifying the therapeutic effect on cancerous cells by monitoring cell viability and death, 3D cellular morphology, and protein production (albumin and 4-MUG) [47], [63], [88].

Improved capabilities of such tumor-on-chip microfluidic system would benefit from the addition of common biological barriers encountered during drug delivery to tumor sites *in vivo* such as vascular [47], [59]. In addition, the timeframes required to establish such system for optimized therapeutic analysis need to occur faster in order to facilitate expedited testing. Current microfluidic system often require several days (5-7 days) to achieve tumor spheroids which are ready to be challenged with therapeutics [47], [61], [63], [64], [88], [89]. Achieving similar results in a more expedited fashion would open up the possibilities for use of the microfluidic systems in patient-specific applications where personalized therapeutic treatment options can be explored in order to quickly identify an optimal treatment plan. Early treatment of many cancers *in vivo* in turn would lead to improved patient health and survival. Likewise, the application of physiologically relevant pressure gradients within the microfluidic systems would better mimic the process of delivering therapeutics to cancer microenvironments *in vivo*. As such, the microfluidic systems utilized in this dissertation were developed to incorporate many of these key factors and characteristics lacking in previous research efforts. Specifically, the inclusion of flow, pressure differentials, mimicked vascular barriers in the form of endothelial monolayers, 3D tumor culture, and expedited tumor growth were accomplished in OOC systems in order to improve the screening capabilities of microfluidics. As such, all chapters in this dissertation utilize improved microfluidics for cancer related therapeutic screening applications, with the dissertation and outline to follow.

1.2 Dissertation Layout

Herein, the dissertation layout is organized following the roadmap described below. First, a single layer microfluidic platform is described and used for cancer targeted nanoparticle screening. To further improve the physiological relevance of the microfluidic platform, a bi-layer system is developed to facilitate blood vessel and cancer growth for drug delivery studies. Lastly, a method is developed for producing 3D tumor spheroids in an expedited manner for use in therapeutic screening as opposed to 2D monolayers of cancer cells. In detail, the layout is as follows.

Chapter 1 briefly describes the background and main challenges faced in cancer therapeutic screening, with detailed introductions and motivations presented in each of the following chapters.

Chapter 2 presents a single layer microfluidic platform that facilitates the growth of HCT116 monolayers for cancer targeted nanoparticle binding studies, and the results obtained using various nanoparticle compositions.

Chapter 3 introduces a bi-layer microfluidic platform that facilitates the growth of an endothelial monolayer as a mimicked blood vessel and a monolayer of cancer cells. The assessment of endothelial permeability is conducted and delivery of therapeutics is demonstrated from the mimicked vessel to the mimicked cancer.

Chapter 4 describes the use of the bi-layer microfluidic platform for assessing the delivery capacities of nanoparticle carriers of various shapes in order to achieve improved therapeutic delivery to cancerous microenvironments.

Chapter 5 presents a microfluidic platform and method for the expedited growth of 3D tumor spheroids for use in therapeutic screening on established cell lines and patient derived cancers.

Chapter 6 comprehensively summarizes the dissertation and presents directions for future work.

Chapter 2: Assessment of PEGylated Cancer Targeting Solid Lipid Nanoparticles in a Microfluidic Device

2.1 Introduction

Treatment of diseases with specificity involves delivery of therapeutics strictly to disease sites while preventing therapeutic delivery to non-diseases sites [22], [23], [35], [90]–[94]. Approaching the goal of disease treatment in this manner improves the efficiency with which therapeutics are utilized [22], [23], [35], [90], [91]. Besides being a more efficient use of therapeutic loads, the delivery of therapeutics to non-diseased regions often leads to side effects [27], [90], [95]. Many resulting side effects can often have undesirable influences and in some extreme cases can cause serious injury or even death [27], [90], [95]. In order to achieve the goals of targeted delivery specifically to diseased regions, the use of nanoparticles has been investigated for their ability to sequester therapeutic loads while allowing for surface functionalization with proteins and antibodies [25], [26], [28], [29]. However, such experimental forms of therapeutic delivery cannot be directly tested within human patients. Instead laboratory based models are used as stand-ins for the human circulatory system in which therapeutic tests can be run [25], [26], [28], [29].

Such testing is often conducted within microfluidic system models in order to facilitate controlled and reproducible testing [24], [45], [96]. In addition, the use of microfluidics often facilitates direct imaging of the system in an easier manner and requires smaller quantities of experimental drug carriers for testing when compared to animal models [97],

[98]. Through the application of microfluidics, nanoparticle testing is possible, with aims of achieving targeted therapeutic delivery. The use of target specific antibodies has been heavily investigated to achieve the goal of targeted nanoparticle delivery to disease sites [30], [31], [99]–[102]. However, while specific binding to targeted antigens can be increased through the use of antibody coated nanoparticles, the ability to actively prevent non-specific binding to non-diseased regions is required [99], [103]–[105]. Many approaches to minimize non-specific binding of therapeutic carriers are documented in literature, with emphasis typically placed on alterations to nanoparticle surface chemistry and charge [30], [99], [103]–[105].

One particular approach utilized to reduce non-specific binding has been demonstrated through the use of chain polymer coatings on the outer surfaces of particles [103]–[108]. Specifically, the use of polyethylene glycol (PEG) has shown promising results in literature to help reduce unwanted binding [103], [104], [106], [108]. Previous studies have also shown that the presence of PEG and target specific antibodies can function to improve target specific binding and absorbance [109]–[111]. Examples include the use of PEG linkers with antibodies targeted for prostate-specific membrane antigen on the surface of quantum dots, which functioned to improve the delivery of the quantum dots to cancerous cells in *in vitro* and *in vivo* experiments [110]. Besides improved target specific binding, the inclusion of PEG and target antibodies of the surface of nanoparticles have been shown to improve the circulation time of the particles in *in vivo* experiments run in mice [109], [111]. Specifically, the presence of PEG on the surface of gold nanoparticles was demonstrated to elongate the circulation time of the nanoparticles in blood plasma for over 8 days compared to less than one day for non-coated gold nanoparticles [109], [111].

Lastly, the coating of PEG onto the surface of silica nanoparticles was shown to reduce aggregation by increasing the shear plane because of steric hindrance-based stabilization [103]. Such reduced aggregation of nanoparticles in turn assists in reduced clearance from the blood plasma *in vivo*. However, despite all of this work there has been little research designed to investigate how to balance the effects of antigen specific binding achieved with antibodies and the inhibition of non-specific binding achieved with the application of PEG.

In this study, we utilize a microfluidic platform that is capable of accommodating cancer cell growth. In conjunction with the microfluidic system, solid lipid nanoparticles (SLNP) are utilized to investigate the influence of various coating ratios of specific antibody (anti-EpCAM) and PEG on the ability to deliver therapeutics to cancerous cells in a targeted manner. The application of the microfluidic system developed in this study for investigating the kinetics of SLNP binding to cancer cells provides a means of controlling the shear forces applied on the particles which is difficult to finely control in traditional experimental setups such as static culture dishes or well plates. In addition, the system provides a cell and non-cell coated surfaces within the same channel that in turn can provide control (non-cell coated) and experimental (cell coated) conditions for simultaneous testing and data collection. Through this work, a suitable range of PEG and anti-EpCAM surface coatings are identified which enhance the ability of the SLNPs to deliver therapeutic payloads in a targeted manner while minimizing unwanted non-specific delivery.

2.2 Experimental

2.2.1 Materials

The media used for HCT116 cells was Dulbecco's Modified Eagle's Medium (DMEM, Life Technology), with 10% fetal bovine serum (FBS, Invitrogen) and 1% Antibiotic & Antimycotic (ThermoFisher). CellTracker Green was used to fluorescently label cells (ThermoFisher). Microfluidic molds were digitally cut from printable gold foil sheet (Silhouette) with Silhouette SD digital cutter (Silhouette). Microfluidic devices were produced from Sylgard 184 polydimethylsiloxane (PDMS) (Dow Corning) and microscope cover glass slides (FisherBrand). SLNPs were produced that contained PEG and anti-EpCAM (diameter 150-200 nm, pyrromethene 567A (Sigma-Aldrich), PEG-12 carnauba (Sigma-Aldrich), Anti-EpCAM (Life Technology), and carnauba wax (Sigma-Aldrich)). Syringe pumps were used for nanoparticle flow tests (Harvard Apparatus). All other reagents not mentioned were used directly without purifying.

2.2.2 Microfluidic device design, fabrication and assembly

Microfluidic devices were fabricated using PDMS and channel molds that were digitally cut into the shape indicated in Fig 2.1(A). The PDMS channels were replicated from the mold in a casting process with a bake at 80^0C for 12 hours. The devices were fabricated using straight channels that were assembled into single layer devices as depicted in Fig 2.1(B). The PDMS pieces received inlet and outlet ports with a biopsy punch and were bound to glass slides with a plasma treatment of both surfaces for 5 minutes followed by a bake at 80^0C for 30 minutes to set the bond. The fully assembled devices were visually inspected and run through an autoclave cycle at 125^{0}C for 30 minutes to sterilize prior to receiving cells.

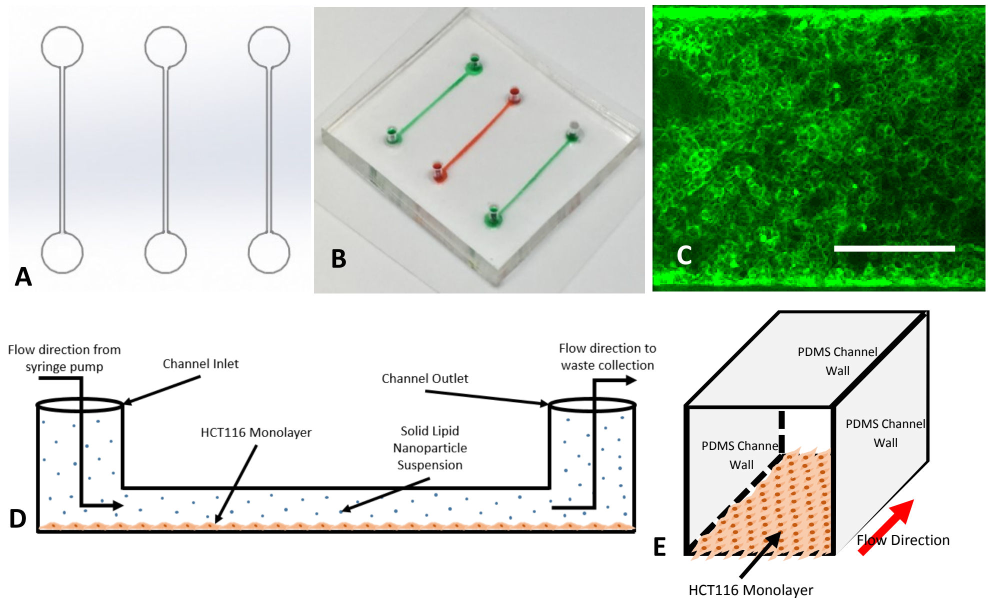

Figure 2.1 Microfluidic device design and function. (A) Microfluidic channel design. (B) Microfluidic device produced with contrast dye flown in channels. (C) Representative fluorescence image of HCT116 cells growing within a device. Scale bar: 250μm (D) Device schema of particle suspension flow tests. (E) Microfluidic channel schema showing which surface of the device facilitates growth of the HCT116 monolayer and which surfaces are exposed PDMS.

2.2.3 Solid lipid nanoparticle fabrication

SLNP fabrication was accomplished through a low-pressure melt-emulsify-chill process. The incorporation of yellow carnauba wax from the *Copernicia prunifera* palm tree(Koster Keunen, Watertown, CT), PEG-12 yellow carnauba wax (Koster Keunen, Watertown, CT), and Pyrromethene 567A (emission wavelength 546nm, Exciton, Dayton, OH) into the SLNPs was accomplished via dispersion into a high temperature aqueous emulsifier solution under controlled shear conditions. A cooling step is then performed in order to stabilize the SLNPs. The resulting SLNP have the oil-soluble fluorescent dye encapsulated within the particles. After filtration, the average SLNP diameter for each batch was measured via dynamic light scattering. Average SLNP diameters were determined to be between 150 to 200nm for each batch made throughout the course of experimental testing using dynamic light scattering as observed in Fig 2.2. The SLNP composition and production process are proprietary information of Particle Sciences, Inc. (Bethlehem, PA).

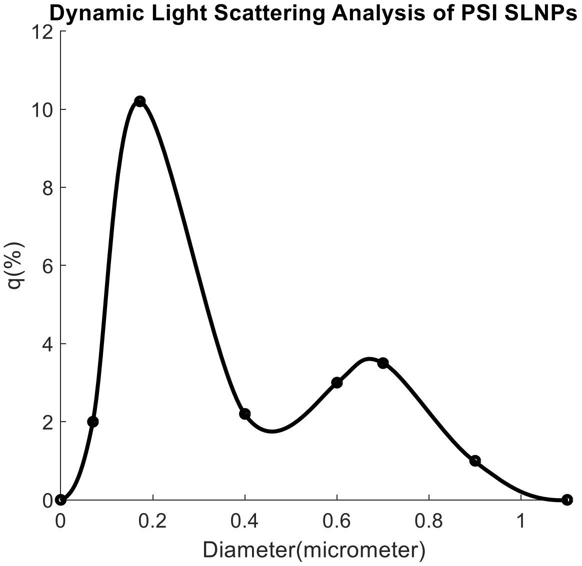

Figure 2.2 Dynamic light scattering analysis of solid lipid nanoparticles. DLS data indicates average SLNP diameters between 150-200nm.

2.2.4 Cell growth and staining

Human colorectal cancer cell line, HCT116, was used as a model cancer in this work. Cultured in 5% CO_2 and at 37 °C, HCT116 cells were incubated with DMEM supplemented with 10% FBS and 1% Antibiotic & Antimycotic. The medium was changed every 2 days. When the cells reached 80-90% confluency, they were subcultured and 0.05% Trypsin - 0.53 mM EDTA was used for cell detachment. Once the cells were collected and the microfluidic device was sterilized, 20 μL of cell suspension was injected and allowed to sit statically under incubated conditions to facilitate cell adhesion within the channel. After 4 hours, PBS was injected into the devices at a flow rate of 200 µL/h to remove any unbound cells. The HCT116 cells were exposed to continuous culture media flow for 4-5 days at a rate of 200 µL/h until fully confluent HCT116 monolayers were formed as seen in Fig. 2.1(C). The confluent monolayers were stained with Cell Tracker Green^{TM} for fluorescence visualization. The stain was produced according to the manufacture's recommendation at a concentration of 10µM and incubated with the cells for 15 minutes prior to starting SLNP flow tests.

2.2.5 Establishing shear rate

The effect of fluid shear on the growth of cells, delivery of fresh nutrients, and particle binding studies was established using syringe pumps (PHD 2000, Harvard Apparatus). The equation governing[112] the shear rate established in each of the channels is as follows: $Shear\ Rate = (\frac{6Q}{W*H^2})(1+\frac{H}{W})(f^*)(\frac{H}{W})$, where Q is the established flow rate within the given channel, W is the channel width, H is the channel height, and f^* is a geometrical factor based on channel dimensions which for the microfluidic devices used is 0.7946. The width and height dimensions for the channels utilized in this study were 500 micrometers and 100 micrometers, respectively. In order to stay within a physiologically relevant range[113]–[115], the shear rates established within the channels for the particle binging studies were held between 200 sec^{-1} and 1600 sec^{-1}. A table showing the tested shear rates and subsequent flow rate, flow durations and total flow volumes can be observed below in Table 2.1.

Table 2.1 Flow testing parameters utilized for various non-specific and specific binding tests.

Non-Specific Binding Tests

Shear Rate (s^{-1})	Flow rate (µL/hr)	Flow Duration (hr)	Total Volume (µL)
200	776.7	~1.29	1000
800	3106.7	~0.32	1000
1600	6213.4	~0.16	1000

Specific Binding Tests

Shear Rate (s^{-1})	Flow rate (µL/hr)	Flow Duration (hr)	Total Volume (µL)
200	776.7	~0.39	300
800	3106.7	~0.10	300
1600	6213.4	~0.05	300

2.2.6 PEG surface area coverage calculations

In order to better understand the influence of the PEG incorporated into the SLNPs, the percentage of the SLNP covered by PEG was determined for each amount of PEG used for testing. The calculations for the surface area coverage was carried out as follows[116], [117]:

$$R_f = b_{exp} \times N_{glycol}^{\frac{3}{5}} \quad (Flory\ radius\ per\ PEG\ chain\ (nm))$$

$$SA_{PEG} = \frac{\pi \times R_f^2}{4} \quad (nm^2\ per\ PEG\ chain)$$

$$SA_{\%} = \frac{V_{\%} \times V_p}{SA_{SLNP}} \quad (\%\ of\ SLNP\ surface\ comprised\ of\ PEG - Carnauba)$$

$$N_{PEG} = SA_{SLNP} \times \frac{SA_{\%}}{100\%} \quad (\#\ PEG\ chains\ on\ SLNP\ surface)$$

$$SAC_{PEG} = \left(\frac{\mathbf{(3)} \times \mathbf{(5)}}{SA_{SLNP}}\right) \times 100\% \quad (\%)$$

Where N_{glycol} is the average number of ethylene glycol units per PEG chain (12-20 ethylene glycol units per chain (avg: 16 units)), b_{exp} is the unit length of one ethylene glycol unit (=0.1nm), R_f is the Flory radius of a single PEG chain on the surface of a SLNP, SA_{PEG} is the surface area of the SLNP occupied by a single PEG chain, $SA_{\%}$ is the percentage of the SLNP surface comprised of PEG-Carnauba units, $V_{\%}$ is the volume percentage of PEG-Carnauba units mixed into each SLNP (values reported from Particle Sciences as indicated in Table 2), V_p is the volume of a SLNP (calculated as volume of a sphere with diameter of 169.5nm), SA_{SLNP} is the total surface area of a SLNP, N_{PEG} is the total number of PEG chains present on the surface of the SLNPs, and SAC_{PEG} is the total percentage of the SLNP surface covered by PEG chains.

Table 2.2 The range of volume percentage of PEG-Carnauba units in each SLNP formulation (first column), reported by Particle Sciences. Corresponding range of surface area percentages covered by PEG on the SLNPs tested (second column). $^{+}$ denotes PEG surface coating percentages tested in first round. * denotes refined range of percentages used in second round of testing.

VOLUME % OF PEG-CARNAUBA UNITS IN SLNPS ($V_{\%}$)	**RANGE OF SLNP SURFACE AREA PERCENTAGES COVERED BY PEG**
0%	0% $^{+}$ *
0.2%	1% $^{+}$
1%	6% $^{+}$ *
2%	12% $^{+}$ *
6%	37% *
12%	74% *
20%	124% $^{+}$ * **(indicated as 100%‡)**

2.2.7 Non-specific SLNP binding

Each of the bare SLNPs was flown through single layer microfluidic devices at varying shear rates. A range of PEG surface coating percentages were tested which included: 0, 1, 6, 12, and 100%[‡] as noted in Table 2.2 above. As noted above in Table 2.1, the shear rates utilized were $200s^{-1}$, $800s^{-1}$, and $1600s^{-1}$. Particle flows were established using a syringe pump for a pre-determined period of time. The total number of particles flown in each test was held constant by varying the duration of the flow to shorter and shorter timeframes as the shear rate utilized increased. This was done to ensure normalized testing conditions across all setups. At the completion of each flow, PBS (1X, Sigma-Aldrich) buffer was flown through the channels to wash away any unbound particles prior to confocal imaging. After washing, confocal scans were made across the entire internal surface of each channel to collect fluorescence intensity data. The scans were then loaded into FIGI (ImageJ)[118], and reconstructed back into a bulk 3D image. Final image processing was carried out to determine the fluorescence intensity of particles bound to the inner walls and cell monolayer of each channel. Comparisons were then made across varying PEG percentages and shear rates as can be seen in Fig 2.3.

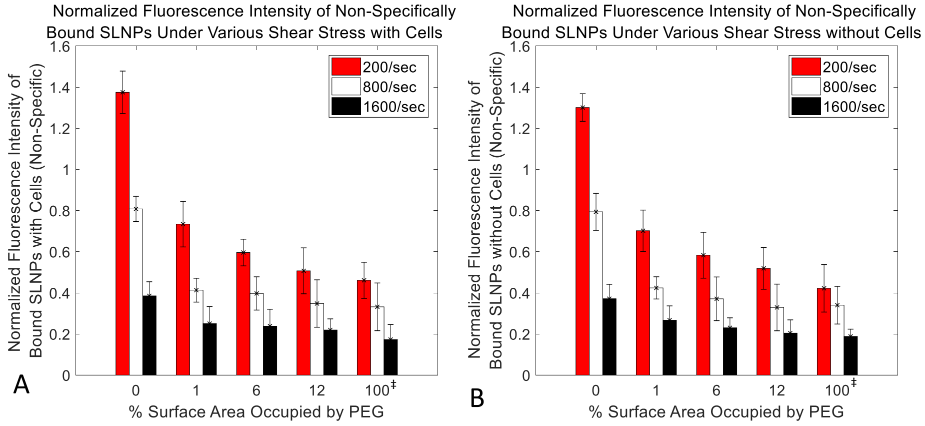

Figure 2.3 Non-specific binding of bare SLNPs at various shear rates. (A) Normalized SLNP binding with HCT116 cell monolayers. (B) Normalized SLNP binding without cells.

2.2.8 Antibody specific SLNP binding

Each of the antibody coated SLNPs was flown through single layer microfluidic devices at varying shear rates. A range of PEG surface coating percentages was tested which included: 0, 1, 6, 12, and 100%‡ as noted in Table 2.2 above. As noted above in Table 2.1, the shear rates utilized were 200s^{-1}, 800s^{-1}, and 1600s^{-1}. Particle flows were established using a syringe pump for a pre-determined period of time. The total number of particles flown in each test was held constant by varying the duration of the flow to shorter and shorter timeframes as the shear rate utilized increased. This was done to ensure normalized testing conditions across all setups. At the completion of each flow, PBS (1X, Sigma-Aldrich) buffer was flown through the channels to wash away any unbound particles prior to confocal imaging. After washing, confocal scans were made across the entire internal surface of each channel to collect fluorescence intensity data. The scans were then loaded into FIGI (ImageJ)[118], and reconstructed back into a bulk 3D image. Final image processing was carried out to determine the fluorescence intensity of particles bound to the inner walls and cell monolayer of each channel. Comparisons were then made across varying PEG percentages and shear rates in order to identify a more refined range of PEG percentages to investigate.

2.2.9 Statistical analysis

Statistical analysis of all obtained results was run utilizing IBM's SPSS statistical software package (IBM Corp.). All of the figures have significant differences indicated above elements within the plots. One way ANOVA tests were run for each data set with confidence levels of 95% held throughout all plots. All analyses were carried out under conditions of Tukey equal variances assumed, along with tests of homogeneity of variance further verified by both Brown-Forsythe and Welch analyses. Significant differences between 0% PEG and all other experimental PEG percentages indicated by " * ", with confidence level of 95%. Significant differences indicated in Fig 2.6(D), are between the average anti-EpCAM values and the average of the bare and IgG values which are denoted by "* ", noting that all differences are given at a confidence level of 95%.

2.3 Results and Discussion

2.3.1 Microfluidic device production

Single layer microfluidic devices were produced using PDMS and glass slides. Sterilization of the devices was achieved via use of an autoclave. Cell growth was successfully achieved under negligible shear rates to ensure that media exchange continuously occurred while limiting the influence of the shear on the cancer cells growth. Fig 2.1 depicts a channel design schema (A), produced device with contrast dye for imaging purposes (B), a representative fluorescence image of HCT116 cells growing within a channel of one device (C), and a device schema of particle suspension flow tests (D).

2.3.2 Solid lipid nanoparticle characterization

The solid lipid nanoparticles were validated to have an average diameter of between 150 to 200nm via dynamic light scattering for the experimental flow tests performed as seen in Fig 2.2. The SLNPs were determined to have uniform spherical shapes by Particle Sciences.

2.3.3 HCT116 growth and staining

HCT116 cancer cells were successfully grown within the channels under a low shear rate (50/sec) in order to facilitate constant media exchange. The cell growth achieved was considered confluent, with 90% or more of the channel surface being covered by cells. All devices reached confluency around 5 days of growth under low shear flow. Representative brightfield images of HCT116 cultures which were considered to be confluent can be observed in Fig 2.4(A). Subsequent cell staining was performed with Cell Tracker Green as seen in Fig 2.4(B). Use of the Cell Tracker Green allowed for differentiation between cells, SLNPs non-specifically bound to surfaces other than cells, and SLNPs specifically bound to cells within the channels. Differentiation between the various signal colors recorded from the confocal scans is important to ensure that later quantification of specifically and non-specifically bound particles is performed properly to ensure accurate results.

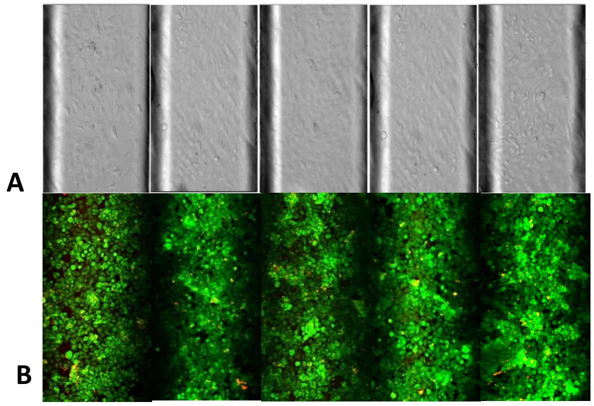

Figure 2.4 Representative brightfield and fluorescence images of HCT116 cultures within microfluidic devices. (A) Brightfield images of HCT116 cells. (B) Fluorescence images of stained HCT116 cells with Cell Tracker Green. All scale bars: 250μm.

2.3.4 Non-specific SLNP binding

Rounds of non-specific SLNP were run using "bare" nanoparticles only coated in a range of PEG surface coating percentages (bare SLNPs) in order to establish baseline values for SLNP binding and to investigate if the presence or absence of cells grown in the devices have strong influence on binding. The percentages used were: 0, 1, 6, 12, and 100%‡ and three different shear rates of 200, 800, and 1600 sec^{-1} were tested to understand how bare SLNP binding performed. Refer to the "PEG Surface Area Coverage Calculations" portion of the Methods section and Table 2.2 for details on how the calculations were carried out. The PEG surface coating percentage indicated as 100%‡ was actually calculated as 124%, however, the theoretical maximum can only 100% of the SLNPs surface. As such, the reported values measure is set to 100%‡, with the assumption that the calculated value of 124% indicates that some of the PEG from the SLNP remains incorporated in the volume of the particle as opposed to being all fully exposed on the particle's surface. The same notation of 100%‡ is used in the later antibody specific binding section and has the same meaning. The total range of PEG surface coating percentages was dictated by the amount of PEG which could be incorporated into the lipid mixture used to produce the SLNPs, which ranged from no PEG to 20% PEG by volume. The initial PEG surface coating percentages chosen for the non-specific and first round of antibody specific testing focused on the lower end of the total range as a result of preliminary trials run under static conditions. Subsequent refinements were made to the percentages chosen for the second round of antibody specific testing in order to better focus in on the range of PEG surface coating percentages which facilitated the greatest degree of binding to cells. The shear rate values used for the non-specific and first round of antibody specific tests were chosen to test SLNP binding under a range of controlled shear forces to understand how such forces influence nanoparticle adhesion. Subsequent refinements were made to the shear rate used in the second round of antibody specific testing, where the larger two shear rates were dropped. Overall, a trend was observed that the total amount of SLNP binding reduced as the PEG coating percentage was increased as seen in Fig 2.3. Additionally, it was observed that increasing the shear rate established during the binding tests resulted in lower amounts of SLNP binding. Lastly, it was observed that non-specific binding of the PEG coated SLNPs occurred approximately equally when run through PDMS devices containing no cells and PDMS devices containing a HCT116 monolayer grown on the bottom of the channel. The lack of difference in binding between devices with and without HCT116 cells indicates that the mechanism of non-specific binding is not influenced by the presence or absence of cells, instead is more heavily influenced by the absorption of serum proteins as indicated in literature[119]–[123]. Fig 2.3 depicts the non-specific SLNP binding results in microfluidic devices with and without HCT116 cells at various shear rates and PEG surface coating percentages.

2.3.5 Influence of shear rate on SLNP binding

In order to assess the influence of shear rate on SLNP binding, SLNP suspension binding flow tests were carried out at various shear rates of 200, 800, and 1600 sec^{-1} as seen in Fig 2.5(A). The PEG surface area coating percentages used were the result of preliminary findings from binding tests run under static conditions, where better performance was observed in the lower end of the total range. Overall, improved SLNP binding was observed under conditions of 200/sec shear, followed by 800/sec and 1600/sec, respectively. The rationale behind these observations is that under lower shear stresses, the SLNPs are better able to bind and remain adhered to the cell coated and exposed PDMS surfaces within the channels, as is apparent in Fig 2.5(A,B&D). Under conditions of 200/sec shear, the PEG percentage which facilitated the greatest ratio of cell binding was the 12% PEG test case as observed in Fig 2.5(B). Representative fluorescent confocal scans compressed into single images are shown in Fig 2.5(C) for the 200/sec shear rate tests. From these images lower PEG percentages result in increased red fluorescence signal. The red signal is the result of SLNPs which have non-specifically bound to surfaces within the channel which are not cells, across all shear rates tested. When lower shear rate values and higher PEG percentages of 12% and 100%[‡] are used very little red signal is observed, instead a yellow-green signal is dominant which occurs when the red signal of the SLNPs mixes with the green signal from the cells. The production of the yellow-green signal is the result of SLNPs being bound directly to the surfaces of the cells being grown within the channels.

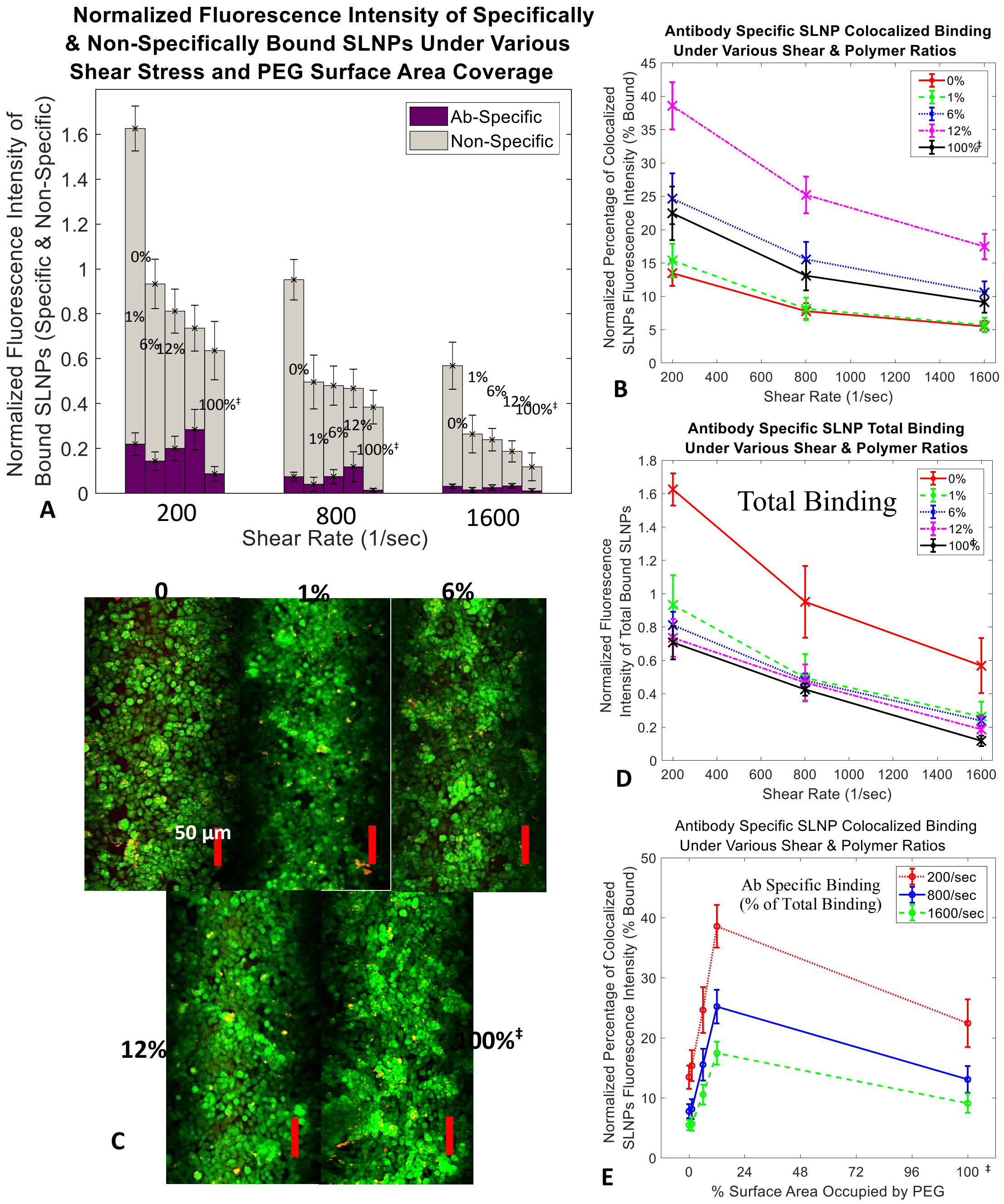

Figure 2.5 Normalized antibody specific binding under various shear rates and PEG percentages. Data shown as sum of means ± S.D. (n=5 independent microfluidic devices) for each testing condition. (A) Normalized fluorescence intensities of (specifically and non-specifically) bound SLNPs under various shear and PEG percentage conditions. (B) Normalized percentages of specifically bound (colocalized) SLNPs to total SLNP binding under various shear and PEG percentages. (C) Representative compressed fluorescence confocal images with SLNPs of varying PEG percentages at 200/sec shear rate. Scale bars are all 50µm in length (D) Normalized total fluorescence intensity of all bound SLNPs for

given shear rates and PEG percentages. (E) Normalized percentages of cell bound SLNPs vs. surface area occupied by PEG, indicating the largest ratios and the large gap between 12% and 100%‡ test cases which was later filled in with additional testing in the following section.

Under conditions of 800/sec shear, more SLNP binding was observed when compared to the 1600/sec test cases with the 12% PEG percentage producing the greatest cell bound ratio as indicated in Fig 2.5(B). Likewise, when considering the 1600/sec shear test cases, the PEG percentage which produced the greatest cell bound ratio was the 12% test cases.

Overall trends observed for binding of the SLNPs show that lower shear rate values resulted in greater quantities of SLNPs binding within the channels. In addition, when considering the total amount of SLNP binding, the 0% PEG tests showed the greatest amount of total binding as observed in Fig 2.5(D). Lastly, it is noted that a general trend exists in the amount of cell specific binding, where an increase is observed from the 0% test cases up to a maximum at the 12.36% tests cases. Continuing to increase the PEG surface area percentage to 100%‡ shows a decrease in cell specific binding. As such, the following round of antibody specific testing includes the addition of two extra PEG surface area percentages, namely 37% and 74%. Additionally, based on the results of this section the shear rate of 200/sec was chosen to use for the remainder of the experimental work because it resulted in the greatest amount of SLNP binding when compared to the larger two shear rates tested.

2.3.6 Influence of PEG surface coating percentage on antibody specific SLNP binding

Based on the results received from the shear rate binding studies, all of the following experimental work was carried out at a shear rate of 200sec^{-1} that provided data showing the greatest degree of change in binding based on PEG surface coating percentages. In addition to refining the shear rates used in the second round of antibody specific testing, the PEG surface coating percentage range was also adjusted. Based on results from the first round of antibody specific testing, the 1% samples were dropped and two additional percentages were added between the 12% and 100%[‡] samples, namely the 37% and 74% samples. The justification for the addition of the 37% and 74% samples was to focus in on the range which facilitated the greatest degree of binding to cells. The following data in Fig 2.6 depict normalized fluorecence intensities of bound (specific and non-specific) SLNPs within the microfluidic channel containing confluent monolayers of HCT116s. Three different SLNP conditions were tested including, bare SLNPs, IgG coated SLNPs and anti-EpCAM coated SLNPs to represent, bare, non-specific and specific binding conditions, respectively.

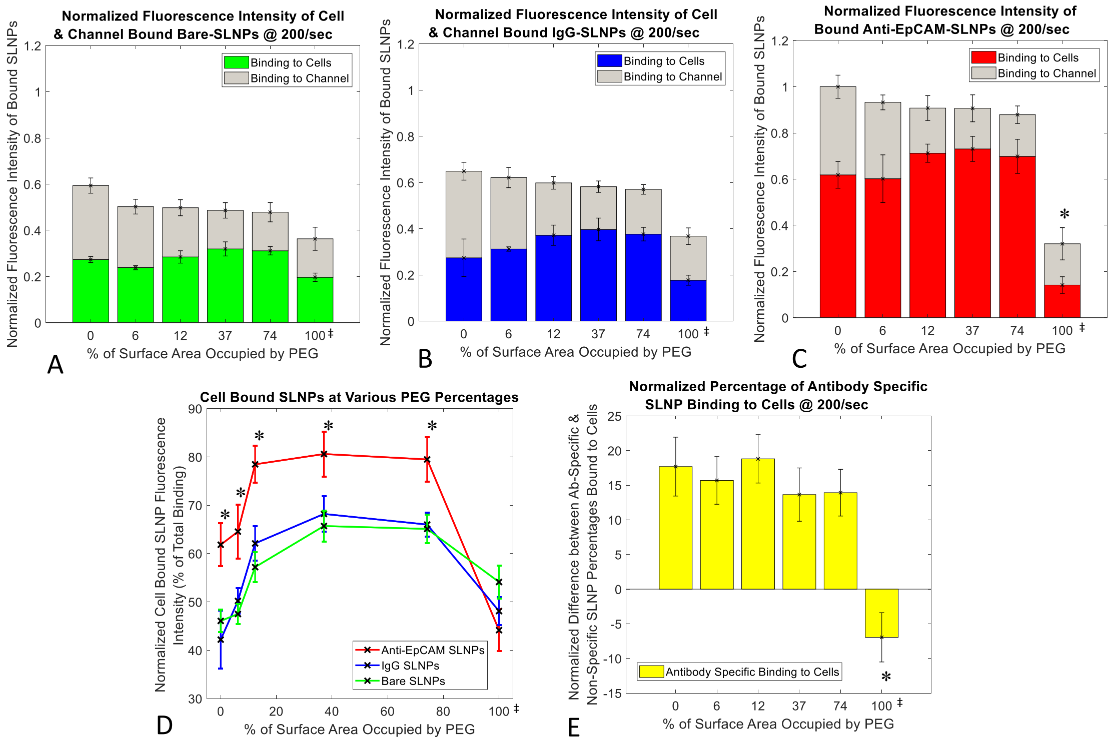

Figure 2.6 Normalized fluorescence intensities of bound SLNPs at various PEG surface area coverage percentages. Data shown as sum of means ± S.D. (n=3 independent microfluidic devices) for each testing condition. (A) Normalized fluorescence intensities of (cell and channel) bound bare SLNPs for various PEG surface area occupation percentages. (B) Normalized fluorescence intensities of (cell and channel) bound IgG SLNPs for various PEG surface area occupation percentages. (C) Normalized fluorescence intensities of (cell and channel) bound anti-EpCAM SLNPs for various PEG surface area occupation percentages. One way ANOVA statistical analysis between 0% and all other experimental conditions with statistical significance indicated by * in plot at $p \leq 0.05$. (D) Normalized fluorescence intensities of cell bound SLNPs as percentages of the total fluorescence intensity of bound SLNPs for various PEG surface area occupation percentages. One way ANOVA statistical analysis between Ab and control test cases with statistical significance indicated by * in plot at $p \leq 0.05$. (E) Normalized difference between Ab-specific and non-specific SLNPs bound to cells for various PEG surface area occupation percentages. One way ANOVA statistical analysis between 0% and all other experimental conditions with statistical significance indicated by * in plot at $p \leq 0.05$. The largest percentage of SLNP surface area occupied by PEG is calculated to be greater than 100% at a value of 124%. For practical purposes, this percentage is reported as 100% throughout the publication and indicated by ‡ in order to signify that the reported value is adjusted.

Fig 2.6(A) depicts the fluorescenc intensity of bare SLNPs bound within the microfludic devices. The bare SLNPs only have PEG on the surface, with the IgG SLNPs have PEG and IgG, and the Ab-specific SLNPs had PEG and anti-EpCAM on the surface. Fig 2.6(B) depicts the FI of bound IgG SLNPs at various PEG surface area occupation percentages. Fig 2.6(C) shows the FI of bound anti-EpCAM SLNPS at various PEG surface area occupation percentages. The binding indicated in Figs 2.6(A-C) are separated into SLNPs bound to cells and those bound non-specifically elsewhere within the channel. Fig 2.6(D) depcits the cell bound FI of each SLNP type as a percentage of the total FI measured within the devices. Viewing the data in this manner helps to clearly identify which SLNP type and PEG% produced the greatest ratio of SLNPs bound to cells within the devices. Lastly, Fig 2.6(E) shows the relative difference between the average cell bound percentage of the bare and IgG SLNP tests at each PEG% and the average cell bound percentage for the anti-EpCAM tests at each PEG%. Viewing the data in this manner allows for the visualization of how the antibody specific mediated SLNP binding outperfomred the non-specific binding tests (bare and IgG) over the range of PEG%s tested. Overall, the data below indicate that the SLNPs coated with anti-EpCAM and which had 37% of their total surface area covered by PEG produced the greatest amount of targeted delivery specifically to the HCT116 cancer cells. Refer to Figs 2.7 - 2.9 to see representative images of the various SLNP types bound to HCT116 cells at various PEG surface area coverage percentages. In Figs 2.7-2.9, particle aggregation is observed during the binding process which is likely due in part to the carnauba wax which makes up the majority of the SLNPs. Exposure of the wax to an aqueous environment in turn causes the SLNPs to aggregate toegther within the microfluidic channels when the hydrohpobic particles encounter each other during the process of bidning to the cell monolayers. The aggregation during the binding process is most prevelant for the SLNPs with the least amount of PEG surface coatings, because ore of the carnauba wax core of the particles is exposed. The presence of PEG on the surface of the SLNPs finctions to shiled the hydrophobic core of the particles and results in less aggreation during the binding process within the channels. Aggrigation of the SLNPs is prevented prior to the binding event within the channel through the use of detergents. When intorduced into the microfluidic channels, the detergent is rapidly diluted icnreasing the likelihood of SLNP self-association during the flow based binding. The use of additional detergent when introducing the SLNPs into the devices could be used to prevent this issue, however, it would need to be ensured that the presence of added detergent would not negatively influence the cellular monolayer in the devices.

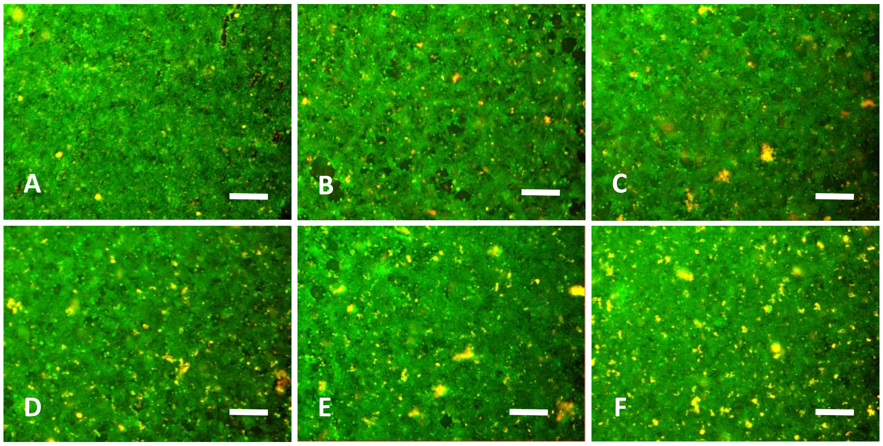

Figure 2.7 Representative fluorescence image taken from confocal scan of HCT116 (green) and bare SLNPs (red). (A) 100%‡ PEG coverage. (B) 74% PEG coverage. (C) 37% PEG coverage. (D) 12% PEG coverage. (E) 6% PEG coverage. (F) 0% PEG coverage. HCT116 stained with Cell Tracker Green^{TM}. SLNPs produce red fluorescence signal. When SLNPs bind to cell surface, green and red signal mix to produce yellow signal.

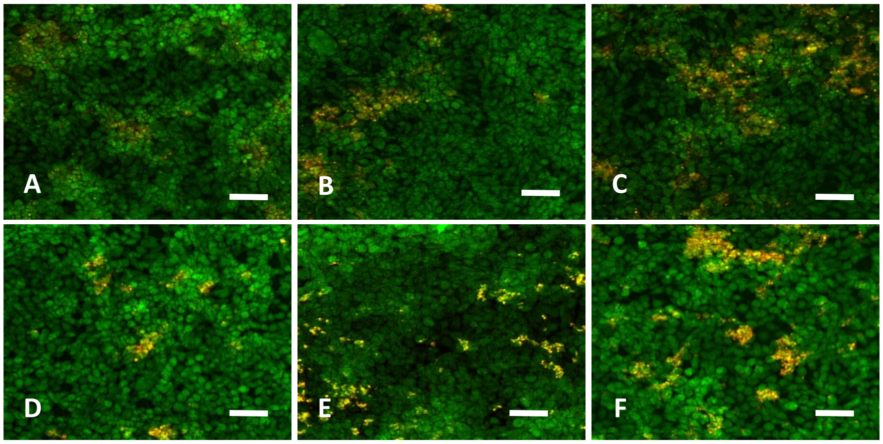

Figure 2.8 Representative fluorescence image taken from confocal scan of HCT116 (green) and IgG SLNPs (red). (A) 100%‡ PEG coverage. (B) 74% PEG coverage. (C) 37% PEG coverage. (D) 12% PEG coverage. (E) 6% PEG coverage. (F) 0% PEG coverage. HCT116 stained with Cell Tracker Green^{TM}. SLNPs produce red fluorescence signal. When SLNPs bind to cell surface, green and red signal mix to produce yellow signal.

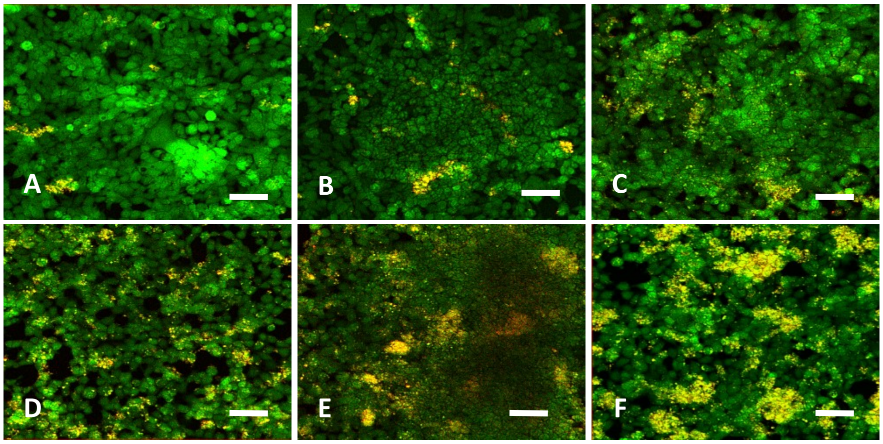

Figure 2.9 Representative fluorescence image taken from confocal scan of HCT116 (green) and anti-EpCAM SLNPs (red). (A) 100%‡ PEG coverage. (B) 74% PEG coverage. (C) 37% PEG coverage. (D) 12% PEG coverage. (E) 6% PEG coverage. (F) 0% PEG coverage. HCT116 stained with Cell Tracker Green^{TM}. SLNPs produce red fluorescence signal. When SLNPs bind to cell surface, green and red signal mix to produce yellow signal.

2.4 Conclusions

The goal of this study was to provide insight into improving therapeutic delivery via SLNPs through the application of antibody specific disease targeting combined with PEG mediated reductions in non-specific delivery.

Single layer microfluidic systems were produced which were capable of sustaining HCT116 cancer cell growth to fully confluent conditions under a range of shear rates. Initial binding tests were performed in devices with and without HCT116 cells verified that the presence or absence of cells within the channels did not significantly impact the degree of SLNP binding observed. This observation agrees with literature findings which indicate that the major factor influencing non-specific nanoparticle binding is the absorption of proteins on the surface of the nanoparticles[119]–[123]. The initial shear rates tested were 200, 800, and 1600sec^{-1}, with the goal of identifying the influence of shear on the binding of SLNPs within the system. It was determined that higher shear rates led to lower amounts of SLNP binding as has been demonstrated in previous work[57], [124]. In addition to testing different shear rates, a range of PEG coating percentages were tested for SLNPs which also contained anti-EpCAM on their surfaces. The initial range of PEG coating percentages was: 0, 1, 6, 12, and 100%‡ which were decided upon as a result of preliminary studies conducted under static conditions at Particle Sciences®. From the initial range of PEG coating percentages, the largest amount of targeted delivery occurred for the 12% test case. Overall, a general trend was observed where targeted delivery was very low for the 0% tests with an observed increase as the coating percentage increased to 12%, followed by a drop as the percentage was increased to 100%‡. From the initial data, a more refined range of PEG surface coating percentages was chosen in order to identify improved SLNP compositions which would perform even better.

The refined range for the second half of the study included two additional PEG coating percentages between 12% and 100%‡. Specifically, the new range which was tested included: 0, 6, 12, 37, 74, and 100%‡. In addition to testing over an adjusted coating percentage range, three different SLNP protein coatings were tested. Namely, bare, IgG coated, and anti-EpCAM coated SLNPs were tested at all six of the PEG coating percentages listed above. The bare SLNPs tested only contained PEG on their surfaces at the specific percentages listed above and were used as control cases in order to identify if the addition of antibodies onto the surface of the SLNPs had any influence on binding. The IgG SLNPs tested contained the PEG percentages listed above in addition to IgG which were used as secondary control cases to identify if the addition of non-specific antibodies onto the SLNPs had any influence on binding. Lastly, the anti-EpCAM SLNPs were tested to identify the influence of a target antibody on SLNP binding to the HCT116 cells. Overall, similar levels of SLNP binding were observed between the two control cases (bare and IgG) and an increased level of total binding was observed for the anti-EpCAM cases. Across all three protein types and all PEG coating percentages tested, the amount of SLNP binding to cells was lower than the amount of binding to the exposed PDMS channel walls. However, this was expected because only one surface within the channels was coated with a monolayer of cells while the other three surfaces were bare PDMS. When comparing the targeted performance of each protein coating type, the anti-EpCAM SLNPs produced the greatest cell bound ratios as expected across all PEG coating percentages tested.

When considering the updated range of PEG coating percentages tested, the SLNPs coated with 37% PEG on their surfaces showed the greatest amount of targeted delivery across all three protein coating types tested. It should also be noted that while displaying a slightly lower degree of targeted delivery, the 74% PEG coated SLNPs also performed well. Given the trend observed in Fig 2.6(D), a local theoretical maximum may possibly exist between the 37% and 74% test cases, however the improvement to targeted delivery is expected to be minimal. Additionally, the drop in the percentage of SLNP binding to cells within the devices as the PEG surface coating percentage increases, leads to the assumption that addition of too much PEG onto the surface of the SLNPs can lead to over-crowding and hindrance of the anti-EpCAM present. As such, a careful balance exists between the antibody and PEG present on the surface of the SLNPs where enough PEG must be added to reduce non-specific binding as much as possible without interfering with the function of the targeted antibody.

Overall, the developed microfluidic system and SLNP therapeutic carriers have shown that improved targeted delivery of nanoparticles to diseased cancerous cells can be facilitated through the application of a target specific antibody and PEG surface coating. From this work an understanding between the balance of antibody specific targeted binding and inhibition of non-specific binding via PEG has been developed. In addition, a range of antibody and PEG ratios have been tested to identify a local condition which facilitates improved targeted delivery. Using such an approach may serve to better reduce the non-specific adhesion of such SLNPs while still providing a means of targeted delivery to sites of cancerous tissues. In order to further improve the physiological relevance of the microfluidic system, the inclusion of vascular endothelium is desired. Inclusion of an endothelial barrier provides a means of studying therapeutic delivery from mimicked vasculature to regions of cancerous tissue. As such, the following chapter demonstrates the use of a bi-layer microfluidic system capable of facilitating a monolayer of endothelial cells and cancer cell growth simultaneously.

Chapter 3: Biomimetic microfluidic platform for the quantification of transient endothelial monolayer permeability and therapeutic transport under mimicked cancerous conditions

3.1 Introduction

As mentioned in Chapter 2, the incorporation of a mimicked blood vessel is required to improve the physiological relevance of the microfluidic systems when studying therapeutic delivery to cancer. The presence of diseased regions near vasculature can lead to states of increased endothelial monolayer permeability [78], [125]–[128]. These increases in vasculature permeability are often the result of vascular permeabilizing agent production and excretion from diseased regions, such as cancerous regions [78], [125], [127], [128]. In the case of cancerous regions, tumor benefits from increased vascular permeability include improved supply of nutrients and removal of cellular waste products as well as access to the vascular system allowing for easy metastasis [129]–[131].

In order to combat such diseased conditions, therapeutic delivery via the vascular system is often utilized [130]–[134]. However, this approach for delivering drugs can be difficult due to varying degrees of endothelial permeability and differences in pressure between the vasculature and the diseased site [129], [132], [133], [135]–[138]. For the case of cancer, fluctuations in capillary level endothelial permeability occur as cancerous cells are killed off by anti-cancer drugs, resulting in an overall decrease in the production of vascular permeabilizing agents [139], [140]. In turn this allows for the vasculature to begin to repair and reduce permeability [139], [140]. As further cancerous cells are targeted and killed, the degree of vascular permeability further reduces, in turn reducing the overall free transport of anti-cancer therapeutics [139], [140].

In addition to fluctuations in endothelial permeability, the occurrence of pressure differentials between blood vessels and diseased sites can also greatly influence therapeutic delivery [136]–[138]. Situations when vascular pressure is lower than that of the diseased region causes added difficulty when attempting to deliver therapeutics [133], [136]–[138]. Examples from literature where interstitial fluid pressure is greater than vascular pressure leads to difficulties in delivering therapeutics to solid tumor sites and inflamed pulpal cells [141], [142]. As such understanding how differences in pressures and flow rates can influence the transport and delivery of therapeutics is beneficial for disease treatment.

In order to better understand the role of the endothelial barrier and the effect of cancerous cells on the transport of therapeutics to diseased regions, a bi-layer microfluidic device has been fabricated which allows for the co-culture of healthy endothelial cells with a secondary cell type [56], [58]. This is achieved while also providing a means of control over the pressures generated in both layers of the device. Throughout the following work, physiologically relevant flow conditions are established in the mimicked vasculature while cancerous cells are used to create a tumor microenvironment. Presence of the cancerous cells provides the system with permeabilizing agents which act to modulate endothelial confluency. The application of flow induced pressures and the application of therapeutics provides insight into optimal treatment options for patient specific disease conditions.

As in any model, the physiological relevance of specific parameters varies. For example, a rather unconventional approach has been utilized to manipulate pressures within the system in a controlled manner. The pros and contras of this and other features of the model are carefully evaluated in the Discussion with consideration given to the data provided by the model.

Overall, this work has been geared around better understanding how the transient nature of the endothelial barrier, presence of flow derived pressures, and variations in system conditions influence the transport and delivery of therapeutics. Through this work we aim to quantify tumor cell induced permeability of microvessels within a mimetic microfluidic system. In addition, we aim to quantify the temporal effect of therapeutics on the measured microvessel permeability throughout time-course treatments.

3.2 Experimental

3.2.1 Materials

The media used for HCT116 cells was Dulbecco's Modified Eagle's Medium (DMEM, Life Technology), with 10% fetal bovine serum (FBS, Invitrogen) and 1% Antibiotic & Antimycotic (ThermoFisher). The media used for BAOEC cells was Dulbecco's Modified Eagle's Medium (DMEM, Life Technology), with 10% heat inactivated fetal bovine serum (FBS, Invitrogen) and 1% Antibiotic & Antimycotic (ThermoFisher). Procine gelatin (0.5%, Sigma-Aldrich) was used to facilitate adhesion of BAOEC within devices. CellTracker Green was used to fluorescently label cells (ThermoFisher). Microfluidic molds were digitally cut from printable gold foil sheet (Silhouette) with Silhouette SD digital cutter (Silhouette). Microfluidic devices were produced from Sylgard 184 polydimethylsiloxane (PDMS) (Dow Corning), Nuclepore polycarbonate semi-permeable membranes with 800nm pore diameter (Whatman), and microscope cover glass slides (FisherBrand). Syringe pumps were used for nanoparticle flow tests (Harvard Apparatus). Paclitaxel (LC Laboratories, Prod. No: P-9600 Lot: ASM-118) and doxorubicin (LC Laboratories, Prod. No: D-4000 Lot: DXR-110) were used as anti-cancer therapeutics. FITC, FITC-Dextran 4kDa, and FITC-Dextran 70kDa (Sigma-Aldrich) were used to visualize transport from vessel to cancer. All other reagents not mentioned were used directly without purifying.

3.2.2 Microfluidic device design, fabrication and assembly

Microfluidic devices were fabricated using polydimethylsiloxane (PDMS) (SYLGARD 184, Dow Corning) and assembled into a bi-layer device as depicted in Fig 3.1. The devices were fabricated using two separate pieces of PDMS with channels molded into them and a polycarbonate semi-permeable membrane (Whatman Cyclopore, Sigma-Aldrich). The semi-permeable membrane is adhered to both pieces of PDMS and sandwiched between the overlapping regions of the channels. The regions where the channels in both pieces of PDMS overlap facilitates transport from one channel into the other through the pores in the semi-permeable membrane. As a result, the pores of the membrane act to dictate the maximum size of materials which can be transferred. In order to only allow for culturing media and small chemical components to pass from one channel to the other while restricting the transport of cells, a membrane with an average pore size of one micrometer was chosen. Because cells are not capable of passing through the membrane, a co-culture setup is achievable by growing bovine aortic endothelial cells (BAOECs) on the top surface of the membrane within the apical channel, while human colorectal cancer cells (HCT116s) are grown on the bottom surface of the lower channel termed the basal channel as depicted in Fig 3.2.

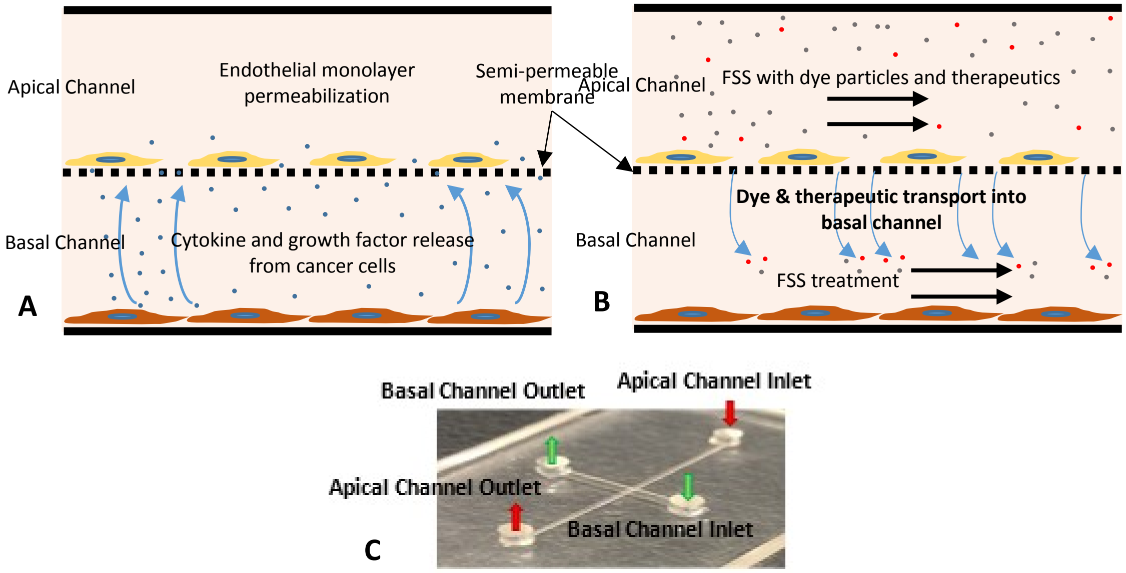

Figure 3.1 Device schema depicting culturing setup and experimental conditions for dye and therapeutic transport to cancer region in basal channel. (A) Bi-layer microfluidic device setup with apical and basal channel separated by semi-permeable membrane. A BAOEC endothelial monolayer is grown on the surface of the semi-permeable membrane and a HCT116 cancer monolayer is grown in the basal channel. Cytokines and growth factors released by the HCT116s influence the permeability of the BAOEC monolayer. (B) Device setup depicting therapeutic and dye transport across the permeabilized BAOEC monolayer and semi-permeable membrane in order to function on the HCT116s present in the basal channel. (C) Image of bi-layer device showing apical and basal channel along with respective inlets and outlets

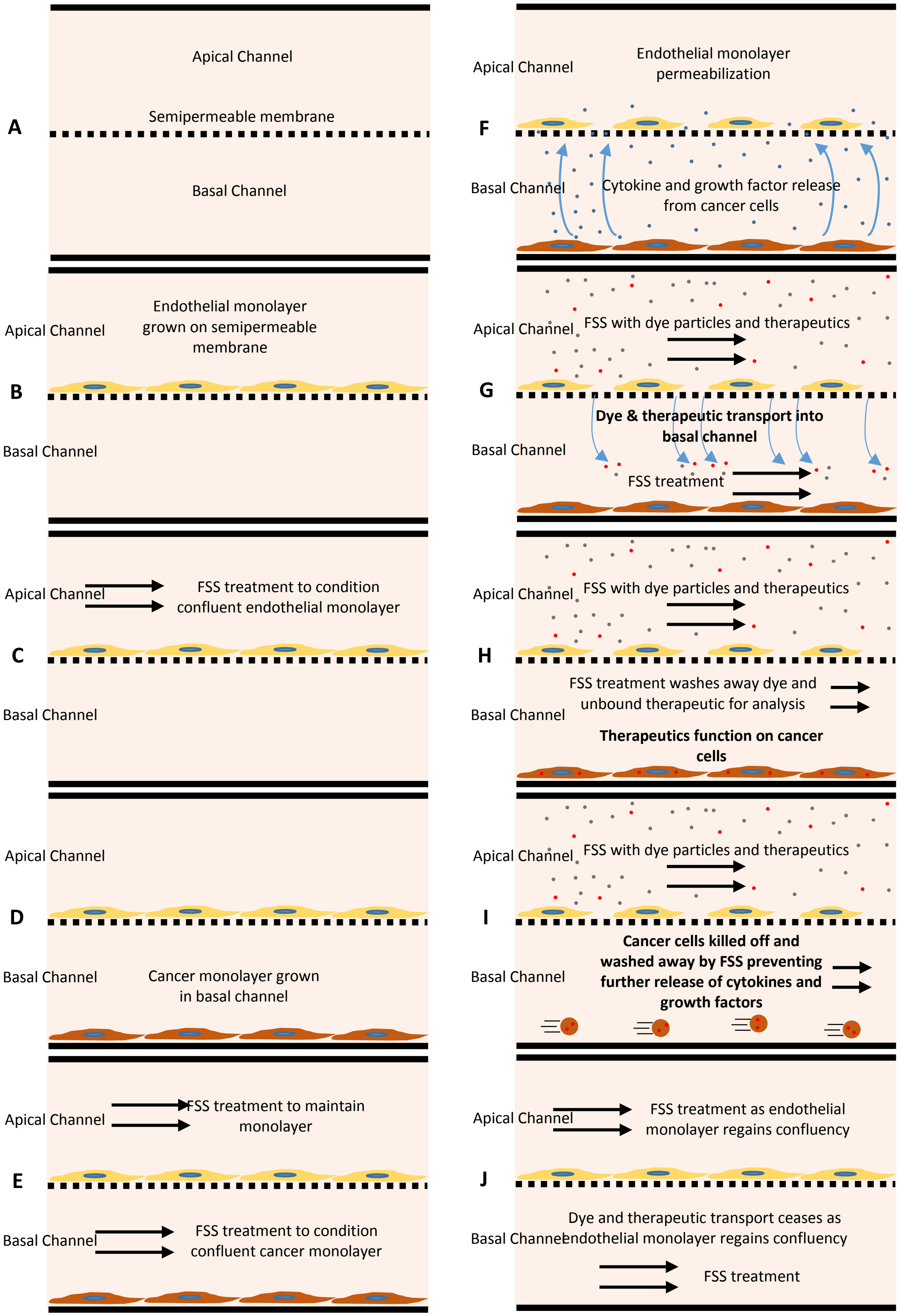
A
Apical Channel
Semipermeable membrane
Basal Channel
B
Apical Channel
Endothelial monolayer grown on semipermeable membrane
Basal Channel
C
Apical Channel
FSS treatment to condition confluent endothelial monolayer
Basal Channel
D
Apical Channel
Basal Channel
Cancer monolayer grown in basal channel
E
Apical Channel
FSS treatment to maintain monolayer
Basal Channel
FSS treatment to condition confluent cancer monolayer
F
Apical Channel
Endothelial monolayer permeabilization
Basal Channel
Cytokine and growth factor release from cancer cells
G
Apical Channel
FSS with dye particles and therapeutics
Basal Channel
Dye & therapeutic transport into basal channel
FSS treatment
H
Apical Channel
FSS with dye particles and therapeutics
Basal Channel
FSS treatment washes away dye and unbound therapeutic for analysis
Therapeutics function on cancer cells
I
Apical Channel
FSS with dye particles and therapeutics
Basal Channel
Cancer cells killed off and washed away by FSS preventing further release of cytokines and growth factors
J
Apical Channel
FSS treatment as endothelial monolayer regains confluency
Basal Channel
Dye and therapeutic transport ceases as endothelial monolayer regains confluency
FSS treatment

Figure 3.2 Device schema depicting culturing setup and testing conditions. (A) Basic setup. (B) BAOEC monolayer grown in apical channel. (C) BAOEC monolayer grown to confluency under shear flow. (D) HCT116s introduced into basal channel. (E) HCT116s grown under shear flow. (F) HCT116s growing in basal channel release cytokines and permeabilizing agents making BAOEC monolayer highly permeable. (G) Dye and therapeutics flown in apical channel transport across BAOEC layer and semi-permeable membrane. (H) Transported therapeutic functions on HCT116s. (I) HCT116s are killed off and washed away down-stream in channel. (J) Media shear flow is continued in apical and basal channel as BAOEC monolayer regains confluency.

3.2.3 Cell growth on device

After fabrication of the microfluidic devices, both the apical and basal channels were filled with a 0.5% porcine gelatin (PG) (0.5%, Sigma-Aldrich) solution and incubated for 30 minutes at 37^0C and 5% CO_2. After incubation, the PG is removed and replaced with BAOEC (Cell Applications, San Diego, CA) suspension in the apical channel and incubated for 12 hours to allow for cell adhesion to the top side of the semi-permeable membrane. After 12 hours, all remaining cell suspension is washed away by establishing media (DMEM(1x) + GlutaMAX – I (gibco, life technologies), 10% HI-FBS (Sigma-Aldrich), 1% Penn/Strep Antibiotic(1X) (Gibco, life Technologies)) flow within the channel using sterile tubing, syringe and syringe pump (PHD 2000, Harvard Apparatus). The flow rate established within the channel is kept low for purposes of media exchange and aligning the BAOECs to flow. These flow based incubation conditions are held constant typically for 3 to 4 days until the endothelial monolayer on the semi-permeable membrane reaches confluency. Upon achieving a confluent BAOEC monolayer in the apical channel, HCT116s (ATCC, Manassas, VA) are introduced into the basal channel and allowed to settle and adhere to the bottom of the basal channel for 24 to 48 hours. HCT116 cells are introduced into the devices in order to permeabilize BAOEC monolayers similar to conditions found in various cancerous disease states. Once the HCT116 cells have properly adhered, a flow rate equivalent to that established in the apical channel is setup in the basal channel using a secondary syringe pump. Both the BAOEC and HCT116 cells are grown within the bi-layer device under these flow conditions within an incubator until experimental proceedings begin.

3.2.4 Establishing shear rate

The effect of fluid shear on the growth of cells and transport of compounds from channel to channel is established using syringe pumps (PHD 2000, Harvard Apparatus). The syringe pumps allow for control over the flow rates established in both channels of the device. By altering the flow rate within the channels, we are able to specifically set and control the shear rate imparted on the cells growing within each channel and any other materials introduced into the channel along with the flowing media. The equation governing [112] the shear rate established in each of the channels is as follows: $Shear\ Rate = (\frac{6Q}{W*H^2})(1+\frac{H}{W})(f^*)(\frac{H}{W})$, where Q is the established flow rate within the given channel, W is the channel width, H is the channel height, and f^* is a geometrical factor based on channel dimensions which for the microfluidic devices used is 0.7946. The width and height dimensions for the channels utilized in this study were 500 micrometers and 100 micrometers, respectively. In order to stay within a physiologically relevant range [113]–[115], the shear rate in the apical channel containing the BAOECs was held at 200 sec^{-1} which is at the lower end of range typically experienced within the arterioles of the body. The shear rate established within the basal channel containing HCT116s was held constant with the shear in the apical channel to prevent any convective flux between channels when not desired. While initially culturing cells within both channels, the shear rate was typically set around 50 sec^{-1} as a means of simply refreshing media exposed to the cells for continued growth while not imparting drastically high shear. It should be noted that both equal and differing shear rates were established in the channels depending on if a pressure difference across the semi-permeable membrane was desired.

3.2.5 Establishing pressures within the channels

In order to simulate the effect of pressures within the system, the relative shear rates established in the channels were varied to achieve desired average channel pressures. In order to prevent the establishment of a pressure differential across the semi-permeable membrane, the shear rates established in both the apical and basal channel were maintained at equal values. The governing equation [143] used to relate the established shear rates in each channel with the average pressure difference across the membrane is as follows:

$$P_\Delta = \frac{\dfrac{\dfrac{12\mu_1 L_1 Q_1}{W_1 H_1^3}}{1-\left(\dfrac{192 H_1}{\pi^5 W_1}\right)\left(\tanh\left(\dfrac{\pi W_1}{2H_1}\right)\right)}}{2} - \frac{\dfrac{\dfrac{12\mu_2 L_2 Q_2}{W_2 H_2^3}}{1-\left(\dfrac{192 H_2}{\pi^5 W_2}\right)\left(\tanh\left(\dfrac{\pi W_2}{2H_2}\right)\right)}}{2}$$

where μ_1 and μ_2 are the viscosity of the fluid in the apical and basal channels respectively, L_1 and L_2 are the overall length of the apical and basal channel respectively, Q_1 and Q_2 are the flow rates established in the apical and basal channels respectively, W_1 and W_2 are the widths of the apical and basal channels and H_1 and H_2 are the heights of the apical and basal channels, respectively. The above equation calculates the average pressure generated in the apical channel and subtracts from it, the average pressure generated in the basal channel. In this case, when P_Δ is equal to zero, it indicates that the average pressures in both the apical and basal channels are the same, allowing for the determination of the flow rates required to achieve the balance of apical and basal channel pressures.

3.2.6 Cell imaging and confluency measurements

Cells grown on devices were imaged utilizing standard fluorescence imaging microscopy (Olympus IX70, Hamamatsu C9300, Plan Fluor 10x & 20x, NA: 0.3, RI: 1). For fluorescence imaging, the plasma membranes of the cultured cells were stained with Cell Tracker Green ^{TM} (10µM, Thermo Fisher Scientific) plasma membrane stain to identify the outer most boundaries of the cells occupying the culturing area. This method of cell plasma membrane (PM) staining allows for the quantification of the area specifically covered by cells within the viewing area of the various fluorescence microscopes. Images taken via conventional fluorescence microscopy were utilized to determine the overall cellular monolayer confluency. These measurements were carried out using the FIGI (ImageJ) software suite [118][144] and the collected image. The imaging technique was used to obtain the average degree of monolayer confluency as well as to quantify the area occupied by gaps between cells. The analysis for the cell coverage measurements were taken once the cells had reached confluency within the apical channel of the device just before HCT116s were introduced into the basal channel. A second measurement of all devices was taken at 24 to 48 hours after introduction of HCT116s into the basal channel. Lastly, final measurements for each device were taken 12, 24, 48, 72, 96, and 120 hours after introduction of anti-cancer therapeutics into the device. Image acquisition software utilized includes HCImage Live (Hamamatsu Photonics) for standard fluorescence imaging and NIS-Elements (Nikon) for acquisition of confocal images.

3.2.7 Anti-cancer therapeutics

In order to study how particle transport is influenced by variations in endothelial monolayer permeability, BAOECs were exposed to HCT116s. Treatment of the microfluidic system with the anti-cancer therapeutics, Paclitaxel and Doxorubicin, allowed for varying degrees of BAOEC permeability within the diseased state setup. The working concentrations for both Paclitaxel and Doxorubicin were 5ng/mL for all experimental testing. Paclitaxel and Doxorubicin functioned to eliminate cancer cells and were chosen due to their wide use, high degree of documentation for *in vitro* and *in vivo* data, and relatively inexpensive cost. The anti-cancer therapeutics were introduced into the apical channel of the devices in order to mimic an intravenous administration. For time-course studies, the anti-cancer therapeutics were continuously introduced into the system via the apical channel over the entire course of 120 hours. Any therapeutic introduced into the microfluidic system was subjected to the shear established within the device in order to mimic the situation or blood flow within the body. Therapeutics which successfully transitioned from the apical channel through the semi-permeable membrane into the basal channel were able to act on the HCT116s present. Interaction of the anti-cancer drugs with the HCT116s resulted in the death of affected cells, which in turn were washed away downstream and eventually out of the device into the waste media collection containers. As such, the HCT116 cells which were killed off and washed away could no longer contribute to the secretion of permeabilizing agents. Lastly, in order to ensure that the presence of the anti-cancer therapeutics caused HCT116 cell death, microfluidic devices containing only HCT116s were subjected to either of the two therapeutics, with cell death verified via cell staining and fluorescence microscopy before and after treatment, as seen in Fig 3.3. Chemical authentication and validation data for the Paclitaxel and Doxorubicin utilized in this work were provided by LC Laboratories (Paclitaxel - Prod. No: P-9600 Lot: ASM-118) (Doxorubicin – Prod. No: D-4000 Lot: DXR-110).

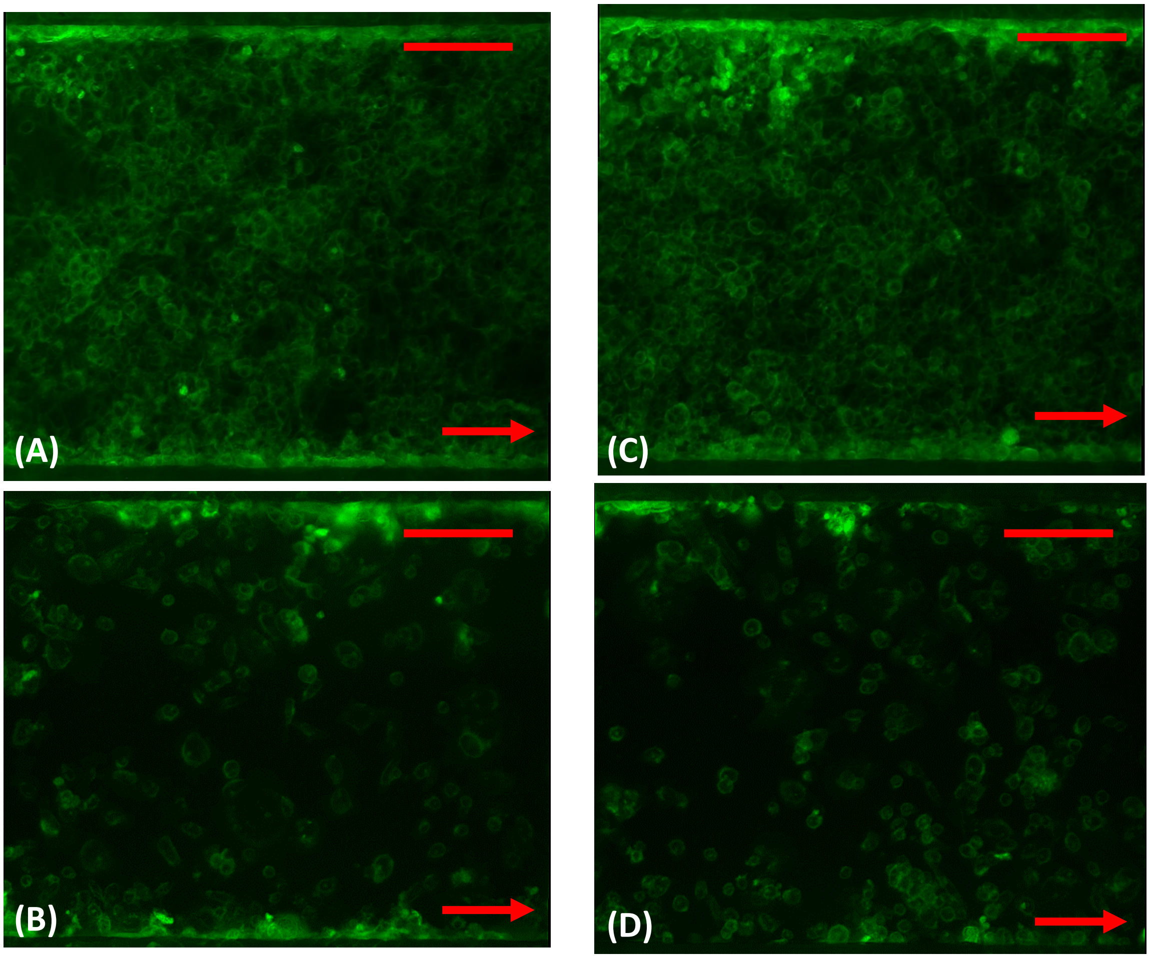

Figure 3.3 Representative fluorescence images of HCT116 monolayers grown under flow in the basal channel of the microfluidic devices with BAOEC in the apical channel before and after 72 hours of treatment with Paclitaxel or Doxorubicin. Cells in all images were stained with Cell Tracker Green^{TM}. (A) Confluent HCT116 monolayer prior to introduction of Paclitaxel in the apical channel. (B) HCT116 cells after treatment with Paclitaxel for 72 hours from the apical channel. (C) Confluent HCT116 monolayer prior to introduction of Doxorubicin in the apical channel. (D) HCT116 cells after treatment with Doxorubicin for 72 hours from the apical channel. Red arrows in the fluorescent images indicate the direction of flow within the channels. All scale bars are 100 μm in length.

Interaction of the anti-cancer therapeutics with BAOECs and subsequent EC cellular responses were investigated by establishing endothelial monolayers within the microfluidic devices without the presence of any cancer cells. Therapeutic solutions were prepared at the same concentrations as described previously. Therapeutic conditioned media was flown through the devices and the BAOECs were stained with Cell Tracker Green in order to facilitate fluorescent imaging. Therapeutic solution flows were established for 120 hours with cell images collected every 24 hours. The resulting images were collected for cell count and EC monolayer permeability measurements. Relative comparisons were made between values measured prior to therapeutic flows (0 hours) and all other measured time points.

3.2.8 Dye cross-vasculature equal pressure transport studies

Dye transport was achieved by flowing dye into the bi-layer channel via syringe pump. In order to quantify the degree of transport for each test case, the outlet flow of both the apical and basal channels was collected separately and distributed into well plates. The fluorescence intensities of the flow-through were measured via plate reader with excitation at 490nm and emission read at 525nm. The dyes utilized in the study include FITC at a working concentration of 0.625mg/mL, FITC-Dextran 4kDa at a working concentration of 5mg/mL, and FITC-Dextran 70kDa at a working concentration of 5mg/mL. The working concentrations for each dye were chosen so that a sufficient fluorescence intensity signal was obtained from the experimental testing for measurement purposes. The basal outlet contained dye which successfully transported across the semi-permeable membrane, and dye exiting out of the apical outlet were collected and measured to ensure that the total dye concentration introduced into the devices was accounted for at both of the outlets.

The transport studies were carried out under three device conditions as follows, cell-free devices, devices with only a BAOEC confluent monolayer, and diseased devices containing a monolayer of BAOECs in the apical channel and a monolayer of HCT116s in the basal channel which were then subjected to a time-course therapeutic treatment. The second and third device conditions established allowed for studies on the ability of dyes to transport under varying degrees of BAOEC permeability. All rounds of transport studies were carried out with flow established in the apical and basal channels. In order to mimic the various pressure conditions experienced within the vasculature, the first rounds of testing were carried out so that no pressure difference was established across the semi-permeable membrane. The pressures established in both the apical and basal channels for these studies were 632.8, 4832.4, and 17431.2 Pa, which were established in addition to the physiologically normal pressure of 10666 Pa (80mmHg). Cell-free device studies did not utilize any cell culturing within the channels prior to introduction of particle suspensions. Devices run with BAOEC confluent monolayers were established 3 to 4 days prior to dye flows to ensure that a highly confluent monolayer was present in the apical channel over the semi-permeable membrane. Lastly, the diseased state devices, were prepared 6 to 8 days in advance of dye flows. 3 to 4 days were spent growing a confluent apical BAOEC monolayer and the remaining days were spent producing a cancer cell monolayer in the basal channel. The transport studies were carried out under adjusted timeframes to ensure that the same amount of dye introduced into each device was the same regardless of the pressure being used. One final note for the diseased state devices, was the later introduction of an anti-cancer therapeutic to influence the cancer cells in the basal channel and the confluency of the BAOEC monolayer in the apical channel. The degree of dye transport was documented throughout a time-course treatment with Paclitaxel and Doxorubicin to understand how the BAOEC monolayer integrity influenced the dye transport capabilities. Experimental schema for this testing can be observed in Fig 3.2 and Fig 3.4.

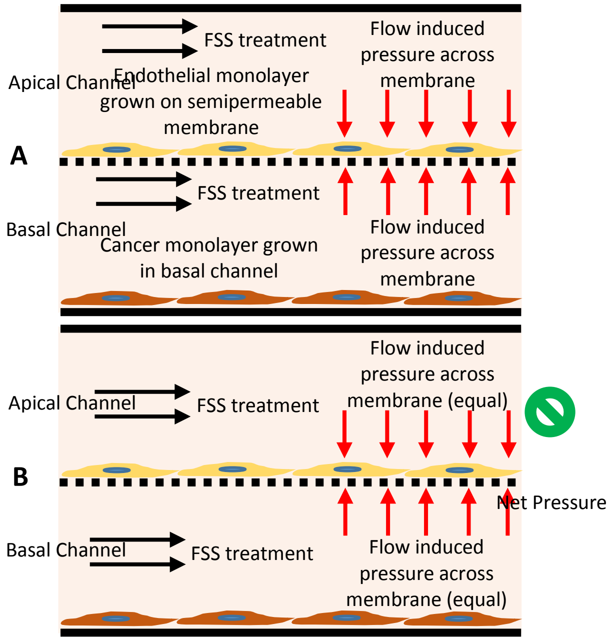

Figure 3.4 Device schema depicting flow conditions for permeability testing. (A) Basic setup. (B) No net pressure across membrane.

3.2.9 Statistical analysis

Statistical analysis of all obtained results was run utilizing IBM's SPSS statistical software package (IBM Corp.). All of the figures have significant differences indicated above elements within the plots. One way ANOVA tests were run for each data set with confidence levels of 95% held throughout all plots. All analyses were carried out under conditions of Tukey equal variances assumed, along with tests of homogeneity of variance further verified by both Brown-Forsythe and Welch analyses. Based on the obtained statistical results, all bar graphs contain grouped pairs between groups and within groups indicating statistically significant differences between means indicated by " * ". For all line plots, statistically significant differences in means are compared against the baseline tests for the spherically shaped particles. Significance between both the short rod particle and long rod particle values are indicated by “ * “. Significant differences between means for short rod and long rod particles are indicated by “ ** “, noting that all differences are given at a confidence level of 95%. Within group F values and degrees of freedom for each plot are noted in their respective legends. Sample sizes for all experimental testing were determined by performing estimation for multiple-sample one-way ANOVA pairwise comparison based on piolet studies utilizing the standard sample size approximation of: $n_{ij} = \frac{2(z\frac{a}{2\tau}+z\beta)^2\sigma^2}{\varepsilon_{ij}^2}$. All statistical comparisons are run under assumptions of equal variance between groups. This assumption is verified via the Levene’s Test where all *p values* must be greater than 0.05 in order to verify the equal variance assumption across groups. All data sets presented in this work pass the Levene’s Test with *p values* greater than 0.05.

3.3 Results and Discussion

3.3.1 Microfluidic device production

Bi-layer microfluidic devices were produced and sterilized using an autoclave in order to permit culturing of both bovine aortic endothelial cells (BAOECs) and human colorectal cancer cells (HCT116s). Device integrity was suitable to allow for the flow of media, dyes and therapeutics without leakage through the use of syringe pumps. A device schema can be observed in Fig 3.1 that depicts the device layout and locations within the device where the BAOEC and HCT116 cells are grown for experimental testing. Full schemas depicting all device setups and testing conditions can be observed in Fig 3.2 and Fig 3.4. Physiologically relevant factors such as the presence of HCT116 cancer cells in close proximity to the vasculature and the natural production/excretion of permeabilizing agents were possible utilizing the microfluidic setup [128], [145]–[147]. However, it is recognized that for some factors, especially the oncotic pressures, the total range and method utilized to achieve the desired goals are not physiologically relevant or accurate [142], [145], [147]. For this study a wide range of pressures, including extremes, were coupled with the use of shear derived pressure on the side of the cancerous region. Such experimental conditions were established in order testing the total capabilities of the system while providing the greatest amount of control over the system as a whole. The use of more physiologically relevant pressure ranges and use of protein concentration gradients to drive the pressure differences in the system would be more realistic [142], [148], [149].

3.3.2 Cell confluency measurements

Cell confluency was measured using a plasma membrane stain, fluorescence imaging and confocal microscopy throughout time-course treatments with anti-cancer therapeutics. From the scans and images collected, the degree of cell monolayer coverage was measured as the area covered by cells expressed as a percentage of the whole viewing area. When only BAOECs were cultured within the devices the cell coverage was determined to be 97.5%. However, when HCT116s were introduced and grown in the basal channel, the degree of cell monolayer confluency dropped to 67.8%. Subsequent treatment of the diseased condition resulted in a steady increase in cell area coverage over the course of 120 hours, back to similar conditions prior to introduction of the HCT116s. These changes in cell area coverage throughout Paclitaxel (Fig 3.5(A)) and Doxorubicin (Fig 3.5(B)) treatment can be seen in Fig 3.5.

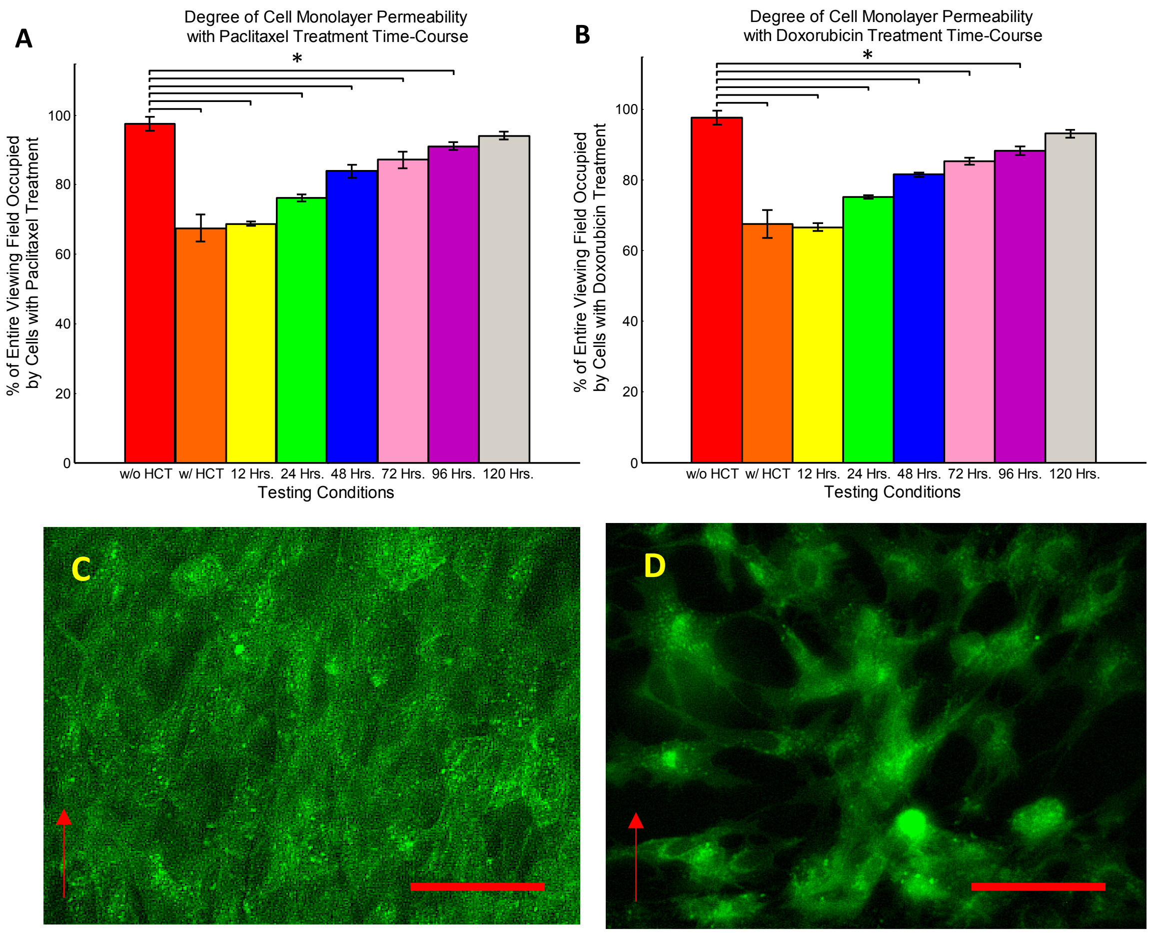

Figure 3.5 Normalized percentage of BAOEC monolayer permeability under various culturing conditions. Data shown as sum of means ± S.D. (n=5 independent microfluidic devices) for each image collection method. (A) Percentage of confluent BAOEC monolayer intact without HCT116s, with HCT116s, after treatment with Paclitaxel, and after treatment with Doxorubicin for 24 hours, measured as a percentage of the entire imaging field, collected via standard fluorescent microscopy. One way ANOVA statistical analysis with statistical significance indicated by * brackets in plot at $p \leq 0.05$. Sample collection was carried out from 5 independent devices (biological replicates). All statistical tests have been justified as appropriate. (B) Percentage of intercellular gap coverage without HCT116s, with HCT116s, after treatment with Paclitaxel, and after treatment with Doxorubicin, measured as a percentage of the entire imaging field, collected via fluorescent confocal microscopy. One way ANOVA statistical analysis with statistical significance indicated by * brackets in plot at $p \leq 0.05$. Sample collection was carried out from 5 independent devices (biological replicates). All statistical tests have been justified as appropriate. (C) Representative fluorescent image of highly confluent BAOEC monolayer prior to introduction of HCT116s into the device. Cells in image were stained with Cell Tracker Green and red arrow indicates direction of flow within the channel. (D) Representative fluorescent image of permeabilized BAOEC monolayer after introduction of HCT116s into the device. Cells in image were stained with Cell Tracker Green and red

arrow indicates direction of flow within the channel. Both red scale bars are 50μm in length.

Complementary data were collected from confocal scans where conditions without HCT116s grown in the devices resulted in a low gap coverage of 2.8%. However, when HCT116s were introduced into the channels, the gap coverage increased to 37.9% as can be seen in Fig 3.6. Both testing conditions and methods of data collection produced similar results indicating that the technique for quantifying the degree of BAOEC monolayer permeability functions well.

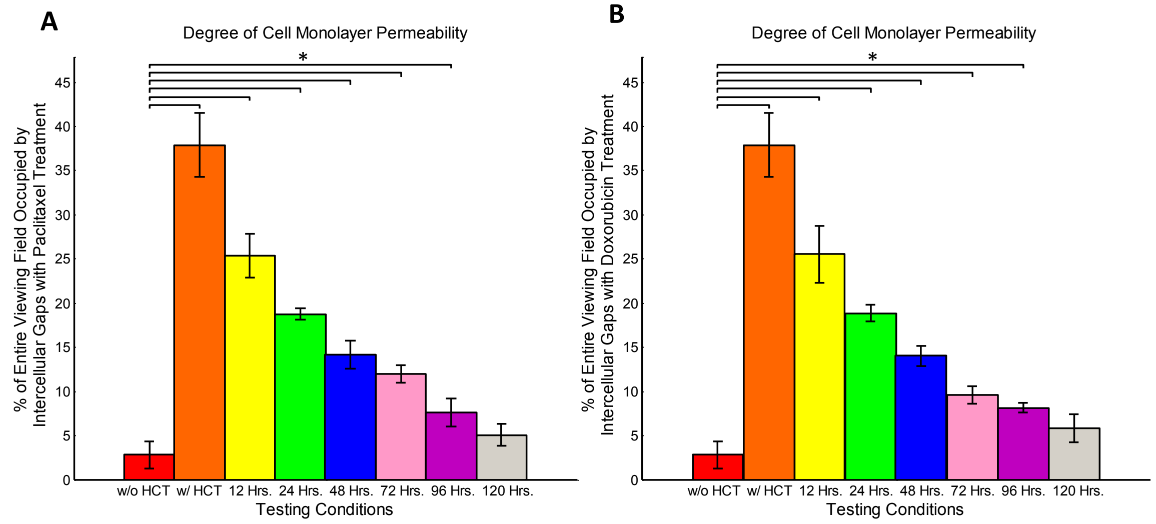

Figure 3.6 BAOEC monolayer permeability under various device conditions and therapeutic treatment times. (A) Percentage of intercellular gaps present within the viewing field throughout the time-course Paclitaxel treatment. One way ANOVA statistical analysis with statistical significance indicated by * brackets in plot at $p \leq 0.05$. Sample collection was carried out from 5 independent devices (biological replicates). All statistical tests have been justified as appropriate. (B) Percentage of intercellular gaps present within the viewing filed throughout the time-course Doxorubicin treatment. One way ANOVA statistical analysis with statistical significance indicated by * brackets in plot at $p \leq 0.05$. Sample collection was carried out from 5 independent devices (biological replicates). All statistical tests have been justified as appropriate.

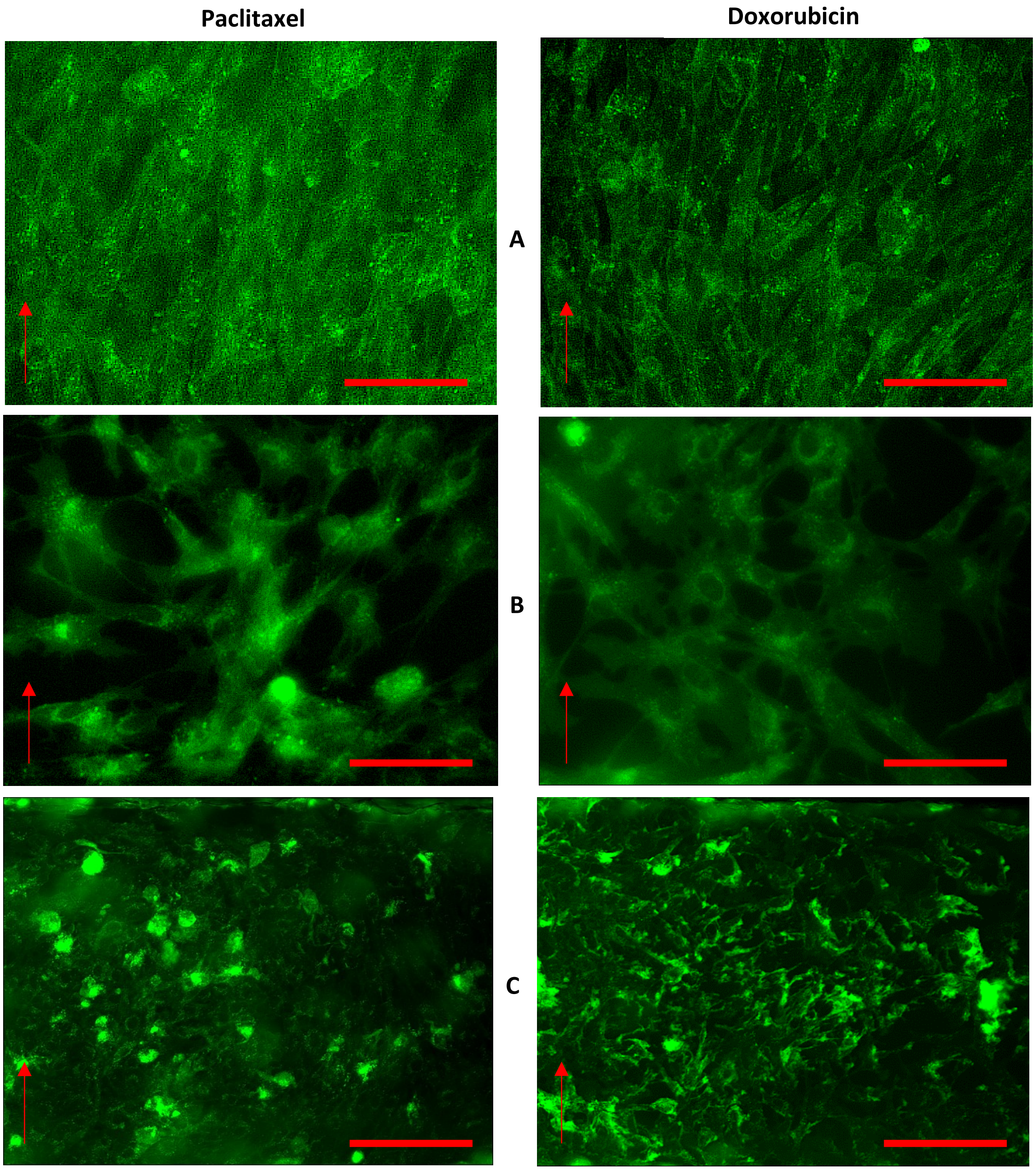

Figure 3.7 Representative fluorescent images of BAOEC monolayers grown in bi-layer microfluidic devices under various culturing conditions stained with Cell Tracker Green plasma membrane dye. (A left), BAOEC monolayer before introduction of HCT116s and Paclitaxel. (A right), BAOEC monolayer before introduction of HCT116s and Doxorubicin. (B left), BAOEC monolayer after introduction of HCT116s for 24 hours and before introduction of Paclitaxel. (B right), BAOEC monolayer after introduction of HCT116s for 24 hours and before introduction of Doxorubicin. (C left), BAOEC monolayer after introduction of HCT116s for 24 hours followed by flow of Paclitaxel for 48 hours. (C right), BAOEC monolayer after introduction of HCT116s for 24 hours

followed by flow of Doxorubicin for 48 hours. Red arrows indicate direction of flow established within device. All red scale bars are 50μm in length.

Representative images of typical results experienced under conditions when only BAOECs were grown in the device, as well as typical results experienced under conditions when BAOECs and HCT116s were grown in the device can be seen in Fig 3.5(C) and (D), respectively, along with Fig 3.7. Fig 3.5(C) clearly shows a highly confluent monolayer of BAOECs aligned with the direction of flow indicated by the red arrow. Dark spots between cells indicate that gaps are present in very low numbers and are small in size. Conversely, Fig 3.5(D) shows sparsely spaced BAOECs with large dark gaps present between individual cells. In addition to standard fluorescence microscopy, representative confocal scans of highly permeabilized BAOEC monolayers were obtained and can be observed in Fig 3.8. Verification of the effect of paclitaxel and doxorubicin on the HCT116 cancer cells utilized in the study can be observed in Fig 3.3, where application of either anti-cancer drug resulted in HCT116 death over time. Additionally, the effect of paclitaxel and doxorubicin on BAOECs was verified over time. BAOECs were grown within microfluidic channels and subjected to culture media shear flow (200sec^{-1}) containing anti-cancer therapeutics. The concentrations of the therapeutics used and the durations of the flow tests were held constant with all other testing. The presence of the anti-cancer therapeutics was shown to influence the survival and confluency of BAOECs grown within microfluidic devices. Treatment of the BAOECs occurred over the course of 120 hours without the presence of any cancer cells in order to quantify the effect of the therapeutics on endothelial cells. The resulting data indicated a slight increase in cell count over the first 24 hours of treatment with the therapeutics. Further treatment of the ECs with therapeutics over the full 120 hours resulted in slight reductions of the cell counts. ECs treated over the same 120 hour timeframe with standard culture media displayed improved growth which slowed over time as the ECs become more and more confluent within the devices. Likewise, when analyzing the coverage area of the EC monolayers as percentages over the time-course treatments, an initial increase was observed over the first 24 hours followed by a reduction in the percentage of the area covered. The data and representative images relating to the BAOECs response to anti-cancer therapeutics can be observed in Fig 3.9.

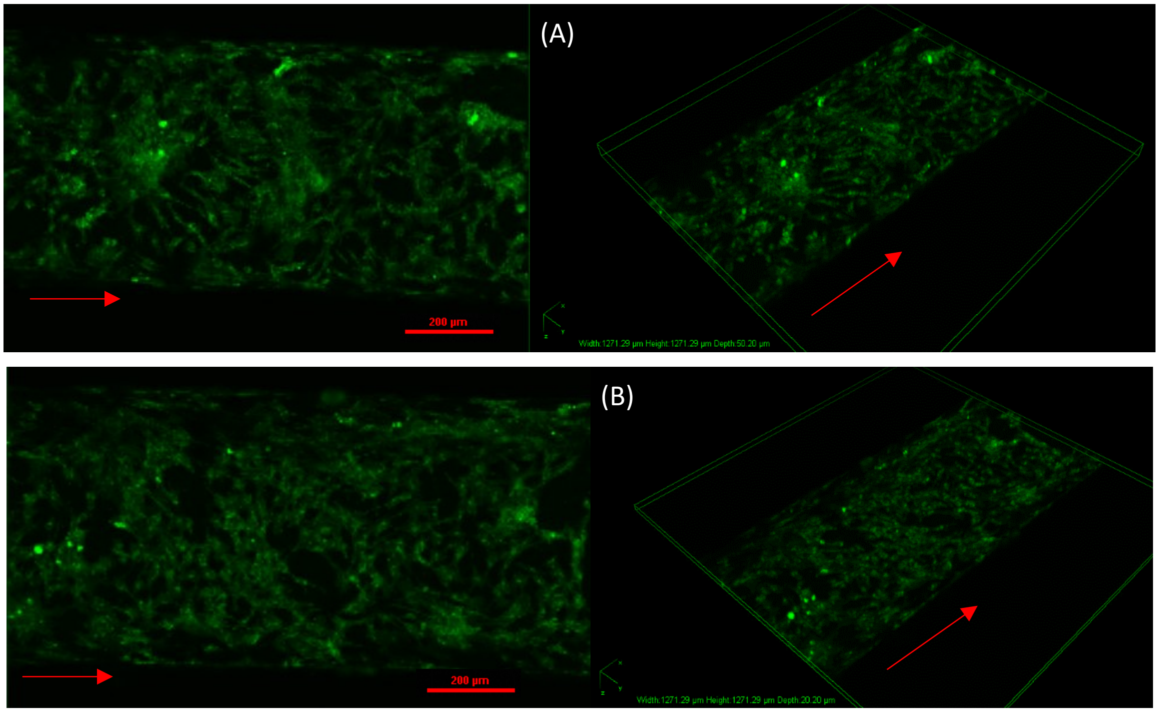

Figure 3.8 Representative fluorescent confocal images of BAOEC monolayers grown in bi-layer microfluidic devices under various culturing conditions. (A) BAOEC monolayer after introduction of HCT116s for 24 hours and before introduction of Paclitaxel. (B) BAOEC monolayer after introduction of HCT116s for 24 hours and before introduction of Doxorubicin. Red arrows indicate direction of flow established within device. Scale bars: 200 micrometers.

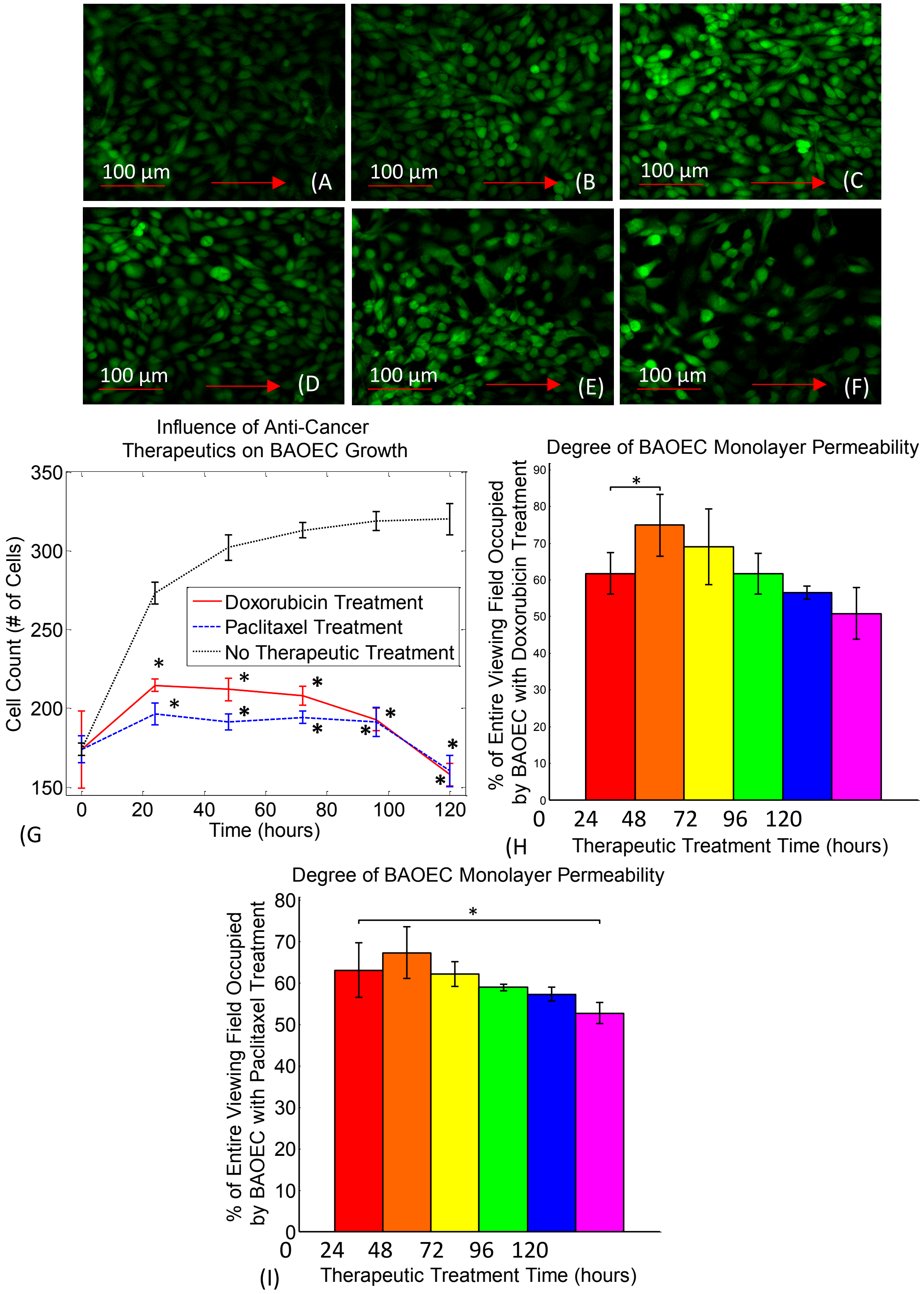

Figure 3.9 BAOEC monolayers subjected to anti-cancer therapeutic flows. (A-F) Representative images of BAOEC monolayers after being subjected to Doxorubicin for 0

(A) 24 (B) 48 (C) 72 (D) 96 (E) and 120 hours (F). Red arrows indicate direction of flow. Scale bars: 100 micrometers. (G) BAOEC cell counts after exposure to anti-cancer therapeutics for various durations. One way ANOVA statistical analysis with statistical significance indicated by * in plot at $p \leq 0.05$. Sample collection was carried out from 5 independent devices (biological replicates). All statistical tests have been justified as appropriate. (H) Percentage of BAOEC monolayer intact throughout Doxorubicin treatment time-course. (I) Percentage of BAOEC monolayer intact throughout Paclitaxel treatment time-course. One way ANOVA statistical analysis with statistical significance indicated by * brackets in plot at $p \leq 0.05$. Sample collection was carried out from 5 independent devices (biological replicates). All statistical tests have been justified as appropriate.

3.3.3 Dye transport under equal flow rates and pressures

Bi-layer microfluidic devices were utilized to track dye transport from the apical channel into the basal channel under various experimental conditions. The specific dyes used in these studies were FITC, FITC-Dextran 4kDa, and FITC-Dextran 70kDa, chosen for their increasing size and molecular weight in order to mimic various small and large molecule therapeutic candidates. Additionally channel flow rates of 9190, 70150, and 253050 μL/hr which correspond to average channel pressures of 632.8, 4832.4, and 17431.2 Pascals (Pa), respectively, were chosen to investigate the influence of a wide range of flow/pressure on therapeutic transport. The following figures contained in Fig 3.10 plot out the normalized dye transport averaged across all testing conditions, using the confluent BAOEC monolayer testing conditions as a baseline (set equal to 1). All of the dye transport data collected has additionally been normalized to account for any loss of dye due to binding with channel walls or cells.

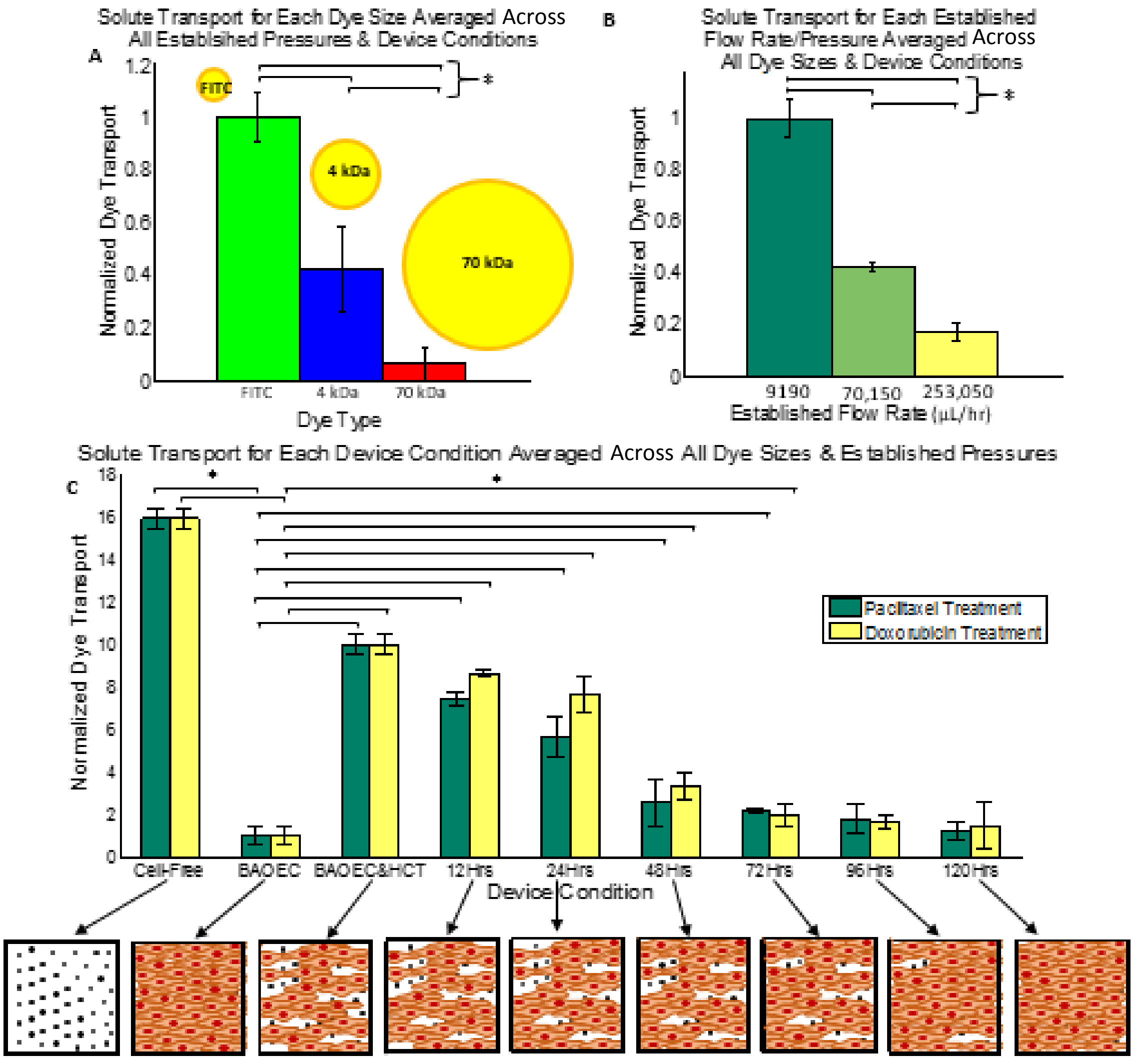

Figure 3.10 Averaged and normalized dye transport based on solute size, established pressure, and device condition for equal pressure tests. Data shown as sum of means ± S.D. (n=15 independent microfluidic devices) for each image collection method. (A) Overall degree of dye transport based on dye size, averaged over all established channel pressures and device conditions tested. Statistical significance of $p<0.05$ indicated by *. (B) Overall degree of dye transport based on established channel flow rates, averaged over all dye sizes and device conditions tested. Statistical significance of $p<0.05$ indicated by *. (C) Overall degree of dye transport based on device condition, averaged over all dye sizes and established channel pressures tested. Statistical significance of $p<0.05$ indicated by *. Schema of typical device conditions depicted for each step of the time-course treatment data.

Fig 3.10(A) depicts the averaged dye transport achieved based on varying dye sizes. The data points represented in the figure are the average values from all tests run at various pressures and under various device conditions. The figure shows that on average, across all other testing conditions, the smallest FITC dye underwent the greatest degree of transport across the EC monolayer. Subsequently, the FITC-Dextran 4kDa and FITC-Dextran 70kDa dyes underwent less transport respectively. This trend based on dye size was observed for equal pressure testing due to diffusion which acts as the main driving factor for transport when no pressure gradient exists across the membrane. The amount of dye in each flow test was held constant and due to its small size, the FITC dye was able to undergo the greatest diffusion and subsequent transport when compared to the two larger dyes. Next, we turn our focus onto the influence of established pressures on the overall transport observed.

Fig 3.10(B) depicts the averaged and normalized dye transport achieved under various pressures established within the channels. It should be noted that no pressure gradient exists across the semi-permeable membranes in this work. As such, the pressures within both the apical and basal channels are changed equally to ensure no flow driven transport of dye occurs. When comparing the degree of dye transport it is shown that the lowest pressure established resulted in the greatest amount of dye transport across all dye sizes and device conditions. Generally, the trend shows that increasing pressures within the channels results in lower transport regardless of dye size. The reason why this trend is observed is again due to the fact that the total amount of dye introduced during each test was held constant. As such, the total duration of the higher pressure flows was shorter when compared to the lower pressure tests due to the manner in which pressure is established in each channel. The shorter period of flow for the higher pressure cases results in less time for the dyes to undergo diffusion which ultimately results in less overall transport. If all established pressures for each dye test were given equal flow durations through the channels, the observed difference in transport would not be present, as demonstrated in Fig 3.11. Lastly for the equal pressure tests, the degree of dye transport achieved under various device conditions was examined.

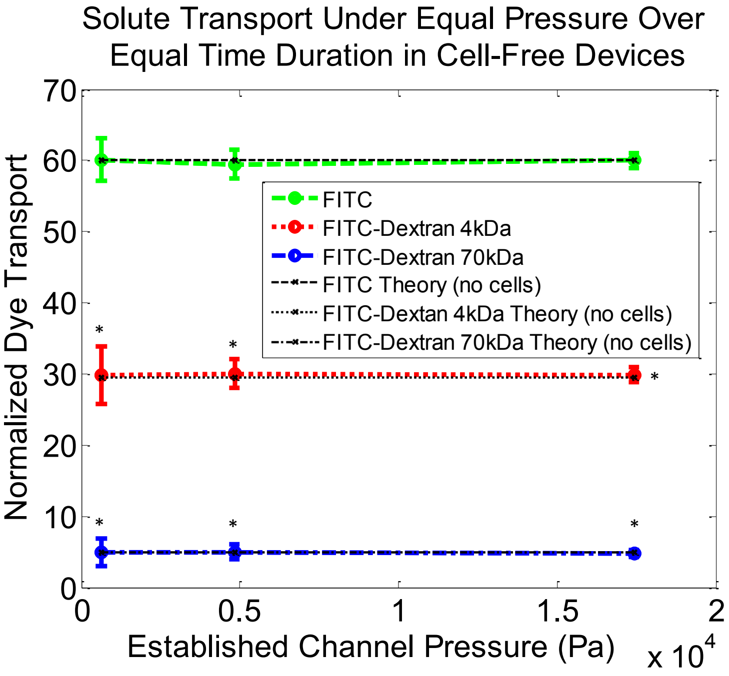

Figure 3.11 Normalized dye transport under various equal pressures for FITC, FITC-Dextran 4kDa, and FITC-Dextran 70kDa dyes flown through bi-layer microfluidic devices. Data shown as sum of means ± S.D. (n=5 independent microfluidic devices). Dye transport over various equal pressure conditions. One way ANOVA statistical analysis with statistical significance indicated by * in plot at $p \leq 0.05$ between baseline FITC dye tests and other dye sizes. Sample collection was carried out from 5 independent devices (biological replicates). All statistical tests have been justified as appropriate.

Fig 3.10(C) depicts the normalized transport achieved under various device conditions which has been averaged for all dye sizes run and all pressures tested within the devices under equal pressure conditions. From the figure it is observed that a large degree of transport occurs when no cells are present within the devices, as expected. Subsequent addition of an EC monolayer resulted in a drastic reduction of overall transport regardless of dye size. Later addition of cancer cells into the basal channel of the devices resulted in an increase in overall transport on average by a factor of around 6. After the addition of cancer cells, treatment with either paclitaxel or doxorubicin over the course of 120 hours showed a slow drop in the amount of total transport. After a full 120 hours of treatment, the observed dye transport was reduced to conditions experienced with a confluent monolayer of ECs prior to the introduction of cancerous cells. Fig 3.10(C) contains a representative schema for each condition of the devices throughout the establishment of an EC monolayer, establishment of a cancerous region, and subsequent time-course treatment with therapeutics. It should be noted for Fig 3.10(C) that no statistically significant difference existed between the overall transport observed during the time-course treatments with paclitaxel and doxorubicin.

Lastly, it should be noted that cell-free device conditions without cells were run in order to verify that the resistance of the membrane incorperated into the microfluidic system was in the same order of magnitude as values reported in literature for *in vivo* tumors [150]–[153], and to function as benchmark testing cases. Additionally, breakdowns of specific data for before averages were calculated across features such as dye size, pressure, or device condition can be seen in Fig 3.12 through Fig 3.14.

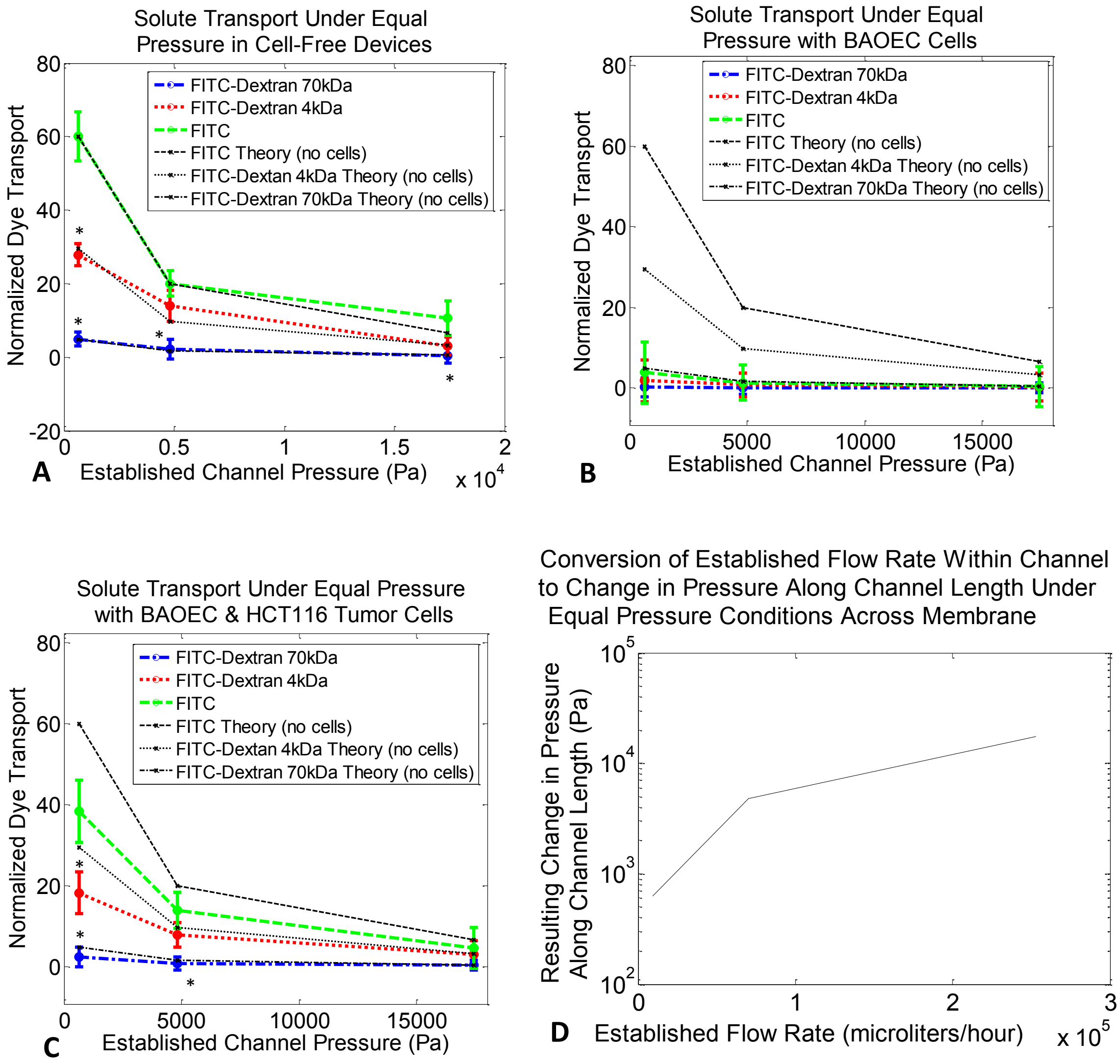

Figure 3.12 Normalized ratio of basal solute concentration to stock solute concentration under various equal pressures across the membrane for FITC, FITC-Dextran 4kDa, and FITC-Dextran 70kDa dyes flown through bi-layer microfluidic devices of different conditions. Pressures shown are in addition to physiologically normal pressure value of 10666Pa. Data shown as sum of means ± S.D. (n=5 independent microfluidic devices) over duration of measurement collection. (A) Bare bi-layer microfluidic devices. One way ANOVA statistical analysis with statistical significance indicated by * in plot at $p \leq 0.05$ between baseline FITC dye tests and other dye sizes. Sample collection was carried out from 5 independent devices (biological replicates). All statistical tests have been justified as appropriate. (B) Bi-layer microfluidic devices containing only an apical BAOEC monolayer. One way ANOVA statistical analysis with statistical significance indicated by * in plot at $p \leq 0.05$ between baseline FITC dye tests and other dye sizes. Sample collection was carried out from 5 independent devices (biological replicates). All statistical tests have been justified as appropriate. (C) Bi-layer microfluidic devices containing an apical BAOEC monolayer and basal HCT116 monolayer. One way ANOVA statistical analysis

with statistical significance indicated by * in plot at $p \leq 0.05$ between baseline FITC dye tests and other dye sizes. Sample collection was carried out from 5 independent devices (biological replicates). All statistical tests have been justified as appropriate. Theoretical values for dye transport under conditions of bare microfluidic devices are plotted for (A) through (C) as a guide for comparative purposes between plots. (D) Plot comparison for effect flow rate established within microfluidic channel on the pressure change established along the length of the device. $p<0.05$ by one way ANOVA tests for dye concentration data compared between dye sizes at various pressure differentials.

A

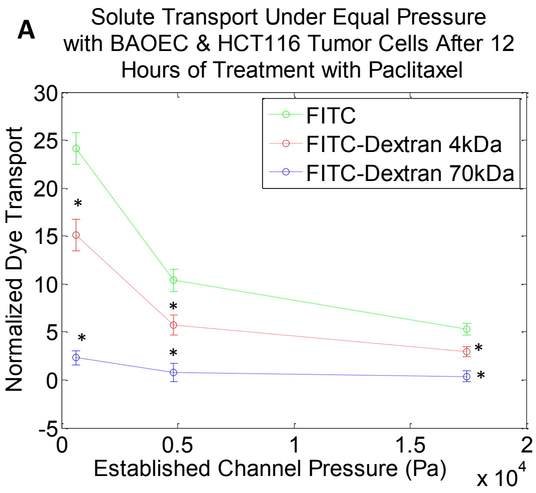
Solute Transport Under Equal Pressure with BAOEC & HCT116 Tumor Cells After 12 Hours of Treatment with Paclitaxel

B

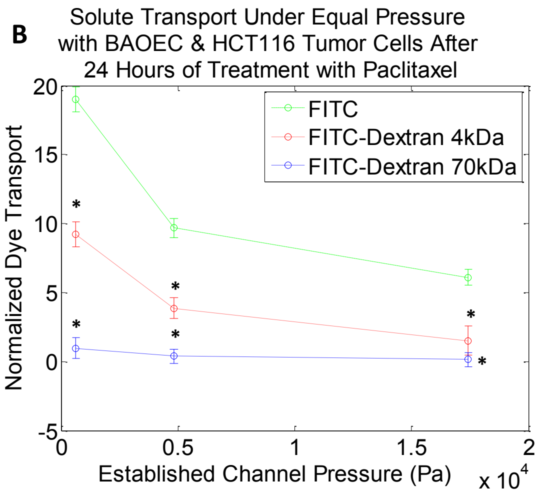
Solute Transport Under Equal Pressure with BAOEC & HCT116 Tumor Cells After 24 Hours of Treatment with Paclitaxel

C

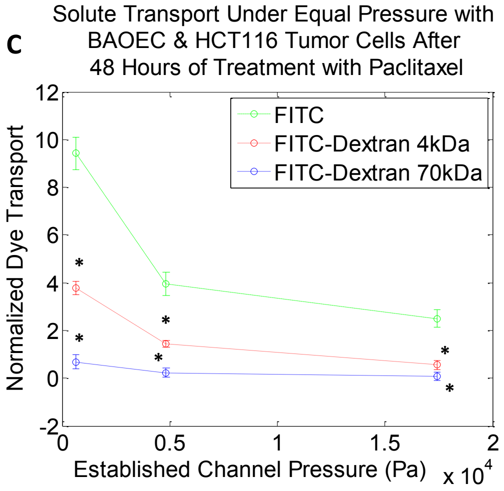
Solute Transport Under Equal Pressure with BAOEC & HCT116 Tumor Cells After 48 Hours of Treatment with Paclitaxel

G

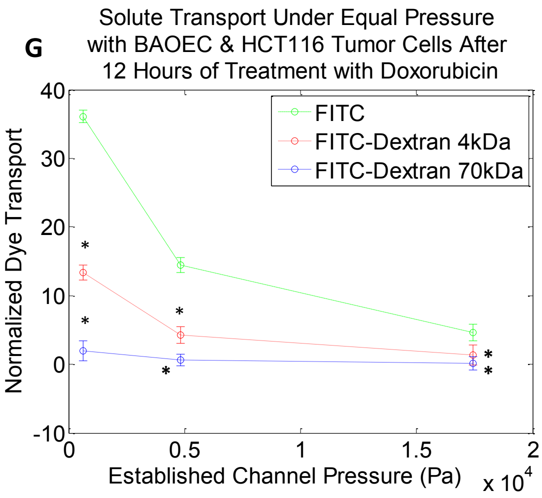
Solute Transport Under Equal Pressure with BAOEC & HCT116 Tumor Cells After 12 Hours of Treatment with Doxorubicin

H

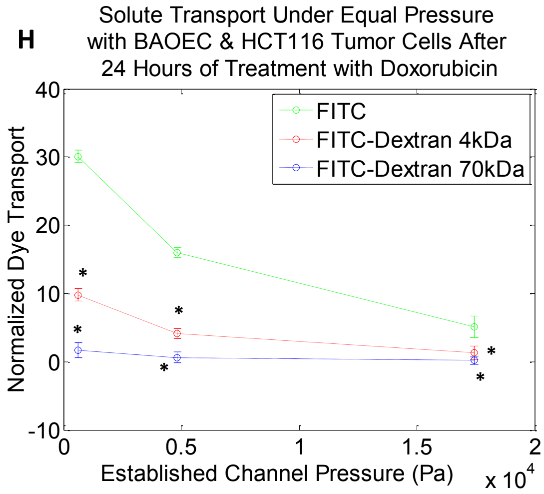
Solute Transport Under Equal Pressure with BAOEC & HCT116 Tumor Cells After 24 Hours of Treatment with Doxorubicin

I

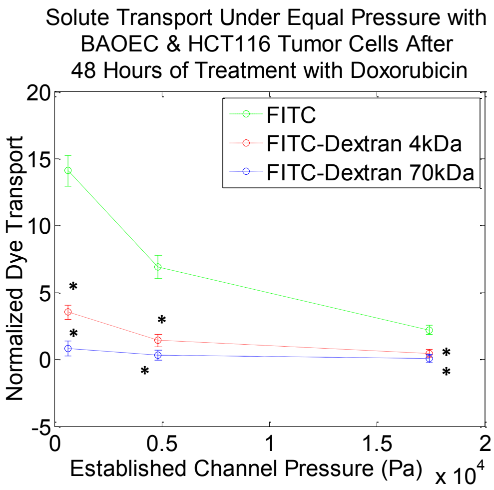
Solute Transport Under Equal Pressure with BAOEC & HCT116 Tumor Cells After 48 Hours of Treatment with Doxorubicin

D

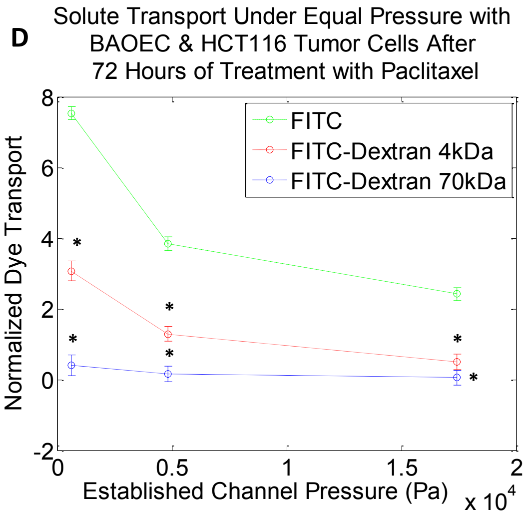
Solute Transport Under Equal Pressure with BAOEC & HCT116 Tumor Cells After 72 Hours of Treatment with Paclitaxel

J

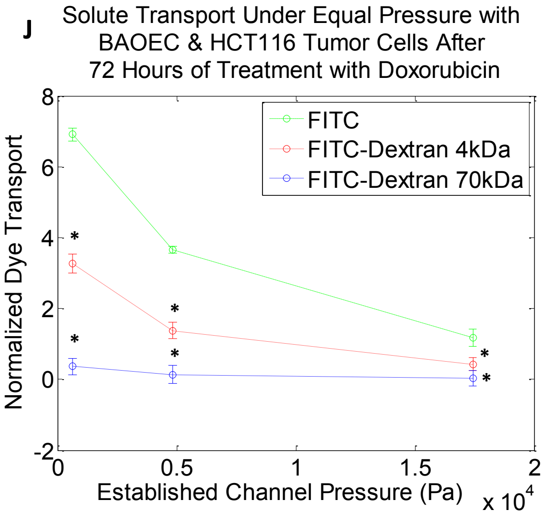
Solute Transport Under Equal Pressure with BAOEC & HCT116 Tumor Cells After 72 Hours of Treatment with Doxorubicin

E

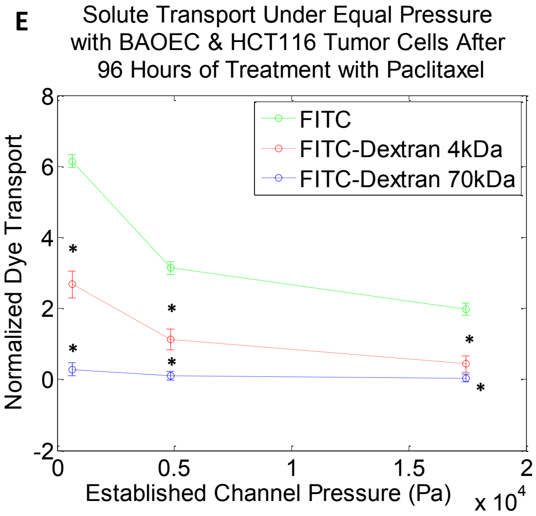
Solute Transport Under Equal Pressure with BAOEC & HCT116 Tumor Cells After 96 Hours of Treatment with Paclitaxel

K

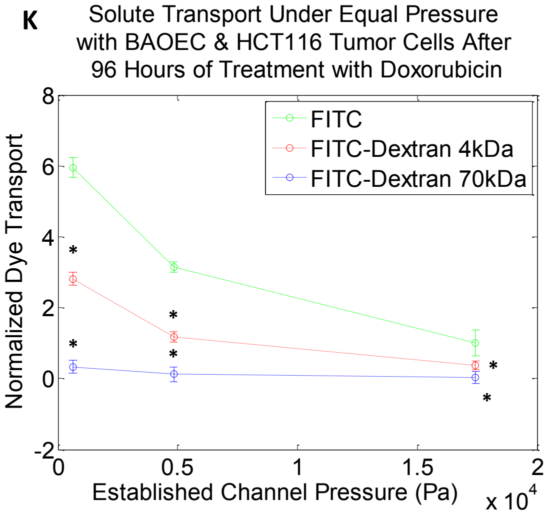
Solute Transport Under Equal Pressure with BAOEC & HCT116 Tumor Cells After 96 Hours of Treatment with Doxorubicin

F

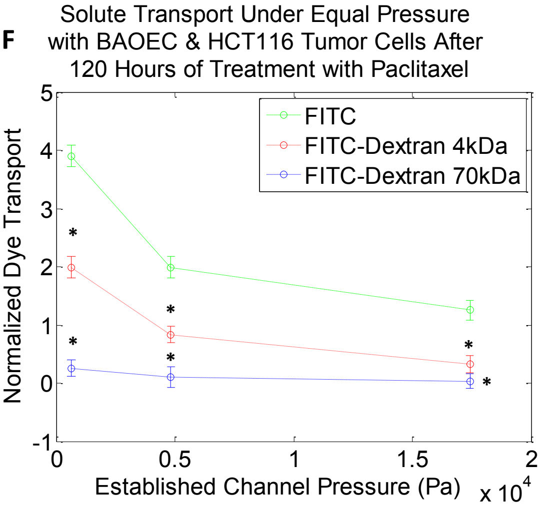
Solute Transport Under Equal Pressure with BAOEC & HCT116 Tumor Cells After 120 Hours of Treatment with Paclitaxel

L

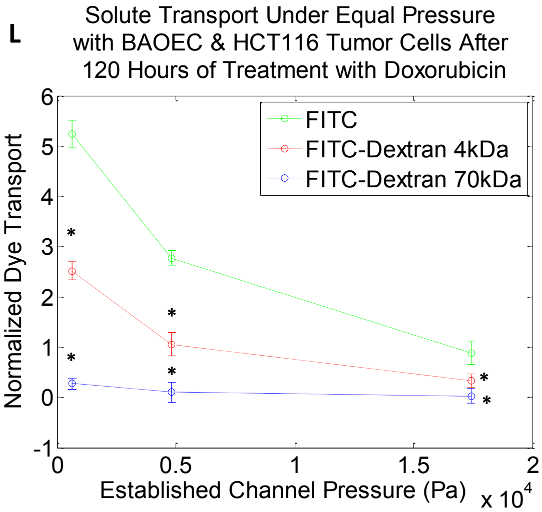
Solute Transport Under Equal Pressure with BAOEC & HCT116 Tumor Cells After 120 Hours of Treatment with Doxorubicin

Figure 3.13 Normalized ratio of basal solute concentration to stock solute concentration under various equal pressures across the membrane for FITC, FITC-Dextran 4kDa, and FITC-Dextran 70kDa dyes flown through bi-layer microfluidic devices with BAOEC monolayer in apical channel and HCT116 monolayer in basal channel at various time points post-treatment with anti-cancer therapeutics. Data shown as sum of means ± S.D. (n=5 independent microfluidic devices) over duration of measurement collection. (A) Dye transport after 12 hours of treatment with Paclitaxel. (B) Dye transport after 24 hours of treatment with Paclitaxel. (C) Dye transport after 48 hours of treatment with Paclitaxel. (D) Dye transport after 72 hours of treatment with Paclitaxel. (E) Dye transport after 96 hours of treatment with Paclitaxel. (F) Dye transport after 120 hours of treatment with Paclitaxel. (G) Dye transport after 12 hours of treatment with Doxorubicin. (H) Dye transport after 24 hours of treatment with Doxorubicin. (I) Dye transport after 48 hours of treatment with Doxorubicin. (J) Dye transport after 72 hours of treatment with Doxorubicin. (K) Dye transport after 96 hours of treatment with Doxorubicin. (L) Dye transport after 120 hours of treatment with Doxorubicin. For all testing conditions and plots above, one way ANOVA statistical analysis with statistical significance indicated by * in plots at $p \leq 0.05$ between baseline FITC dye tests and other dye sizes. Sample collections were carried out from 5 independent devices (biological replicates) for each test. All statistical tests have been justified as appropriate.

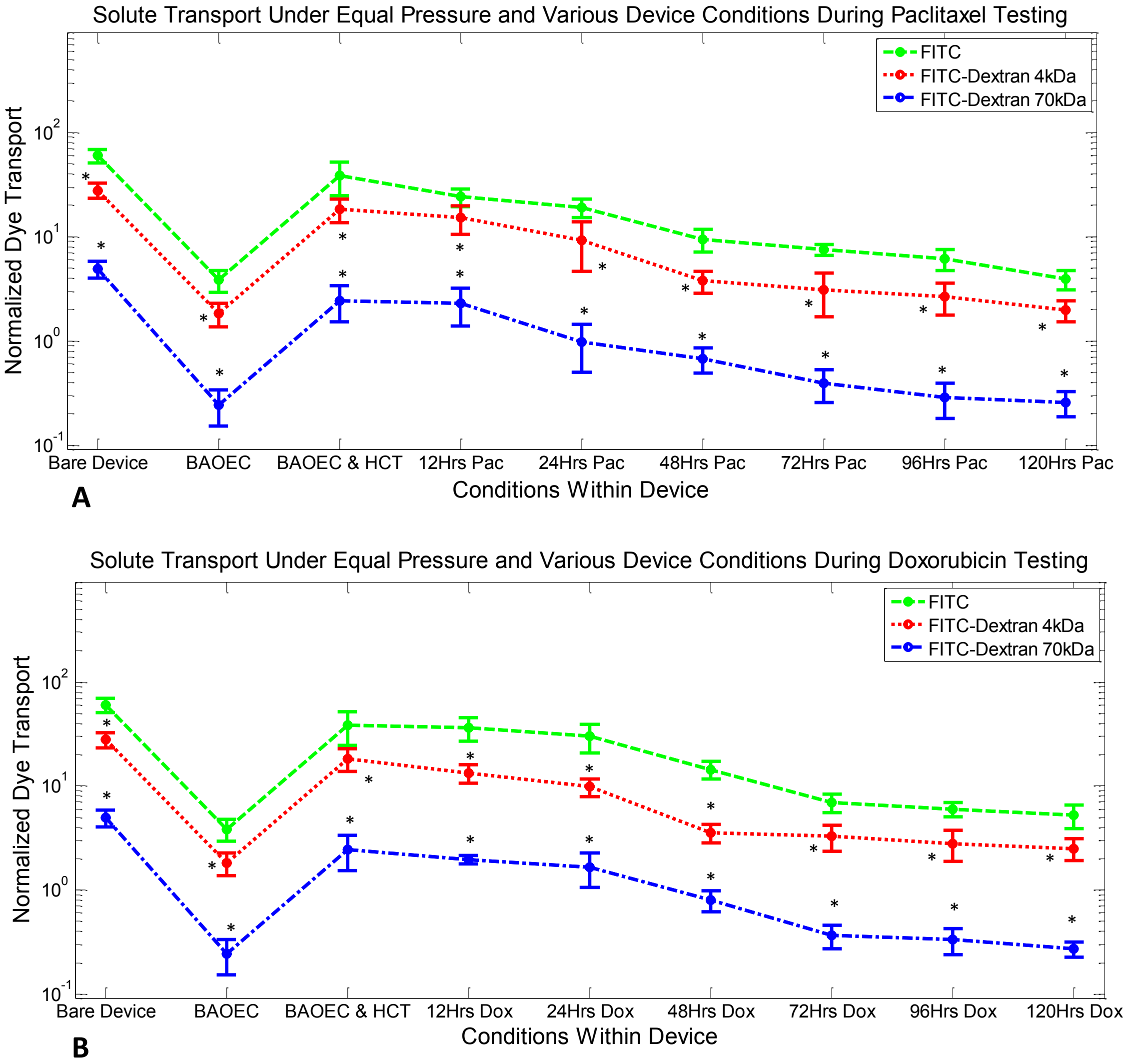

Figure 3.14 Normalized ratio of basal solute concentration to stock solute concentration time-course under various device conditions and equal pressure across (632.8 Pa + 10666 Pa) the membrane for FITC, FITC-Dextran 4kDa, and FITC-Dextran 70kDa dyes flown through bi-layer microfluidic devices. Data shown as sum of means ± S.D. (n=5 independent microfluidic devices) over duration of measurement collection. (A) Dye transport with eventual treatment with Paclitaxel. One way ANOVA statistical analysis with statistical significance indicated by * in plot at $p \leq 0.05$ between baseline FITC dye tests and other dye sizes. Sample collection was carried out from 5 independent devices (biological replicates). All statistical tests have been justified as appropriate. (B) Dye transport with eventual treatment with Doxorubicin. One way ANOVA statistical analysis with statistical significance indicated by * in plot at $p \leq 0.05$ between baseline FITC dye tests and other dye sizes. Sample collection was carried out from 5 independent devices (biological replicates). All statistical tests have been justified as appropriate.

3.4 Conclusions

From this work, a platform for studying transport phenomenon in a bi-layer microfluidic device is offered which allows for co-culturing of a variety of cell types. The overall goal of the study was to demonstrate the influences of factors, such as the presence of cancerous cells and established pressures, on the transport of dyes and therapeutic agents in a mimicked blood vessel. The system has also been shown to allow for physiologically relevant flow in the apical channel mimicking microvasculature blood flow and shear. While some portions of the system are held to physiologically relevant conditions, there are several features which are tested over wider ranges for the sake of testing the systems capabilities. The total range, magnitude, and method of generating oncotic pressure in this work are examples of conditions not strictly held to physiologically relevant values. Studying the responsiveness of the system over a wider range of values provided verification that the system is capable of being applied to different disease conditions beyond the scope of cancer microenvironments. Additionally, the unrealistic approach of controlling pressure differences between channels via shear flow allows for more precise regulation when compared to physiological oncotic pressure controlled mainly by protein concentration gradients [142], [145], [147], while also providing a means of maintaining a constant therapeutic flux. The use of bovine endothelial cells as opposed to human derived endothelial cells in this work introduces the possibility of variations in observed results stemming from interspecies differences in EC responses to human cancer cell cytokines, inflammatory agents, antibody interactions and therapeutic agents [154]–[156]. In order to facilitate more reliable data collection, future uses of the developed microfluidic system will incorporate the use of human derived endothelial cells such as human umbilical vein endothelial cells (HUVECs). Facilitating the future growth of human derived endothelial cells will require improvements to our microfluidic device performance and functionality in order to ensure that healthy and confluent cultures of human endothelial cells can be grown. As a final note, the use of a semi-permeable membrane within the bi-layer microfluidic model also introduces a physical barrier which is not found *in vivo* and as such introduces an added resistance to the transport of dye and therapeutic molecules. Ideally, such a microfluidic model would be capable of growing a self-supported tubular vessel comprised of human derived endothelial cells, in turn preventing any added resistance to the transport of materials across the device. As such, it should be noted that the observed permeability measurements are lower than what would be expected *in vivo*. This occurs because transport within the boundary of any gaps formed between endothelial cells should occur in an unrestricted manner, however, the presence of the semi-permeable membrane restricts the total free area in the cell monolayer gap resulting in a higher resistance and overall reduced transport. Future improvements of the techniques utilized to produce microvasculature within the bi-layer microfluidic system will allow for these issues to be resolved in order to better mimic conditions experienced *in vivo*.

The microfluidic system has been shown to allow for the monitoring of EC permeability and confluency which can be varied based on conditions established within the system. Use of serum-conditioned culture media as opposed to whole blood facilitated ease of use related to data collection and imaging without interference of blood cells, while still providing many of the proteins and small molecule components found in blood plasma. Specifically, the ability to quantify EC monolayer coverage when isolated, exposed to cancerous cells and throughout the anti-cancer treatment process has been demonstrated.

EC coverage was shown to be maximized when only ECs were grown within the apical channel covering nearly 100% of the entire channel. However, upon introduction of HCT116s, the EC coverage dropped to around 65% coverage. The initial EC coverage near 100% was achieved because no cytokines or permeabilizing agents were present within the devices. Later introduction of HCT116s into the basal channels resulted in the release of cytokines and permeabilizing agents into the system. As such, the diffusion and transport of the cytokines/permeabilizing agents to the apical channel resulted in a high degree of EC permeability. Subsequent treatment of the system with either paclitaxel or doxorubicin over 120 hours resulted in the slow recovery of the EC coverage back to conditions of nearly 100% coverage. Treatment with either anti-cancer drug, assisted in the recovery of EC confluency by functioning to kill off the HCT116s growing within the system. As HCT116s were killed off by therapeutics, the production and excretion of cytokines/permeabilizing agents was reduced in turn allowing for EC recovery. It should be noted that the usage of endothelial cells within the microfluidic system was carried out in the form of cell monolayers as opposed to tubular structures. The subsequent use of EC monolayers in turn is recognized to have the potential to influence the performance of the system by altering the regulation of cell-cell and cell-matrix adhesion characteristics based on matrix dimensionality (2D vs. 3D) [157]. In addition, it is recognized that the use of endothelial cell monolayers, limits the functionality of the microfluidic system due to the rapid loss of tissue-related functions which impairs the predictive capabilities of the system as a whole [158]. The use of a three dimensional growth system to form endothelial tubes is preferred in order to better mimic EC responses to permeabilizing agents and shear while ensuring that no impairment of the systems predictive capabilities occurs. As such three dimensional tissue growth of endothelial cells into tubular structures will be adopted for future studies involving studies of vasculature.

In addition to observing the influence of the therapeutics on the cancer cells, flow tests were run in devices containing only ECs using therapeutic conditioned media. The resulting data showed initial increases in EC cell counts and confluency over the first 24 hours. Continued treatment showed slight decreases in cell counts and confluency as a result of the therapeutics presence. The exposure of ECs to therapeutics slowed their normal growth as apparent when comparing the growth curves of cells treated with standard media and those treated with therapeutic conditions media as seen in Fig 3.9. The slow of EC growth and slight reduction in cell counts agrees well with previous findings in literature and is known to occur as a result of the manner in which the two therapeutics function to cause cell death [159]–[162]. In addition, only slight variations in EC confluency were noted as a result of being exposed to the therapeutics. The variations which were observed can be attributed to the combination of fluctuations in cell counts and changes in EC morphology. The scale of fluctuation in EC permeability resulting from the therapeutics alone was relatively low when compared to the fluctuations observed when cancer cells were present in the system. As such, the major focus of the work was geared around permeability induced by the presence of the HCT116 cancer cells. Overall, this work has shown that the system is able to function as a suitable method for observing cellular scale changes in EC confluency and permeability resulting from the presence of cancer cells and anti-cancer therapeutics. It should be noted that measurements of EC permeability were carried out with direct cell imaging measurements and indirectly via dye transport studies. The observed gaps which formed between ECs as a result of being exposed to cancerous cytokines and permeabilizing agents are what facilitated the apical to basal transport of the dyes used. The presence of a semi-permeable membrane in the microfluidic system was required to function as a physical substrate onto which ECs could anchor, which also serves to introduce a small amount of resistance to fully unrestricted dye transport. However, decisions on the pore size and density for the membranes was chosen to reduce the unavoidable transport resistance as much as possible. As such, this study focuses on quantifying the influence of factors such as cytokines/permeabilizing agents (resulting from cancerous disease conditions), pressure differentials, and shear flow on the observed permeability of the vascular endothelium to variously sized dye molecules. Beyond the scope of monitoring EC monolayer integrity, the system was shown to be capable of performing therapeutic/tracer delivery studies which will be discussed next.

Leveraging the ability to dictate precise pressures within both channels of the devices, a variety of equal pressure cases were tested to observe the effect of pressure/flow rate on therapeutic delivery. Given that the pressures established in each channel can be controlled independently, we chose to investigate the effects of various equal pressure test cases on therapeutic transport. In addition to the use of equal pressures, a range of dye sizes and device conditions were established in order to further understand how transport if influenced.

When considering the influence of solute size on transport, the maximum amount of transport observed occurred for FITC, followed by FITC-Dextran 4kDa, and FITC-Dextran 70kDa, respectively. This trend in transport is observed due to the dye molecules various sizes. The smallest FITC dye underwent the greatest transport because it is more freely able to diffuse through the system. The larger dyes take longer times to diffuse around in the system and as such, they undergo less transport over the same time-period. The large influence of dye size on the observed transport is credited to the fact that under equal pressure conditions, the main factors driving transport are the natural diffusion of the dyes and the concentration gradients which exist across the semi-permeable membrane. Since size plays a large role in dye diffusion, a large difference in transport is observed between the three dyes. In addition to dye size, the established pressures within the channels also largely influences transport.

The wide range of equal pressures tested resulted in differing degrees of transport. Given the resulting transport trend, it was observed that increasing the pressure within the system while still maintaining equal pressures on both halves of the device, resulted in reduced transport of dyes regardless of size. This trend was observed due to the fact that the total volume of dye suspension introduced into each device was held constant. As such, the increased pressures being generated by increased flow rates, resulted in less time for the dye molecules to diffuse while in the system. If the duration of flow for each pressure case was held constant instead of the total volume, then no difference in transport between established channel pressures would be expected, as verified via cell-free device testing data in Fig 3.11. Moving beyond the scope of established channel pressures, studies were conducted to identify the influence of system conditions on the transport of therapeutics.

From this section of the study, a range of system conditions were established including cell-free, EC confluent, EC and HCT116 diseased devices and the subsequent application of time-course therapeutic treatments. The greatest degree of dye transport was observed under device conditions containing no cells (cell-free) which agreed well with the predicted theoretical model based on the Kedem-Katchalsky transport equations [163] (see Fig

3.12(A)). Later establishment of an EC monolayer within the apical channel resulted in greatly reduced transport due to the formation of a confluent monolayer. The overall transport was reduced due to coverage of the pores present in the semi-permeable membrane by the ECs. Instead of being able to transport across the semi-permeable membrane, the dyes introduced into the apical channel were forced to exit the system from the apical channel outlet. These observed results agree well with trends published in similar studies utilizing microfluidic system to study endothelial permeability to tumor cells [164].

Further addition of HCT116s resulted in the partial recovery of transport within the system. The observed partial transport recovery is the result of cytokines and permeabilizing agents, released by the newly added HCT116s, functioning to permeabilize the EC monolayer. The formation of large gaps between ECs in the apical channel allowed for the exposure of pores in the membrane which in turn allowed for increased dye and therapeutic transport. Again, the observed results agree with previous literature findings using metastatic cancer cell lines, tumor conditioned media containing excreted cytokines/permeabilizing agents, and similar dye molecules [164]. Moving beyond the diseased state of the system, the application of anti-cancer therapeutics was investigated in order to verify that the system as a whole responds to the presence of therapeutic agents.

Paclitaxel and Doxorubicin were utilized to treat the cancerous regions of the devices in order to observe the recovery process of the EC monolayers. Subsequent treatment of the system with either of the therapeutics over the course of 120 hours resulted in the recovery of the EC monolayers as measured directly with imaging (see Fig 3.5) and indirectly via dye transport measurements. The observed increase in cancerous cell death upon treatment with either paclitaxel or doxorubicin agrees with other literature studies [165]–[168]. Additionally, the observed reduction in EC permeability during treatment with either of the anti-cancer therapeutics agrees with trends observed in literature [79], [128], [169], [170]. Time-course treatments were only run over the course of 120 hours because the EC permeability and dye transport were able to recover back to conditions similar to those experienced prior to the introduction of cancerous cells. Additionally, there exist other *in vivo* based tumor studies which have been run over the course of five to seven days, making the choice of 120 hours of treatment in our model suitable [134], [171]–[173].

Introduction of therapeutics into the apical channel along with dye molecules was performed in order to observe if the amount of transported dye would be influenced by the treatment of the diseased cancerous environment. Transport of the anti-cancer therapeutics across the membrane functioned to slowly kill off the HCT116s present in the basal channel of the devices. In turn the death of HCTs reduced the amount and degree of cytokine/permeabilizing agent secretion. The EC monolayers were shown to recover over the 120 hour treatment process as a result of HCT116 cell death. These results confirmed that the system was functioning to facilitate therapeutic transport across the EC monolayer and semi-permeable membrane. The observed changes in dye transport resulting from therapeutic treatment serve as an indirect technique for quantitatively analyzing the degree of EC permeability. Additionally, an understanding of how therapeutic treatments influence cancerous and endothelial cells can be gained through the use of the developed microfluidic system. As noted previously, the direct influence of the therapeutics on EC permeability have been quantified and should be given consideration when choosing potential anti-cancer therapeutic treatments for patients.

Overall, the developed microfluidic system has been shown to allow for the establishment of EC monolayers which are responsive to their local environment while also facilitating physiologically relevant flows in the apical channel. The additional ability to grow secondary cell types, such as cancerous cells, in close proximity to the mimicked blood vessel provides the opportunity to study interactions and responses between the chosen cell types. Further, the ability to precisely control and regulate pressures within each channel provides opportunities to study various disease conditions such as tumor microenvironments. In this work, we have utilized endothelial and tumor cells to establish a simplified tumor microenvironment in order to study endothelial responses to cancerous cells/anti-cancer therapeutics, the therapeutic delivery process in a mimicked vessel, and the responsiveness of HCT116 cells to treatment with paclitaxel and doxorubicin. It should be noted that this approach does not consider all conditions experienced in an *in vivo* tumor microenvironment. Furthermore, it is noted that certain parameters and conditions established within the system do not always fall within physiologically relevant ranges. The use of values outside of physiologically relevant ranges were performed for the sake of testing the system's functionality for potential work outside the scope of mimicking tumor microenvironments. Further advancements in the screening capabilities of the bi-layer microfluidic system required the analysis of nanoparticle therapeutic carriers as opposed to dye and free therapeutic molecules. As such, the next chapter demonstrates the functionality of the microfluidic system for analysis of nanoparticles of various shapes in order to achieve improved therapeutic delivery.

Chapter 4: The shape effect on polymer nanoparticle transport in a blood vessel

4.1 Introduction

Within biological models, the transportation and delivery of cellular building blocks, waste, and other materials is required in order to sustain life which in turn requires energy [174]–[178]. Biological models such as vesicle, virion, and DNA transport/translocation have adapted various techniques to accomplish transport tasks while expending as little energy as possible [179]–[181]. This invaluable evolutionary fine-tuning was turned toward when attempting to maximize the transport and delivery of therapeutics stored within nanoparticle carriers based on their shape. In order to compare various nanoparticle designs, a suitable biological model must be chosen which replicates many of the factors encountered within the system. A model mimicking microvasculature must be used which contains many characteristics of the biological model while not becoming overly complicated and difficult to sustain. Previous attempts in literature to mimic vasculature for the sake of nanoparticle analysis have been oversimplified with subpar results [46], [182]–[185].

Current techniques for investigating nanoparticle transport utilize living *in vivo* models which show targeting efficiency around or below 10% based on the amount of nanoparticles introduced into the system [186]–[188]. Such low efficiency of delivery to targeted sites is often due to particle shapes which are not suitable for delivering maximized drug loads while enhancing characteristics required for migration across biological barriers. Despite the poor efficiencies achieved in the past using synthetic designs, we turn to nature in order to overcome the challenge of nanoparticle transport across biological barriers. Specifically, vesicle and viral transport have adopted rod and filament-like carrier shapes in order to maximize the amount or volume of material being passed across a membrane while limiting the energy required to do so [176], [189]–[191]. Additionally, previously reported characteristics such as longer circulation times *in vivo* and lower rates of accumulation for larger sized filamentous particles in organs such as the liver, lungs and spleen are beneficial when delivering therapeutic loads [185], [189], [192], [193]. As such, the application of long filamentous nanoparticle carriers towards the goal of therapeutic delivery is of interest. Previous attempts in literature to design filamentous nanoparticles have occurred, however there has not yet been any systematic study towards the improvement of such delivery vehicles [185], [189], [192], [193].

In turn, this study investigates the effectiveness of spherical, short rod, and long rod particles in a variety of conditions experienced by nanoparticle carriers *in vivo*. The goal of this study is to identify which nanoparticle shape is able to most efficiently deliver therapeutics and to see if the evolutionary preference of long filamentous rods is ideal for the application of therapeutic delivery to diseased conditions. A range of *in vitro* based microfluidic experimental setups are utilized to mimic certain aspects of vasculature important for understanding the effectiveness of each nanoparticle shape towards maximizing therapeutic delivery, as seen in Fig 4.1. The developed microfluidic model serves as a biomimetic blood vessel testing platform which provides novel insight into nanoparticle performance by allowing for the direct quantification of various factors influencing transport. Factors such as nanoparticle binding, endothelial permeability, flow, and pressure conditions are all capable of being precisely measured and locally controlled which in turn allows for a more systematic study of nanoparticle transport efficiency. This novel approach to quantify nanoparticle transport performance allows for the maximization and enhancement of therapeutic delivery crucial for maintaining relatively low therapeutic loads which are safe for patients. From this work, we demonstrate the capabilities of the developed microfluidic system to quantify the influence of key factors on nanoparticle transport while drawing conclusions on which particle shape tested is most ideal for the therapeutic delivery process compared to the solution offered over time by biological evolution. We believe this to be the first work to quantitatively study the effect of particle shape on key factors influencing transport efficiency such as nanoparticle distribution, binding, degree of vascular permeability, along with controlled flow and pressure conditions in a mimetic platform mimicking the vascular system.

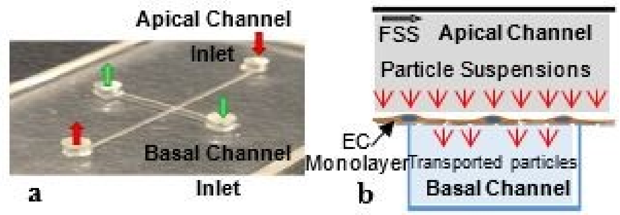

Figure 4.1 Microfluidic device design and channel orientation. (A) Image of bi-layer device showing apical and basal channel along with respective inlets and outlets. (B) Schematic depicting EC growth on semi-permeable membrane and nanoparticle suspension introduction and transport through intracellular gaps.

4.2 Experimental

4.2.1 Materials

The media used for HCT116 cells is Dulbecco's Modified Eagle's Medium (DMEM, Life Technology), with 10% fetal bovine serum (FBS, Invitrogen) and 1% Antibiotic & Antimycotic (ThermoFisher). The media used for BAOEC cells is Dulbecco's Modified Eagle's Medium (DMEM, Life Technology), with 10% heat inactivated fetal bovine serum (FBS, Invitrogen) and 1% Antibiotic & Antimycotic (ThermoFisher). Procine gelatin (0.5%, Sigma-Aldrich) used to facilitate adhesion of BAOEC within devices. CellTracker Orange used to fluorescently label cells (ThermoFisher). Microfluidic molds digitally cut from printable gold foil sheet (Silhouette) with Silhouette SD digital cutter (Silhouette). Microfluidic devices produced from Sylgard 184 polydimethylsiloxane (PDMS) (Dow Corning), Nuclepore polycarbonate semi-permeable membranes with 800nm pore diameter (Whatman), and microscope cover glass slides (FisherBrand). Syringe pump used for nanoparticle flow tests (Harvard Apparatus). Paclitaxel (LC Laboratories, Prod. No: P-9600 Lot: ASM-118) used as anti-cancer therapeutics. Nanoparticles used in work were made from monomethoxy ploy(ethylene glycol)-block-poly(ε-caprolactone) (Sigma Aldrich), Nile red fluorescent dye (Sigma Aldrich), tetrahydrofuran (Sigma Aldrich) and sodium chloride (Sigma Aldrich). All other reagents not mentioned were used directly without purifying.

4.2.2 Microfluidic device fabrication

Microfluidic devices were fabricated using polydimethylsiloxane (PDMS) (SYLGARD 184, Dow Corning) and assembled into a bi-layer device as observed in Fig 4.1. The devices were fabricated using two separate pieces of PDMS with channel molded into them and a polycarbonate semi-permeable membrane (Whatman Cyclopore, Sigma-Aldrich). The semi-permeable membrane is adhered to both pieces of PDMS and sandwiched between the overlapping regions of the channels. The regions where the channels in both pieces of PDMS overlap facilitates transport from one channel into the other through the pores in the semi-permeable membrane. As a result, the pores of the membrane act to dictate the maximum size of materials which can be transferred. In order to only allow for culturing media and small chemical components to pass from one channel to the other while restricting the transport of cells, a membrane with pore size of one micrometer has been chosen. Because cells are not capable of passing through the membrane, a co-culture setup is achievable by growing bovine aortic endothelial cells (BAOECs) on the top surface of the membrane within the apical channel, while human colorectal cancer cells (HCT116s) are grown on the bottom surface of the lower channel termed the basal channel. Additional devices were prepared which consisted of single channels adhered to glass slides. These devices were used for particle distribution and binding studies where a bi-layer setup was not required. Sterilization of the microfluidic devices was carried out by running the fully assembled devices through the autoclave at 134^{0}C for one hour. The choice of PDMS and polycarbonate as materials for the fabrication of the devices was made in order to prevent any cytotoxic effect on the endothelial or cancer cells. Both PDMS and polycarbonate have been shown to have little cytotoxic effect on cells when properly cured and sterilized [194]–[198]. It is for this reason that both materials are often popular choices when fabricating microfluidic system designed to study the cytotoxic effect of other chemical compound and materials, especially in therapeutic delivery applications [194]–[198].

4.2.3 Nanoparticle fabrication

The fabrication process of monomethoxy poly(ethylene glycol)-block-poly(ε-caprolactone) (mPEG-PCL, Mw=1.25 kDa) copolymer nanoparticles with spherical and rod-like shapes was performed as follows. In brief, mPEG-PCL freeze-dried powder (10 mg) and fluorescent dye Nile red were dissolved in 5 mL tetrahydrofuran (THF). Later, 10 mL of deionized water was added dropwise to the mixture with stirring. After the evaporation of the organic solvent, the final solution was transferred to a dialysis bag (MWCO 1000) and submerged in distilled water for 2 days to remove the unloaded dye. Thus, the spherical nanoparticles were obtained. The fabrication process of the rod-like nanoparticles was similar with that mentioned above. The only difference was that the deionized water was replaced by sodium chloride (NaCl) solution. The length of the nanoparticles was changed by varying the concentration of NaCl solution. Similarly to the PDMS and polycarbonate used to produce the microfluidic devices, the mPEG-PCL is also known to be non-cytotoxic. A large body of literature exists supporting the choice of the mPEG-PCL as a safe and non-toxic material from therapeutic delivery via micelles [113], [199]–[201].

4.2.4 Cell growth on device

After fabrication of the microfluidic devices, both the apical and basal channels were filled with a 0.5% porcine gelatin (PG) (0.5%, Sigma-Aldrich) solution and incubated for 30 minutes at 37^0C and 5% CO_2. After incubation, the PG is removed and replaced with BAOEC (Cell Applications, San Diego, CA) suspension in the apical channel and incubated for 12 hours to allow for cell adhesion to the top side of the semi-permeable membrane. After 12 hours, all remaining cell suspension is flown away by establishing media (DMEM(1x) + GlutaMAX – I (gibco, life technologies), 10% HI-FBS (Sigma-Aldrich), 1% Penn/Strep Antibiotic(1X) (gibco, life technologies)) flow within the channel using sterile tubing, syringe and syringe pump (PHD 2000, Harvard Apparatus). The flow rate established within the channel is kept low for purposes of media exchange and aligning the BAOECs to flow. These flow based incubation conditions are held constant typically for 3 to 4 days until the endothelial monolayer on the semi-permeable membrane reaches confluency. Upon achieving a confluent BAOEC monolayer in the apical channel, HCT116s (ATCC, Manassas, VA) are flown into the basal channel and allowed to settle and adhere to the bottom of the basal channel for 24 to 48 hours. HCT116 cells are introduced into the devices in order to permeabilize BAOEC monolayers similar to conditions found in various cancerous disease states. Once the HCT116 cells have properly adhered, a flow rate equivalent to that established in the apical channel is setup in the basal channel using a secondary syringe pump. Both the BAOEC and HCT116 cells are grown within the bi-layer device under these flow conditions within an incubator for the remainder of the experimental proceedings.

4.2.5 Establishing shear rate

The effect of fluid shear on the growth of cells and transport of compounds from channel to channel is established using syringe pumps (PHD 2000, Harvard Apparatus). The syringe pumps allow for control over the flow rates established in both channels of the device. By altering the flow rate within the channels, we are able to specifically set and control the shear rate imparted on the cells growing within each channel and any other materials introduced into the channel along with the flowing media. The equation governing the shear rate established in each of the channels is as follows: $Shear\ Rate = (\frac{6Q}{W*H^2})(1+\frac{H}{W})(f^*)(\frac{H}{W})$, where Q is the established flow rate within the given channel, W is the channel width, H is the channel height, and f^* is a geometrical factor based on channel dimensions which for the microfluidic devices used is 0.7946 [112]. The width and height dimensions for the channels utilized in this study were 500 micrometers and 100 micrometers, respectively. In order to stay within a physiologically relevant range, the shear rate in the apical channel containing the BAOECs was held at 200 sec^{-1} which is at the lower end of range typically experienced within the arterioles of the body [113]–[115]. The shear rate established within the basal channel containing HCT116s was held constant with the shear in the apical channel to prevent any convective flux between channels when not desired. While initially culturing cells within both channels, the shear rate was typically set around 50 sec^{-1} as a means of simply refreshing media exposed to the cells for continued growth while not imparting drastically high shear. It should be noted that equal shear rates were established in both the apical and basal channels in order to prevent the formation of a pressure gradient across the semi-permeable membrane. As a final note, the use of channel dimensions defined above, resulted from several factors which required consideration. Namely, the desire to work within the length scale of smaller human vasculature, ease of endothelial and cancer cell growth, ease of microfluidic device production and long-term device stability factored into the decision of the final channel dimensions. Ideally, producing microfluidic devices on the length scale of less than or equal to 100 micrometers would be more realistic for mimicking human microvasculature

[202]–[204]. However, the production of photoresist features on silicon wafers at such a small size is difficult and is not conducive for several round of PDMS casting to form channels. In order to better facilitate the growth of both endothelial and cancer cells, the use of wider channels was opted for in order to enlarge the total volume of media contained within the channels at any given point in time. This factor is especially important once a confluent monolayer of endothelial cells is formed within the channels and cancer cell seeding is attempted. In order to allow the cancer cells enough time to settle and anchor to the surface of the basal channel, the media flow within the devices must be halted otherwise, the cancer cells would wash away down-stream. This period of static incubation can last anywhere from 12 to 24 hours, during which time, the nutrients contained within the channel are limited. If the channel dimensions are made too small, the amount of media contained within the channels would not be sufficient to sustain both cell types unit normal media flow can be re-established. As a final consideration, larger channel dimensions were chosen in order to help keep the resistance of the overall system low. Use of small channel dimensions would have resulted in a very large resistance to the flow of media established with syringe pumps. Having large resistance in the system leads to increased pressures within the devices which in turn result in leakage and rupturing of the bi-layer microfluidics. In order to avoid such conditions, the use of a wider channel geometry allows for the resistance of the system to be maintained at a reasonable level to allow for the experimental proceedings.

4.2.6 Cell imaging and confluency measurements

Cells grown on devices were imaged utilizing standard fluorescence imaging microscopy (Olympus IX70, Hamamatsu C9300, Plan Fluor 10x & 20x, NA: 0.3, RI: 1). For fluorescence imaging, the plasma membranes of the cultured cells were stained with CellMask^{TM} Orange (2.5µg/mL, Invitrogen) plasma membrane stain to identify the outer most boundaries of the cells occupying the culturing area. This method of cell plasma membrane (PM) staining allows for the quantification of the area specifically covered by cells within the viewing area of the various fluorescence microscopes. Images taken via conventional fluorescence microscopy were utilized to determine the overall cellular monolayer confluency. These measurements were carried out using the FIGI (ImageJ) software suite and the collected image. The imaging technique was used to obtain the average degree of monolayer confluency as well as to quantify the area occupied by gaps between cells [118], [144]. The analysis for the cell coverage measurements were taken once the cells had reached confluency within the apical channel of the device just before HCT116s were introduced into the basal channel. A second measurement of all devices was taken at 72 to 96 hours after introduction of HCT116s into the basal channel. Lastly, final measurements for each device were taken 12, 24, 48, 72, 96, and 120 hours after introduction of anti-cancer therapeutics into the device. Image acquisition software utilized includes HCImage Live (Hamamatsu Photonics) for standard fluorescence imaging and NIS-Elements (Nikon) for acquisition of confocal images.

4.2.7 Anti-cancer therapeutics

In order to study how particle transport is influenced by variations in endothelial monolayer permeability, BAOECs were exposed to HCT116s. Treatment of the microfluidic system with the anti-cancer therapeutic, Paclitaxel, allowed for varying degrees of BAOEC permeability within the diseased state setup. Paclitaxel functioned to eliminate cancer cells and was chosen due to its wide use, high degree of documentation for *in vitro* and *in vivo* data, and relatively inexpensive cost. This anti-cancer therapeutic was introduced into the apical channel of the device in order to mimic an intravenous administration. Any therapeutic introduced into the microfluidic system was subjected to the shear established within the device in order to mimic the situation or blood flow within the body. Therapeutic which successfully transitioned from the apical channel through the semi-permeable membrane into the basal channel were able to act on the HCT116s present. Interaction of the anti-cancer drug with the HCT116s resulted in the death of affected cells, which in turn were washed away downstream and eventually out of the device into the waste media collection containers. As such, the HCT116 cells which were killed off and washed away could no longer contribute to the secretion of permeabilizing agents. Lastly, in order to ensure that the presence of the anti-cancer therapeutic in the apical channel interacting with the BAOECs did not result in the death of healthy BAOEC cells, a high dose of the therapeutic agent was statically incubated with BAOECs prior to the cells reaching confluence in order to determine if the presence of the drug would severely inhibit cell proliferation or cause severe cell death. Chemical authentication and validation data of the Paclitaxel utilized in this work was provided by LC Laboratories (Prod. No: P-9600 Lot: ASM-118).

4.2.8 Particle distribution studies

Particle location within the vessel can influence the likelihood of interaction with the endothelial layer of the vessels. In order to understand how well the particles interact with the vascular wall, their distributions under flow conditions was studied. For these studies, particles of each shape were flown through single layer microfluidic devices at varying shear rates. The shear rates chosen were $200s^{-1}$, $800s^{-1}$, and $1600s^{-1}$, which fall within the physiologically relevant range for humans [113]–[115]. In addition to altering shear, test conditions were run with 25% RBCs (Innovative Research, Inc., single donor human RBCs, type O+) and without RBCs. During each flow, fine resolution confocal scans (Nikon C2plus, Plan Fluor 10x & 20x, NA: 0.3, RI: 1) were captured at various points along the channel. The step size utilized for these scans was 50 nm/step, and each scan was made over the entire cross-section of the microfluidic channel. Image data collected from the confocal microscope was then imported into FIGI (ImageJ) and the fluorescence intensity of each scanned layer was calculated and normalized [144]. Plotting the measured fluorescence intensities and layer data allows for the distribution of each particle shape to be visualized under the specific flow conditions established during the time of each scan. Comparisons could then be made based on changes in particle shape, established shear rate, and blood conditions.

4.2.9 Particle binding studies

The next important step in the therapeutic delivery process is achieving nanoparticle adhesion to the inner wall of the human vasculature. As such the influence of particle shape, blood conditions, and shear rate on particle binding were investigated. All binding studies were conducted under non-specific conditions, as the particles utilized had no antibody coating. Due to the non-specific binding regime utilized, the binding studies were conducted in microfluidic devices which did not contain cells. The absence of cells within the devices also allowed for improved imaging. Each particle was flown through single layer microfluidic devices at varying shear rates as well as varying blood conditions. As noted above, the shear rates utilized were $200s^{-1}$, $800s^{-1}$, and $1600s^{-1}$, and the blood conditions utilized were no RBCs and 25% RBCs. Particle flows were established using a syringe pump for an established period of time. The total number of particles flown in each test were held constant by varying the duration of the flow to shorter and shorter timeframes as the shear rate utilized increased. This was done to ensure normalized testing conditions across all setups. At the completion of each flow, PBS (1X, Sigma-Aldrich) buffer was flown through the channels to wash away any unbound particles prior to confocal imaging. After washing, confocal scans were made across the entire internal surface of each channel to collect fluorescence intensity data. The scans were then loaded into FIGI (ImageJ), and reconstructed back into a bulk 3D image [144]. Final image processing was carried out to determine the fluorescence intensity of particles bound to the inner walls of each channel. Comparisons were then made across varying particle shape, shear rate and blood condition. Finally, for comparative purposes, static binding cases were run, where particle solutions were introduced into the channel and statically incubated for 1 hour prior to rinsing and imaging.

4.2.10 Particle cross-vasculature transport studies

In order to identify the ability of each particle to undergo transport across a semi-permeable membrane, a bi-layer setup for the microfluidic devices was utilized. Particle transport was achieved by flowing particles into the bi-layer channel via syringe pump. In order to quantify, the degree of transport for each test case, the outlets of both the apical and basal channels was collected and measured. The basal outlet contained particles which successfully transported across the semi-permeable membrane, and particles exiting out of the apical outlet were collected and measured to ensure that the total particle concentration introduced into the devices was accounted for at both of the outlets.

The transport studies were carried out under three device conditions as follows, bare devices, devices with only a BAOEC confluent monolayer, and diseased devices containing a monolayer of BAOECs in the apical channel and a monolayer of HCT116s in the basal channel. The second and third device conditions established allowed for studies on the ability of particles to transport under varying degrees of BAOEC permeability.

All transport studies were carried out with flow established in the apical and basal channels. In order to best determine the effect of particle shape on the transport process, all tests were run so that no pressure difference was established across the semi-permeable membrane. The pressures established in both the apical and basal channels for these studies were 632.8, 4832.4, and 17431.2 Pa. Bare device studies did not utilize any cell culturing within the channels prior to introduction of particle suspensions. Devices run with BAOEC confluent monolayers were established 3 to 4 days prior to particle suspension flows to ensure that a highly confluent monolayer was present in the apical channel over the semi-permeable membrane. Lastly, the diseased state devices, were prepared 6 to 8 days in advance of particle suspension flows. 3 to 4 days were spent growing a confluent apical BAOEC monolayer and the remaining days were spent producing a cancer cell monolayer in the basal channel. As with the binding studies, the transport studies were carried out under adjusted timeframes to ensure that the same number of particles were introduced into each devices regardless of the pressure being used. One final note for the diseased state devices, was the later introduction of an anti-cancer therapeutic to influence the cancer cells in the basal channel and the confluency of the BAOEC monolayer in the apical channel. The degree of particle transport was documented throughout a time-course treatment with the Paclitaxel to understand how the BAOEC monolayer integrity influenced the particle transport capabilities.

4.2.11 Statistical analysis

Statistical analysis of all obtained results was run utilizing IBM's SPSS statistical software package (IBM Corp.). All of the figures have significant differences indicated above elements within the plots. One way ANOVA tests were run for each data set with confidence levels of 95% held throughout all plots. All analyses were carried out under conditions of Tukey equal variances assumed, along with tests of homogeneity of variance further verified by both Brown-Forsythe and Welch analyses. Based on the obtained statistical results, all bar graphs contain grouped pairs between groups and within groups indicating statistically significant differences between means indicated by " * ". For all line plots, statistically significant differences in means are compared against the baseline tests for the spherically shaped particles. Significance between both the short rod particle and long rod particle values are indicated by " * ". Significant differences between means for short rod and long rod particles are indicated by " ** ", noting that all differences are given at a confidence level of 95%. Within group F values and degrees of freedom for each plot are noted in their respective legends. Sample sizes for all experimental testing were determined by performing estimation for multiple-sample one-way ANOVA pairwise comparison based on piolet studies utilizing the standard sample size approximation of: $n_{ij} = \frac{2(z\frac{a}{2\tau}+z\beta)^2\sigma^2}{\varepsilon_{ij}^2}$. All statistical comparisons are run under assumptions of equal variance between groups. This assumption is verified via the Levene's Test where all *p values* must be greater than 0.05 in order to verify the equal variance assumption across groups. All data sets presented in this work pass the Levene's Test with *p values* greater than 0.05.

4.3 Results and Discussion

4.3.1 Microfluidic device fabrication

Microfluidic devices were successfully produced using polydimethylsiloxane (PDMS) and polycarbonate semi-permeable membranes assembled into a bi-layer device as observed in Fig 4.1(A) with inlets and outlets for the apical and basal channels. Successful sterilization of the devices via an autoclave allowed for cell culture as represented by the diagram in Fig 4.1(B). The dimensions for the apical and basal channels of the microfluidic devices were 100 μm in height, 100 μm in width, and 25 mm in length.

4.3.2 Characterization of nanoparticle morphology

Three different shapes of polymer nanoparticles were achieved by self-assembly in NaCl-water solution at different concentrations. The morphologies of the particles were measured using transmission electron microscopy (TEM). Solutions without NaCl result in the production of spherical nanoparticles having an average diameter of 45 nm, at 0.05 M NaCl, short rod-like nanoparticles are obtained with an average diameter of ≈ 25 nm and average length of 150 nm and at 0.5 M NaCl, long rod-like nanoparticles are obtained with an average diameter of ≈ 25 nm and an average length of 400 nm, as seen in Fig 4.2. The formation of nanoparticles with varying shapes was accomplished through the introduction of various NaCl concentrations. When the concentration of NaCl was less than 0.05M, the resulting micelles were spherical in shape. When the concentration of NaCl reached 0.05M, the resulting micelles were rod-like in shape (short rod). As the concentration of NaCl was increased, the nanoparticles were observed to elongate. Utilizing a concentration of NaCl equal to 0.1M, the resulting micelles were 600nm in length (long rod) where use of 0.05M resulted in a micelle length of 300nm [205]. In addition, the stability of the nanoparticles has been previous tested and were shown to be stable over the course of 120 hours when subjected to 0.9% physiological saline solution, showing very little degradation [205]. Lastly, in a previous study the nanoparticle micelles were shown to have very good cytocompatability over a range of concentrations from 25 μg/mL to 500 μg/mL for 24 hour incubations [205].

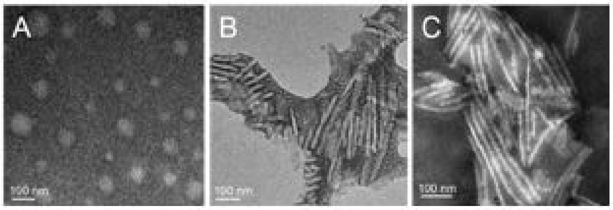

Figure 4.2 The morphology of polymer nanoparticles via TEM scans. (A) Spherical. (B) Short rod-like. (C) Long rod-like.

4.3.3 Cell confluency measurements

Cell confluency was measured utilizing a plasma membrane stain and fluorescence imaging. From these imaging results, FIGI was utilized to calculate the area within the field of view which was occupied by cells and the area occupied by gaps between cells [206]. From the images collected, the degree of cell monolayer coverage, being the area covered by cells expressed as a percentage of the entire viewing area, was determined to be 99.7% when only BAOECs were cultured within the microfluidic devices. However, when HCT116s were introduced and grown in the basal channel in order to alter the BOAEC monolayer permeability, the degree of the BAOEC monolayer confluency dropped to 65.2%. This change in cell area coverage can be seen in Fig 4.3, where conditions with HCT116s show lower BAOEC coverage.

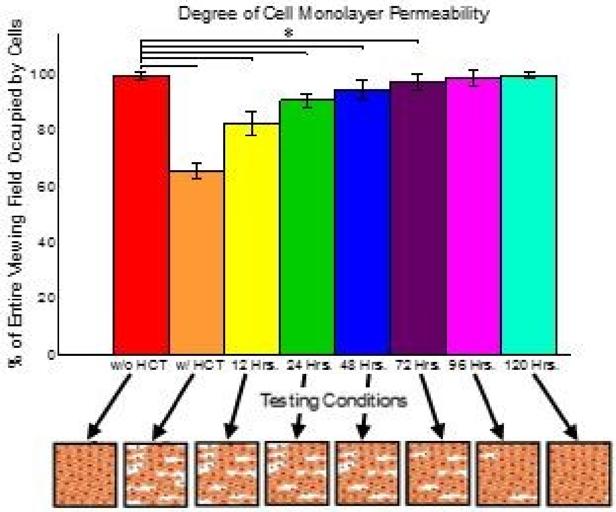

Figure 4.3 Normalized percentage of BAOEC monolayer permeability under various culturing conditions. Data shown as sum of means ± S.D. (n=5 independent microfluidic devices). Percentage of confluent BAOEC monolayer intact without HCT116s, with HCT116s, after treatment with Paclitaxel for 12hrs., after treatment with Paclitaxel for 24hrs., after treatment with Paclitaxel for 48hrs., after treatment with Paclitaxel for 72hrs., after treatment with Paclitaxel for 96hrs., and after treatment with Paclitaxel for 120hrs., measured as a percentage of the entire imaging field, collected via standard fluorescent microscopy. One way ANOVA statistical analysis with Tukey equal variances assumed, along with tests of homogeneity of variance verified by Brown-Forsythe and Welch analyses. $F_{7,32} = 108.86$. Statistical significance indicated by * brackets in both plots at $p \leq 0.05$. Sample collection was carried out from 5 independent devices (biological replicates). All statistical tests have been justified as appropriate.

Subsequent treatment of the permeabilized system with Paclitaxel shows slow recovery back to near confluent BAOEC conditions over the course of 120hrs. Additional data collected for the area of coverage for the gaps between cells agrees well with the measurements taken of the area covered by cells, see Fig 4.4(A). The total area measured independently from the two groups of experiments sum to values near 100%, which would indicate that both methods of data collection resulted in similar results. Representative images of typical results experienced under the various conditions established within the devices can be seen in Fig 4.4(B-I).

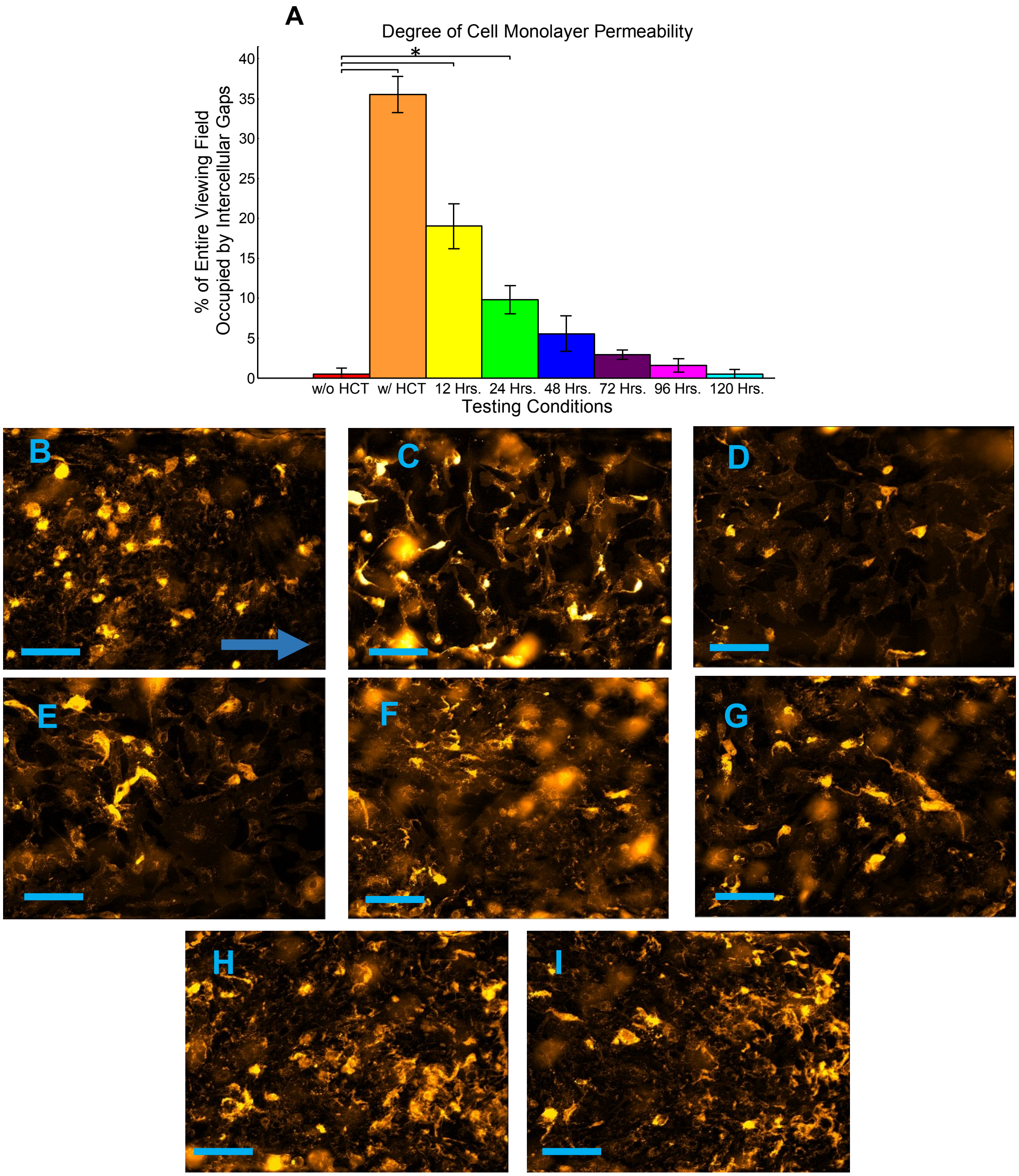

Figure 4.4 Normalized percentage of BAOEC monolayer permeability under various culturing conditions. Data shown as sum of means ± S.D. (n=5 independent microfluidic devices) & representative fluorescence images of BAOEC stained with CellMask^{TM} Orange plasma membrane stain. BAOECs are grown within microfluidic device and subjected to various conditions. (A) Percentage of intercellular gap coverage without HCT116s, with HCT116s, after treatment with Paclitaxel for 12hrs., after treatment with Paclitaxel for 24hrs., after treatment with Paclitaxel for 48hrs., after treatment with Paclitaxel for 72hrs., after treatment with Paclitaxel for 96hrs., and after treatment with Paclitaxel for 120hrs., measured as a percentage of the entire imaging field, collected via

standard fluorescent microscopy. One way ANOVA statistical analysis with Tukey equal variances assumed, along with tests of homogeneity of variance verified by Brown-Forsythe and Welch analyses. $F_{7,32} = 661.92$. Statistical significance indicated by * brackets in both plots at $p \leq 0.05$. Sample collection was carried out from 5 independent devices (biological replicates). All statistical tests have been justified as appropriate. (B) BAOECs grown in confluent monolayer. (C) BAOEC monolayer after exposure to HCT116s present in basal channel. (D) BAOEC monolayer after treatment of HCT116s with Paclitaxel for 12 hrs. (E) BAOEC monolayer after treatment of HCT116s with Paclitaxel for 24 hrs. (F) BAOEC monolayer after treatment of HCT116s with Paclitaxel for 48 hrs. (G) BAOEC monolayer after treatment of HCT116s with Paclitaxel for 72 hrs. (H) BAOEC monolayer after treatment of HCT116s with Paclitaxel for 96 hrs. (I) BAOEC monolayer after treatment of HCT116s with Paclitaxel for 120 hrs. All scale bars are 50μm in length and direction of flow in all images is represented by blue arrow.

4.3.4 Particle distribution

In order to better understand where particles tend to concentrate in bulk fluid flow, and the effect which particle shape has on these zones of concentrated particles, confocal based scans were run on the spherical, short rod, and long rod particles. A representative confocal 3D reconstruction is presented in Fig 4.5(A). From the confocal scans, the following data was observed for a range of shear rates and blood conditions within the devices. The flow condition which resulted in a peak closest to the channel wall was the long rod particles flown at a shear of 1600 sec^{-1} with the presence of 25% RBCs in suspension. The conditions resulting in the furthest peak from the channel wall was the spherical particles flown at a shear rate of 800 sec^{-1} without RBCs.

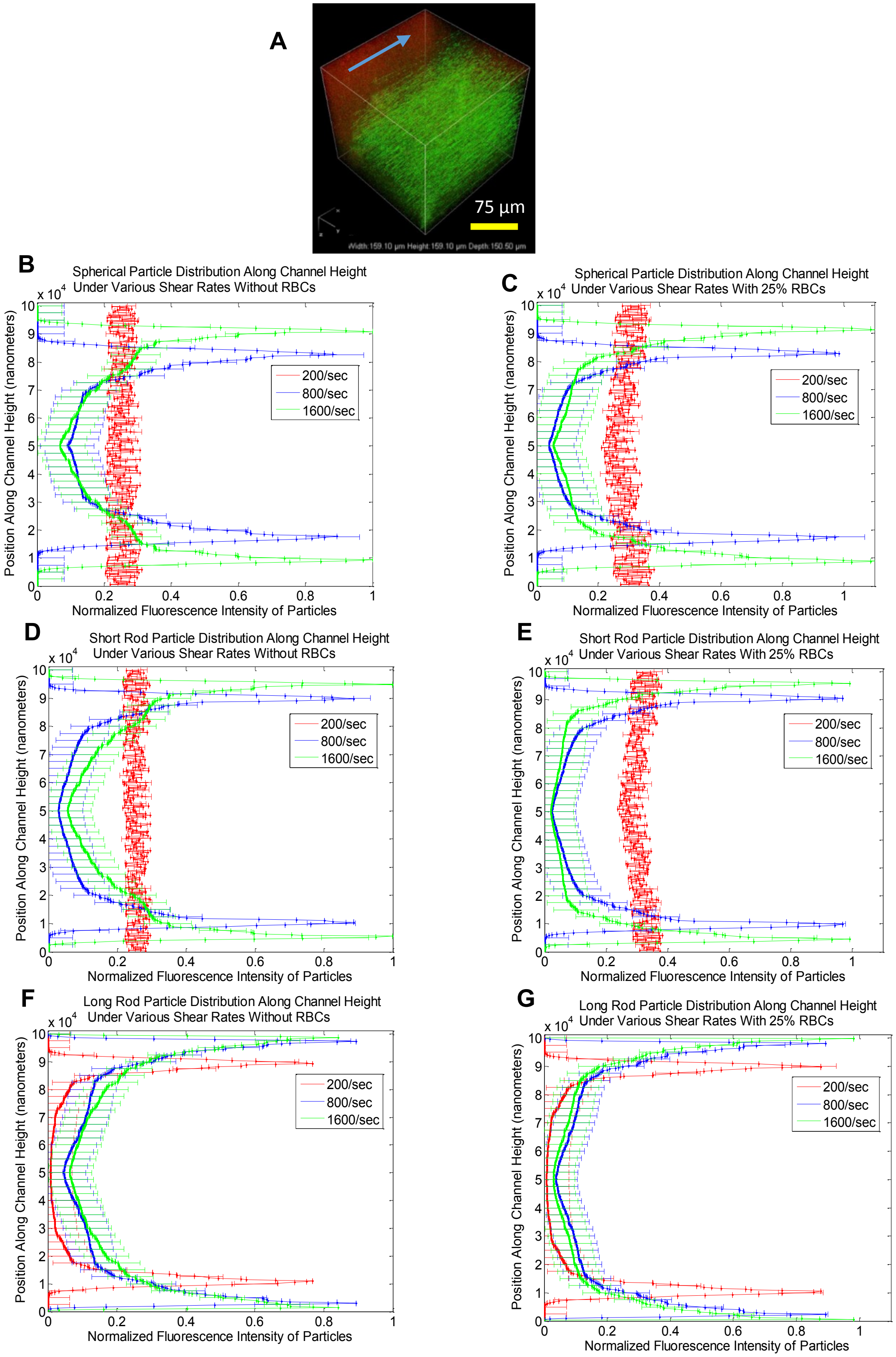
A
75 µm
Width: 159.10 µm Height: 159.10 µm Depth: 150.50 µm
B
Spherical Particle Distribution Along Channel Height
Under Various Shear Rates Without RBCs
C
Spherical Particle Distribution Along Channel Height
Under Various Shear Rates With 25% RBCs
D
Short Rod Particle Distribution Along Channel Height
Under Various Shear Rates Without RBCs
E
Short Rod Particle Distribution Along Channel Height
Under Various Shear Rates With 25% RBCs
F
Long Rod Particle Distribution Along Channel Height
Under Various Shear Rates Without RBCs
G
Long Rod Particle Distribution Along Channel Height
Under Various Shear Rates With 25% RBCs
x 10^4
Position Along Channel Height (nanometers)
Normalized Fluorescence Intensity of Particles
200/sec
800/sec
1600/sec
0
1
2
3
4
5
6
7
8
9
10
0
0.2
0.4
0.6
0.8
1

Figure 4.5 Representative image collected during particle flow tests & normalized particle concentration distributions under various shear rates and blood conditions. Data shown as sum of means ± S.D. (n=5 independent microfluidic devices). (A) 3-Dimensional particle distribution confocal scan depicting traces of particle paths during flow and particle locations. Scale bar is 75μm and blue arrow indicates direction of flow. (B) Spherical distribution at various shear without RBCs. (C) Spherical distribution at various shear with 25% RBCs. (D) Short Rod distribution at various shear without RBCs. (E) Short Rod distribution at various shear with 25% RBCs. (F) Long Rod distribution at various shear without RBCs. (G) Long Rod distribution at various shear with 25% RBCs.

General trends observed in the data show that increases in shear rate, larger particle sizes, and conditions with 25% RBCs in suspension lead to concentration peaks closer to the channel walls. Conditions using the two smaller particle shapes run at 200 sec^{-1} resulted in uniform distribution without any concentration peaks. Fig 4.6(A) depicts an example plot of the fluorescence intensity distribution of the spherical particles without RRBCs under various shear rates. From the figure, peak positions can be observed where the spherical particle concentration is greatest through the cross-section of the channel as flow occurs. Figure 4b depicts the maximum concentration peak position distance from the wall of the channel for all of the conditions tested. Fig 4.5(B-G) depicts the confocal fluorescence intensities of each particle shape throughout the depth of the 100 μm channel under various testing conditions.

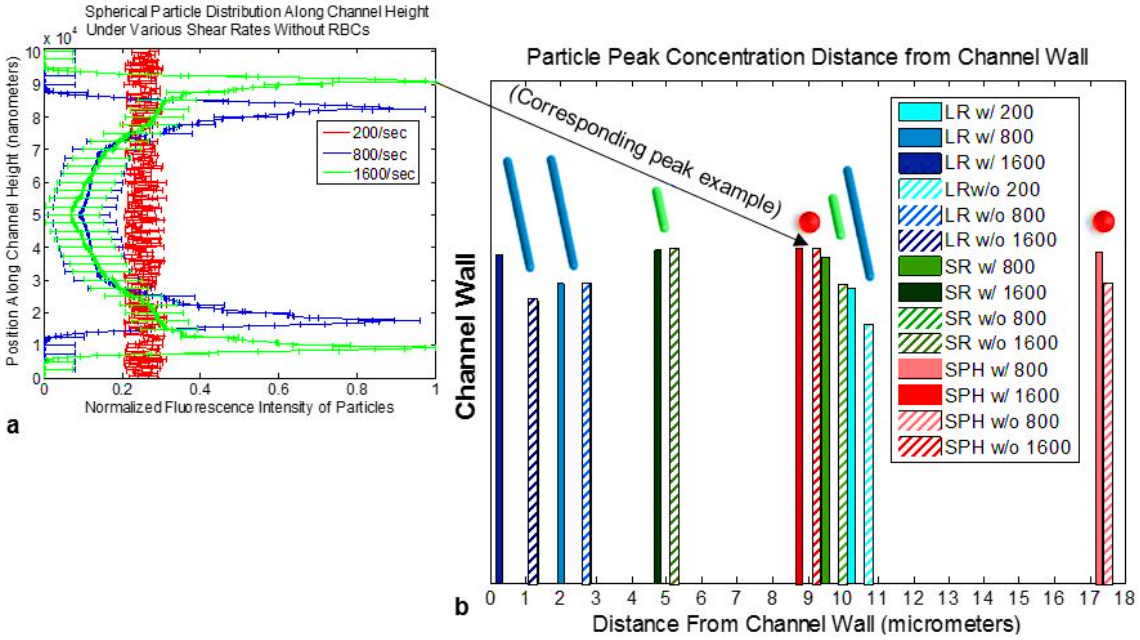

Figure 4.6 Particle concentration peak positions under various flow conditions. Data shown as sum of means ± S.D. (n=5 independent microfluidic devices). (A) Example spherical particle fluorescence intensity distribution along channel cross-section measured via confocal microscope without RBCs under various shear rates. (B) Particle concentration peak position distances from the channel wall plotted for all particle shapes, blood conditions, and shear rates tested.

4.3.5 Particle binding

Fluorescence intensities of bound particles within the channels were collected via confocal microscopy. The initial scans show the greatest degree of binding for the spherical particles, followed by the short rod and long rod particles, respectively. The initial scans can be seen in Fig 4.7(A) and Fig 4.7(B), where increases in shear rate lead to lower levels of particle binding and the presence of RBCs increases the observed binding. However, it should be noted that the initial data do not reflect the differing volumes of each particle shape.

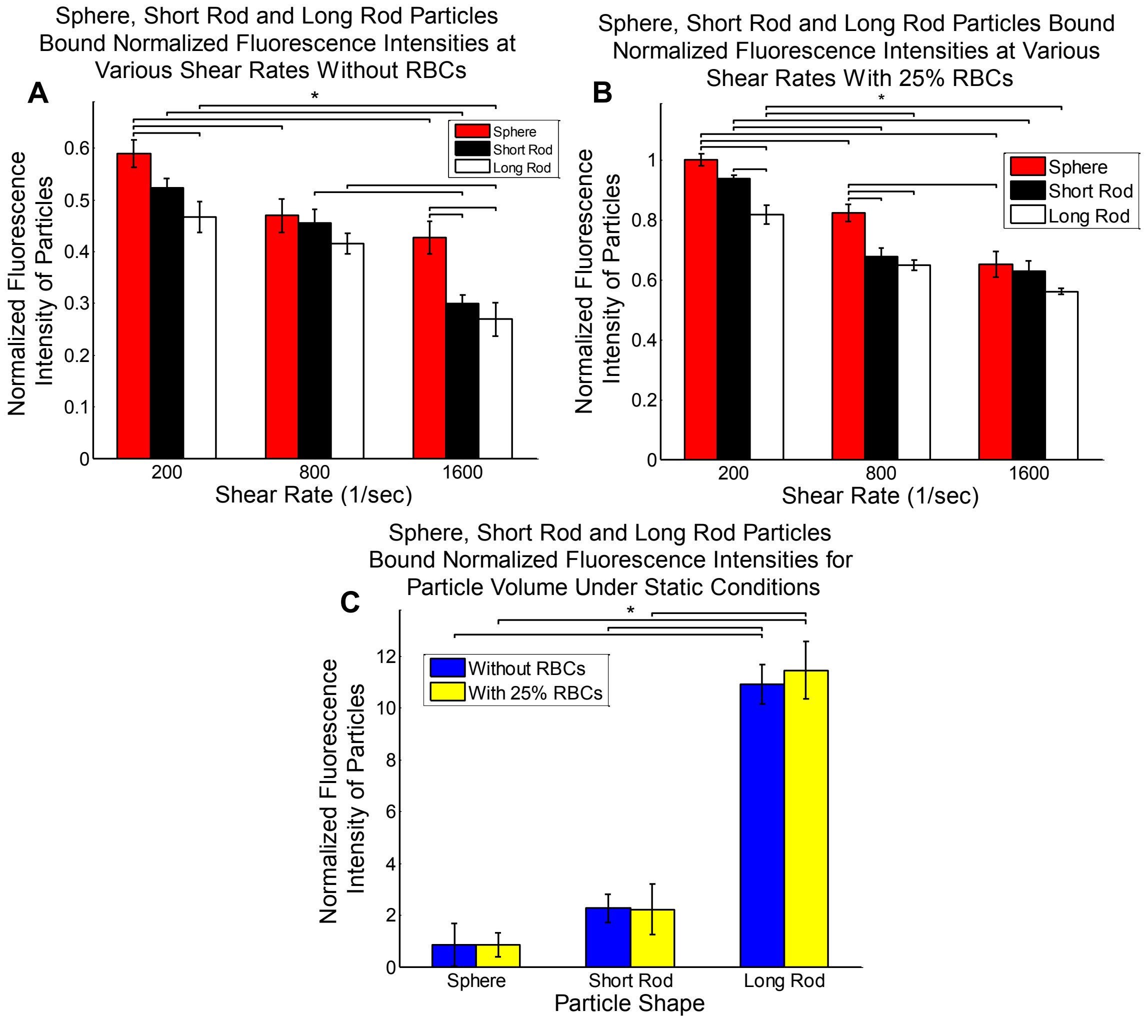

Figure 4.7 Normalized bound particle fluorescence intensities under various shear rates, blood conditions & particle volume considerations. All data shown as sum of means ± S.D. (n=5 independent microfluidic devices). (A) Spherical, short rod, and long rod intensities at various shear without RBCs. $F_{8,18} = 27.59$. (B) Spherical, short rod, and long rod intensities at various shear with 25% RBCs. Data not normalized for particle volume. $F_{8,18} = 50.16$. (C) Spherical, short rod and long rod intensities under static conditions with data normalized for particle volume. One way ANOVA statistical analysis with Tukey equal variances assumed, along with tests of homogeneity of variance verified by Brown-Forsythe and Welch analyses. $F_{5,12} = 246.58$. Statistical significance indicated by * bracket at $p \leq 0.05$ for all plots. Sample collection was carried out from 5 independent devices (biological replicates). All statistical tests have been justified as appropriate.

Once normalized for particle volume, the degree of binding shows that the long rod particles are able to bind the greatest amount of therapeutic to the walls of the mimicked vessel, as seen in Fig 4.8(A) and Fig 4.8(B) for conditions with and without RBCs. The short rod and spherical particles had lower degrees of binding after particle volume normalization, respectively. The same trends were observed after normalization for decreases in binding as shear rate increases, and increases in binding with the presence of RBCs. As a final comparison, the particle binding observed under static conditions showed that the presence of RBCs made no difference in the degree of binding. Overall, the degree of static binding was substantially larger when compared to the flow based conditions and the long rod particles were determined to be able to bind the greatest amount of therapeutic after particle volume normalization. See Fig 4.7(C) for static binding data normalized for particle volume.

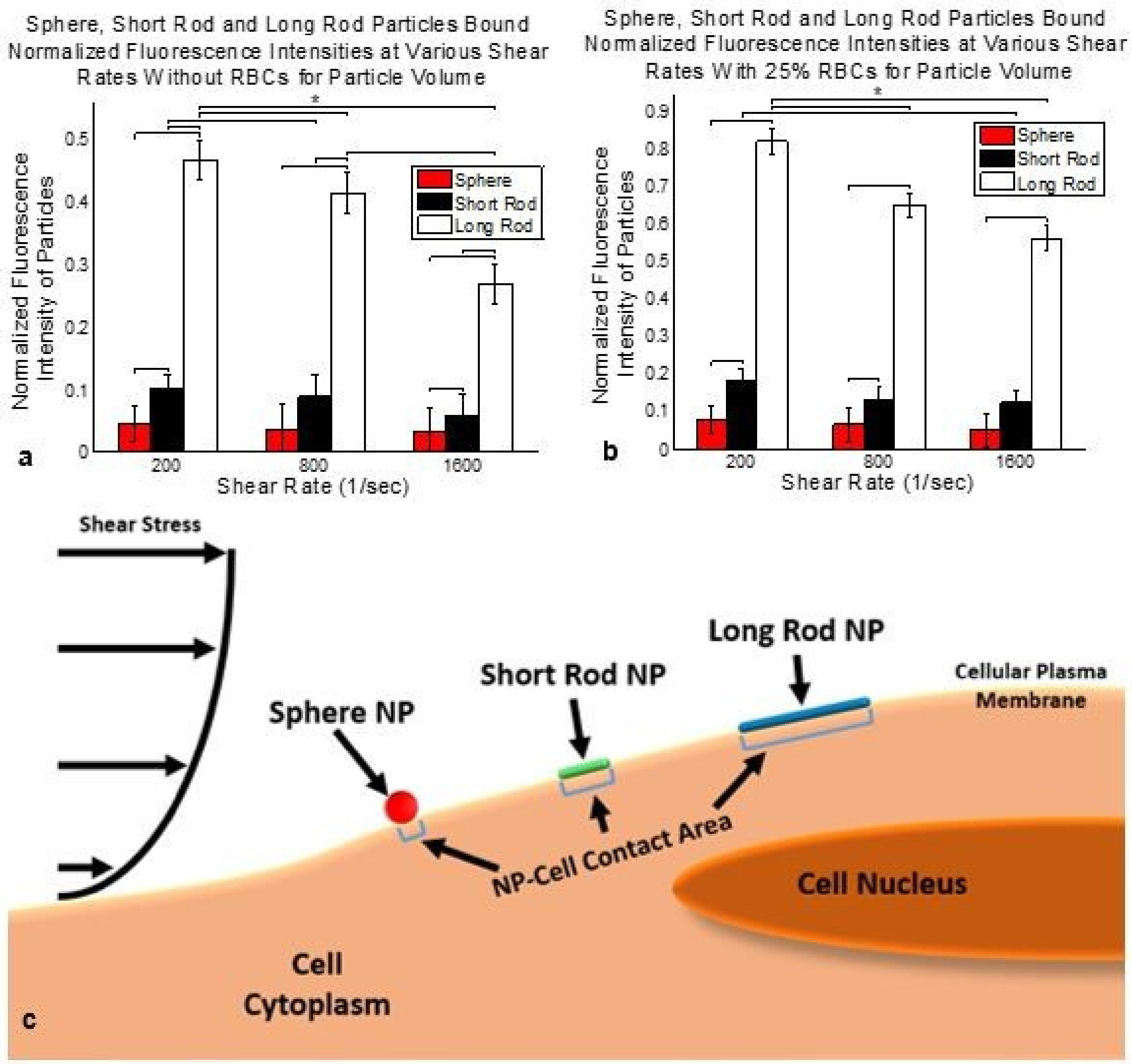

Figure 4.8 Normalized bound particle fluorescence intensities under various shear rates, blood conditions & particle volume considerations coupled with schema. All data shown as sum of means ± S.D. (n=5 independent microfluidic devices). (A) Normalized bound particle fluorescence intensities at various shear rates without RBCs. Data normalized for particle volume. $F_{8,27} = 298.32$. (B) Normalized bound particle fluorescence intensities at various shear rates with 25% RBCs. $F_{8,27} = 69.31$. Data normalized for particle volume. One way ANOVA statistical analysis with Tukey equal variances assumed, along with tests of homogeneity of variance verified by Brown-Forsythe and Welch analyses. Statistical significance indicated by * brackets in both plots at $p \leq 0.05$. Sample collection was carried out from 5 independent devices (biological replicates). All statistical tests have been justified as appropriate. (C) Particle binding schema indicating larger contact area for long rod and short rod nanoparticles along with a larger magnitude shear stress placed on sphere nanoparticle.

After normalization for particle volume, the ideal nanoparticle shape for the binding of therapeutics to the inner wall of a vessel would be the long rod particles flown under conditions with RBCs at the lowest shear rate as seen in Fig 4.8. Fig 4.8(C) depicts a schema of the differences in binding area and shear stress exposure for the three different nanoparticles tested. These differences depicted in Fig 4.8(C) influence the overall nanoparticle binding observed which is considered later in the conclusion for this section.

4.3.6 Particle cross-vascular transport

We turn to the final phase of therapeutic delivery which is the transport of particles from within the vasculature out into diseased tissues. As mentioned previously, a bi-layer microfluidic setup was utilized to facilitate particle transport with all tests being carried out under conditions without RBCs and equal pressures across the membrane. Fig 4.9(A) depicts the particle diffusion process from the apical channel into the basal channel which results in a particle concentration gradient. The data presented in this section have been normalized for particle volume in order to determine the ideal particle shape for therapeutic delivery. Fig 4.9(B) through Fig 4.9(D) depict the therapeutic transport achieved based on the condition established in the devices. Under bare channel and diseased channel conditions, the long rod particles were capable of achieving the greatest amount of therapeutic transport for all equal pressure cases tested. The short rods showed the greatest therapeutic delivery under healthy BAOEC monolayer conditions at the two lower equal pressure cases tested and the spherical particles showed improved delivery at the greatest equal pressure case under healthy conditions. Reduction in therapeutic delivery with increased equal pressures during testing was observed for all device setups tested as seen in Fig 4.9(B-D).

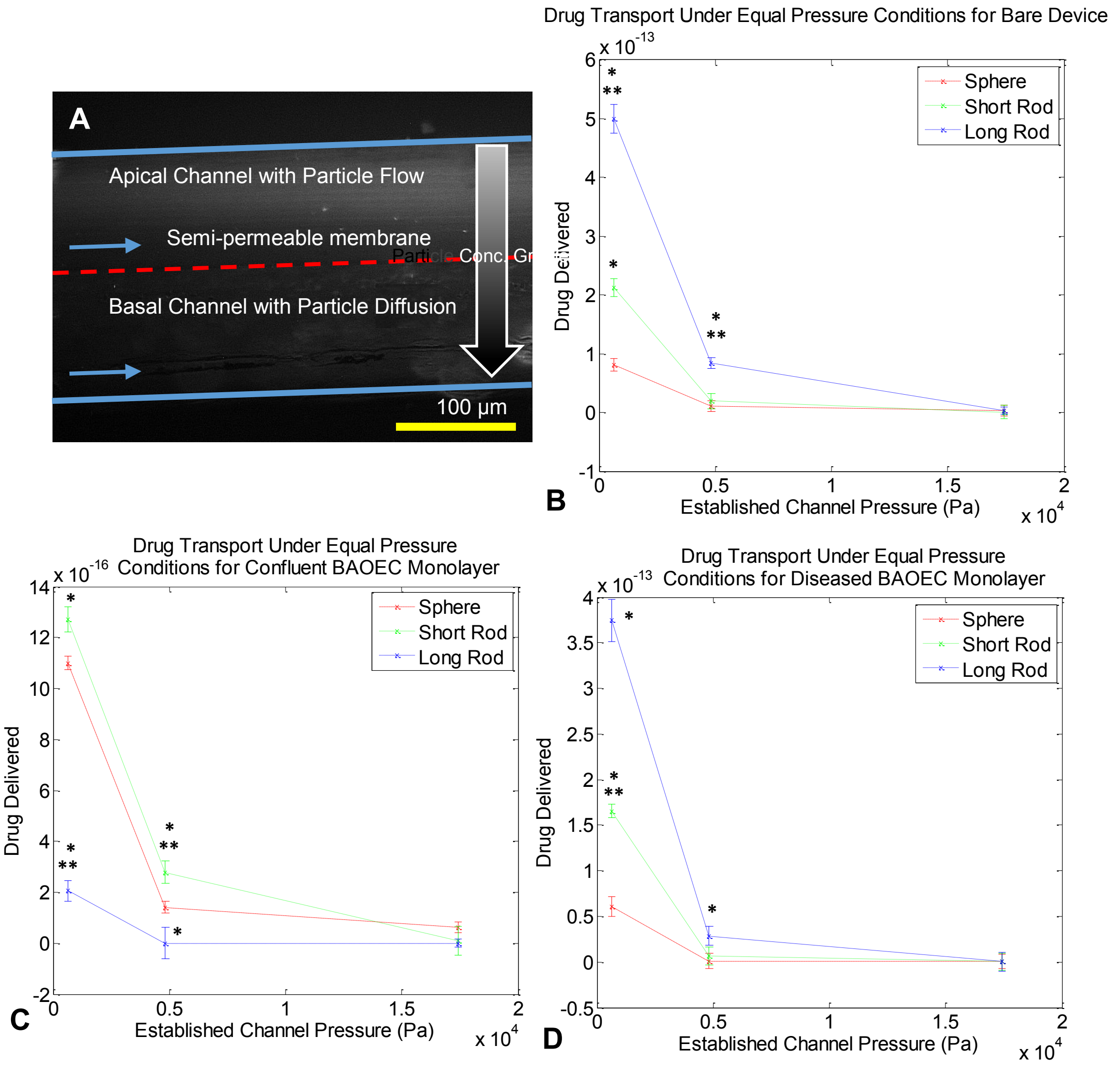

Figure 4.9 Cross-sectional fluorescence image of particles flowing through bi-layer microfluidic device & normalized drug transport for various particle shapes and device conditions. Data shown as sum of means ± S.D. (n=5 independent microfluidic devices). (A) Particle diffusion is observed from the apical into the basal channel via gradient of particle concentrations, indicated by image brightness. Scale bar is 100 μm, blue arrows indicate flow directions in both apical and basal channels, and red dashed line indicates where the semi-permeable membrane is located in the cross-sectional view. (B) Normalized drug transport for particle shapes at various pressures in bare microfluidic devices. $F_{8,18}$ = 413.70. (C) Normalized drug transport for particle shapes at various pressures in microfluidic devices containing confluent BAOEC monolayers. $F_{8,18}$ = 632.71. (D) Normalized drug transport for particle shapes at various pressures in diseased state microfluidic devices with apical BAOECs and basal HCT116s. $F_{8,18}$ = 5535.61. All data normalized for particle volumes. One way ANOVA statistical analysis with Tukey equal variances assumed, along with tests of homogeneity of variance verified by Brown-Forsythe and Welch analyses. Statistical significance between short rod/long rod and sphere (control) indicated by * at $p \leq 0.05$ & statistical significance between short rod and

long rod indicated by ** at $p \leq 0.05$. Sample collection was carried out from 5 independent devices (biological replicates). All statistical tests have been justified as appropriate.

Taking the diseased state model one step further, the addition of Paclitaxel to the disease state showed recovery in the BAOEC monolayer. The constant perfusion of Paclitaxel along with the particles was carried out over the course of 5 days as particle transport was monitored as seen in Fig 4.10. At 12 hours of treatment, the amount of particle transport began to drop slightly as the HCT116s began to die off and the BAOECs began to recover their confluency. After 24 hours, transport continued to drop, with a shift at 4832.4 Pa where the short rods began to perform noticeably better than the long rods and spherical particles. After 48 hours, transport of all three particle shapes continued to drop, with a very marked drop in long rod transport at 632.8 Pa. Also at 48 hours of treatment, the short rods perform the best at 4832.4 Pa. At 72 hours, the long rod transport dropped even further performing worse than the short rods at 632.8 Pa and worse than both of the other particles at 4832.4 Pa and 17431.2 Pa. After 96 hours of treatment, the transport data begins to resemble the trends observed in the BAOEC confluent devices. The short rods perform the best at the two lower pressures and the spherical particles begin to show improved performance at the highest pressure. The long rods across all pressures perform the worst after 96 hours of treatment as the pores in the BAOEC monolayer begin to drastically reduce in size and frequency. Finally, after 120 hours of treatment, the transport data is indistinguishable from the data and trend observed for devices only containing confluent monolayer of BAOECs. The time-course of particle transport during the Paclitaxel treatment can be observed in Fig 4.10 at the three equal pressure cases tested. Breakdowns of each time interval throughout the whole time-course can be seen in Fig 4.11.

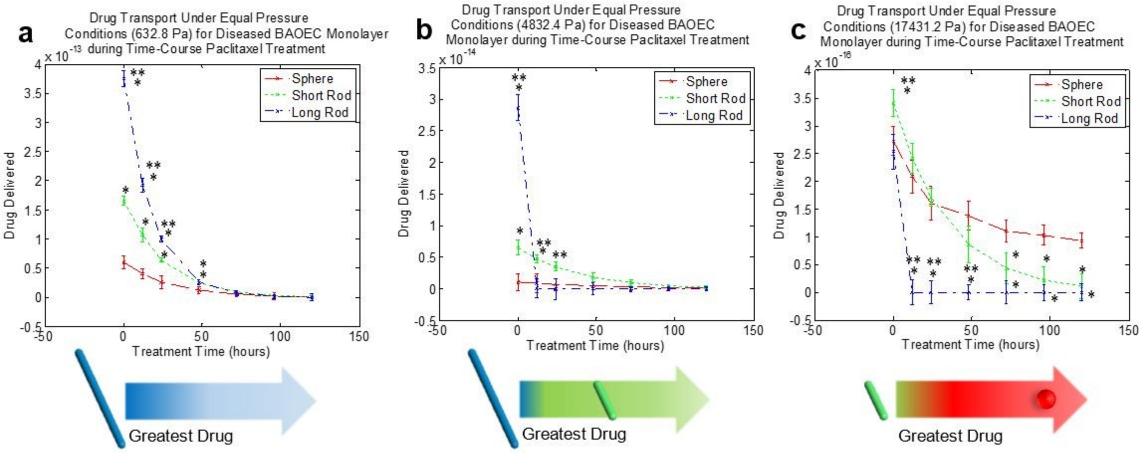

Figure 4.10 Normalized time-course plots of drug transport for various particle shapes and pressures during Paclitaxel treatment. Data shown as sum of means ± S.D. (n=5 independent microfluidic devices). (A) Normalized time-course drug transport for particle shapes over 120hrs. at 632.8Pa. $F_{20,42} = 2479376.58$. (B) Normalized time-course drug transport for particle shapes over 120hrs. at 4832.4Pa. $F_{20,42} = 114.79$. (C) Normalized time-course drug transport for particle shapes over 120hrs. at 17431.2Pa. $F_{20,42} = 1.60$. One way ANOVA statistical analysis with Tukey equal variances assumed, along with tests of homogeneity of variance verified by Brown-Forsythe and Welch analyses. Statistical significance between short rod/long rod and sphere (control) indicated by * at $p \leq 0.05$ & statistical significance between short rod and long rod indicated by ** at $p \leq 0.05$. Sample collection was carried out from 5 independent devices (biological replicates). All statistical tests have been justified as appropriate. Diagrams in (A-C) indicate the nanoparticle shape for maximum drug delivery across endothelial monolayer to diseased site.

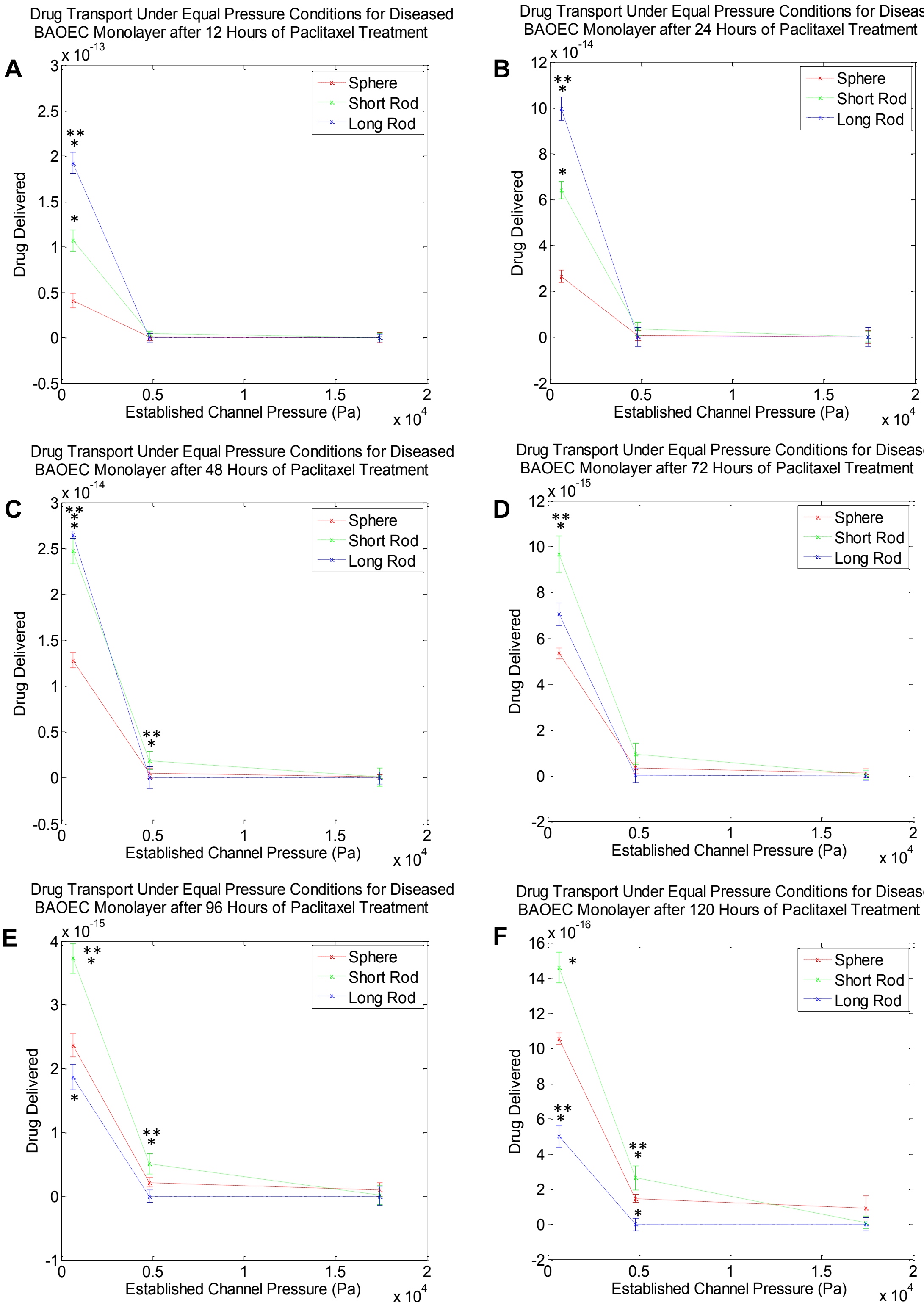

Figure 4.11 Normalized drug transport for various particle shapes and pressures during Paclitaxel treatment time-course. Data shown as sum of means ± S.D. (n=5 independent microfluidic devices). (A) Normalized drug transport for particle shapes 12hrs. into

treatment. $F_{8,18} = 276.10$. (B) Normalized drug transport for particle shapes 24hrs. into treatment. $F_{8,18} = 1054.86$. (C) Normalized drug transport for particle shapes 48hrs. into treatment. $F_{8,18} = 2998.76$. (D) Normalized drug transport for particle shapes 72hrs. into treatment. $F_{8,18} = 84.36$. (E) Normalized drug transport for particle shapes 96hrs. into treatment. $F_{8,18} = 572.99$. (F) Normalized drug transport for particle shapes 120hrs. into treatment. $F_{8,18} = 494.04$. All data normalized for particle volumes. One way ANOVA statistical analysis with Tukey equal variances assumed, along with tests of homogeneity of variance verified by Brown-Forsythe and Welch analyses. Statistical significance between short rod/long rod and sphere (control) indicated by * at $p \leq 0.05$ & statistical significance between short rod and long rod indicated by ** at $p \leq 0.05$. Sample collection was carried out from 5 independent devices (biological replicates). All statistical tests have been justified as appropriate.

4.4 Conclusions

The goal of this study was to provide insight into improving therapeutic delivery performance through the application of variously shaped particles.

Enhanced conditions for distributing particles nearest to channel walls were achieved by using long rods with 25% RBCs at the shear rate of 1600 s^{-1}. These results were observed because the long rods have larger surface area exposure to the inertial lift force pushing towards the walls and a drag force pushing towards the channel core [206]–[208]. The distribution peaks follow the trends outlined by the theory of hydrodynamic lift and drag as predicted by the lift Equation 1 from Takemura & Magnaudet:

$$\boldsymbol{C_L = (8.94\beta^2(LRe)^{-2.09})\left(\left(1 + \left(0.6Re^{\frac{1}{2}}\right) - \left(0.55Re^{0.08}\right)\right)^2\right)\left(\left(\frac{L}{1.5}\right)^{-2\tanh(0.01Re)}\right)}$$

(1)

along with the hydrodynamic drag Equation 2 from Vasseur & Cox:

$$\boldsymbol{C_D = \frac{27}{4LRe} + \frac{24}{Re\left(1+\left(\frac{3}{8}\right)Re\right)}} \qquad \textbf{(2)}$$

where C_L is hydrodynamic lift, C_D is hydrodynamic drag, β is a coefficient (0.50698 for this study), L is the distance away from the channel wall, and Re is the particle Reynolds number [206]–[210]. Beyond particle distribution, the long rod particles were shown to undergo improved binding to the channel walls.

The binding section indicates that the best performer is the long rods at the lowest shear rate tested of $200s^{-1}$ with 25% RBCs. The large volume of the long rod significantly outperforms the other shapes because adhesion of a single long rod is equivalent to more than 2 short rods and more than 4 spherical particles. Therefore the long rod particles are best at binding therapeutic to the vessel lumen because of the large surface area over which non-specific binding can occur. Additionally, long rods and short rods have less area exposed to shear flow within the channel reducing drag. These factors result in greater particle binding for the long rods as depicted in the schema of Fig 4.8(C).

Lastly, the transport portion of this study showed that short rods and spherical particles performed best due to their smaller size and small gaps in the EC monolayer for healthy vessels. Diseased conditions showed improved performance with long rods due to large gaps in the EC monolayer. However, treatment with Paclitaxel resulted in changes in transport as the BAOEC monolayers regained confluency as in Fig 4.3 with schema. The long rods performed best under low pressures throughout the treatment time-course because the particles had longer to undergo diffusion transport. However under medium pressure initial treatment with long rods followed by short rods after 12 hours performed best due to shorter particle diffusion times and reduced EC permeability as therapeutic treatment progressed. Lastly, treatment under high pressures were best for short rods followed by spherical particles after 24 hours due to the very brief diffusion timeframe and reduction in EC permeability with Paclitaxel treatment. In addition, the improved performance of the smaller particle shapes at the higher pressures can be attributed to the improved particle focusing towards the channel walls. In order for the particles to transport across the EC monolayer, they must first be near the edges of the channel and cell monolayer. At the lowest pressure, the sphere and short rod particles remain uniformly distributed throughout the channels cross-section and as such have a longer distance to diffuse in order to cross the EC monolayer. Under the same low-pressure condition, the long rod particles are large enough to be influenced by the hydrodynamic lift force allowing the particles to be more heavily distributed closer to the channel walls and in turn have a shorter distance to diffuse in order to cross over the EC monolayer. As the pressure is increased, the smaller particles are focused in higher concentrations closer to the channel wall, in turn reducing the distance for the particles to diffuse across the cell monolayer. This improved particle focusing closer to the channel wall coupled with the increased diffusion achieved by the two smaller particle shapes, allows the sphere and short rod particles to begin to outperform the long rod particle at the higher pressures tested. The low pressure conclusions agree well with *in vivo* mice tumor studies by Zhou and colleagues (2012), with the long rods delivering the greatest amount of drug under pressures near the lower end of the range tested in this work [211].

One final consideration given to the process of therapeutic delivery via nanoparticle carries is the biodistribution of the carriers *in vivo* and the circulation times associated with various particle sizes and shapes. It is well documented in literature that smaller particles tend to be more readily absorbed by the tissue of organs such as the liver, lungs and spleen. In general, these three particular organs tend to have the greatest accumulation of nanoparticles, either due to filtration functions within the body or large surface area for material absorption and exchange [185], [192], [193], [212]. When compared to the results obtained from our blood vessel model we found that our conclusions were in good agreement with the trend observed *in vivo*. The spherical particles tended to most easily transport from the mimicked vessel over to the surrounding tissue. Likewise, it is well accepted in literature that larger particles or particles with larger aspect ratios, such as long filaments, tend to have longer circulation times *in vivo* [185], [192], [193], [212]. The longer circulation lifetime of larger particles results from lower rates of binding with vascular walls and being taken up by surrounding tissue less easily due to their size [185], [192], [193], [212]. Again these trends were observed in our model system, where the long rod particles bound in the lowest quantity to the walls of the mimicked vessel, however, due to their larger therapeutic carrying capacity were able to outperform the smaller particles when considering the characteristic of drug delivery.

Overall, the long rod filamentous nanoparticles have presented as the best option for the delivery of therapeutics from the three shapes studied in this work. The biomimetic nature of the long rods leverages the same effect observed in vesicle, virion, and DNA transport/translocation to efficiently deliver large payloads in as few packages as possible [190], [191], [213]–[216]. Improving disease treatment also relies on the pressure or flow rate in the general zone of the disease, as well as the time-course over which treatment is administered. The best option for patients may not be as simple as picking a single particle shape and treating over the entire duration of the disease. Instead, consideration may be given to trying an initial combination of particle shapes, or changing particle shapes throughout treatment time-courses. As a final improvement to the therapeutic screening system, a method for producing 3D tumor spheroids is required in order to achieve a higher level of physiological relevance and to improve the predictive capabilities of the system as a whole. Therefore, the next chapter introduces a bi-layer microfluidic device and accompanying method designed to produce tumor spheroids in an expedited manner using nutrient flow for use in therapeutic screening. In addition, a computational model is developed to predict the growth of the tumor spheroids under flow conditions.

Chapter 5: Bi-layer microfluidic platform for expedited tumor growth towards drug evaluation

5.1 Introduction

Throughout the world 14.1 million people suffer from cancers of various types as of 2012, with an estimated increase to around 21.3 million by 2030 [1]–[3]. The average survival rate after diagnosis varies based on cancer type and the stage at which the cancer is identified [2], [3]. Improving the likelihood of patient survival requires early diagnosis along with rapid development and implementation of treatment plans [2], [3].

Current *in vitro* growth of cancer models and therapeutic performance tests are run using two-dimensional monolayers or sheet cultures of cancer cells [217], [218]. While this approach reduces the time required to identify a viable candidate, it makes use of a model system which does not match what is experienced *in vivo* [217]–[222]. As such this method can result in the selection of a therapeutic treatment plan which is not ideal for use against the patient's tumor mass due to misrepresentation of cell-cell interactions and differences in drug kinetics between 2D and 3D models [217]–[222]. In order to better identify viable therapeutic treatment options for patients a need exists for methods capable of generating three-dimensional tumor spheroids or masses in a short period of time [217]–[222]. Current *in vitro* approaches such as liquid-overlay [223], hanging-drop [224], magnetic levitation [225], bioreactors [226] and others are capable of producing tumor spheroids however suffer from issues of low spheroid quantities, inability to refresh culture media, difficulty with direct tumor imaging, difficulty with introduction of therapeutics for drug testing, high cost, large initial quantities of cancer cells required for growth and long periods of time as indicated in Table 5.1 [227]–[233]. Ideally, such *in vitro* growth systems should be capable of generating tumor models without such issues for testing [223]–[226], [234]. In addition, the tumor models should be produced quickly in order to reach an exponential growth phase, where treatment of *in vivo* tumors typically occurs [217], [218].

Table 5.1 Advantages and improvements over existing methods. Comparison of our microfluidic growth platform with traditional cancer growth techniques and platforms.

	Imaging	Throughput	Media Circulation	Control over Drug Testing	Cost	Initial Number of Cells Required	Culturing Time Required
Hanging-Drop	Hard	Low	No	None	Low	Low	Long
Animal Models	Very Hard	Low	Yes	Low	High	High	Long
NASA Bioreactor	Hard	High	Yes	Low	High	High	Long
Our Bilayer Microfluidic	Easy	High	Yes	High	Low	Low	Short

Current 3D growth models require 1 week to 1 month in order to fully establish cancer spheroids before any drug screening can occur [217], [235]. Additionally, several hundreds to thousands of initial cancer cells are often required in order to form such 3D tumor models [227]–[233]. As an example, *in vivo* injection of cancer cells into animal models such as mice and rats often requires large populations ($1X10^5$ or more) of cancer cells for injection and can typically require a several weeks or more of growth before treatment testing can begin [236]–[238]. The acquisition of such a large population of cells from patient samples can often be difficult due to the rarity of cells in certain cancer types where fewer than 50 cells may be collected in biopsies [227]–[233]. Following the establishment of the tumor models, simultaneous therapeutic analysis is required in order to identify and viable therapeutic treatments [227]–[233]. As such, being able to perform tumor growth to a predetermined size in an expedited manner within a platform capable of facilitating tests with dozens of potential therapeutic options will aid to shorten the drug screening process [227]–[233]. However, performing multiple drug tests simultaneously increases the time required for data acquisition and analysis.

The overall pool of potential therapeutics capable of being utilized as treatment options continues to grow as new drugs are approved by the FDA. From the year 2013 to February of 2018, a total of nearly 160 new drugs for treatment of various cancers has been approved and released on the market [239]. For some specific cancers, such as leukemia, there exist multiple drug choices which could potentially serve as the best treatment option for patients, with *BCR-ABLI* T315I-positive cell leukemia alone having 11 potential options [240]. More substantial are the number of drug candidates which are made available to patients in clinical trials, where it is not uncommon to have upwards of 50 or more candidates available [228]. Such clinical trials typically pose more risk to patients as a full response profile has not been completely established and could serve to be a waste of patient's time if the chosen treatment is not effective [228]. Current practices typically utilize trial dosages on patients to test drug candidate responses until an effective drug is found, which a time-consuming and painful process [241]–[243]. Such large quantities of potential therapeutic options is promising for patients, however, identifying which is best suited can serve to be an insurmountable challenge [228]–[233]. In order to better sample a larger range of the total available clinical trial and marketed drug options, a system must be developed which is capable of running tens to hundreds of potential options simultaneously in order to facilitate the timely selection of a viable treatment [244], [245].

Previous microfluidic platforms have been developed to help address the issues faced in cancer therapeutic testing [246]–[248]. All of these systems involve the production of devices which have specialty chambers in which cancer cells can be grown and exposed to therapeutic agents [246]–[248]. However, most of the systems designed to handle three dimensional tumor spheroids require that the spheroids be pre-formed outside of the device and later introduced upon reaching a suitable size or that the spheroids be grown slowly within the device [246]–[250]. In both cases, the time required to produce the tumor spheroids is long, large initial quantities of cancer cells are required and there is the need for an additional handling step when spheroids are formed outside of the microfluidics [246]–[250]. The previous approaches which form spheroids directly within microfluidic systems often rely on the use of hydrogel or ECM materials to facilitate the three dimensional growth of the tumors [247], [249], [250]. While the use of hydrogels or ECM is beneficial in providing structural support to the growing tumors, their presence around the spheroids limits the ability to deliver nutrients to the tumor [247], [249], [250]. Such growth models require the nutrients to undergo diffusion through the hydrogel materials before reaching the spheroids [247]–[250]. As such, the rate of growth for the spheroids is limited when compared to a system where nutrient delivery to the periphery of the tumor occurs unhindered. Therefore, when attempting to grow cancer spheroids as quickly as possible for use in therapeutic testing, the ability to avoid nutrient diffusion through hydrogels is important [246], [248]. We in turn have developed a system that is able to actively deliver key growth nutrients to growing spheroids in a convectively driven manner that allows for fast growth directly within the microfluidic environment along with coupled therapeutic testing.

Current methods for producing cancer cell populations for therapeutic testing require extended periods of time [244], [245], [251], [252]. Such delays typically experienced when growing cancer populations result in lost time when attempting to identify viable therapeutic treatments [244], [245], [251], [252]. In order to shorten the time delay experienced during cancer cell growth and drug screening from one or more weeks, down to just a few days requires a method of expedited growth. In order to address these issues, a microfluidic system will be developed which is capable of generating tumor spheroids in an expedited fashion utilizing convection driven nutrient delivery. The microfluidic system will be tested with adherent (spheroid forming) and non-adherent (suspension) cancer cell to verify performance across different cancer types. In addition, a mathematical model will be utilized to verify and predict the growth of the cancer within the microfluidic system. Application of mathematical model and direct imaging of the cancer populations will serve as a feedback loop to facilitate expedited cancer growth in an adaptive manner. Overall, outperforming current cancer growth techniques will serve to provide a platform better suited for therapeutic testing as shown in Table 5.1.

5.2 Experimental

5.2.1 Materials

The media used for HCT116 cells is Dulbecco's Modified Eagle's Medium (DMEM, Life Technology), with 10% fetal bovine serum (FBS, Invitrogen) and 1% Antibiotic & Antimycotic (ThermoFisher). The media used for Leukemia cells is Dulbecco's Modified Eagle's Medium + GlutaMAX (DMEM+GlutaMAX, Life Technology), with 10% heat inactivated fetal bovine serum (HI-FBS, Invitrogen) and 1% Antibiotic & Antimycotic (ThermoFisher). CellTracker Red used to fluorescently label cells (ThermoFisher). Microfluidic molds digitally cut from printable gold foil sheet (Silhouette) with Silhouette SD digital cutter (Silhouette). Microfluidic devices produced from Sylgard 184 polydimethylsiloxane (PDMS) (Dow Corning), Nuclepore polycarbonate semi-permeable membranes with 800nm pore diameter (Whatman), and microscope cover glass slides (FisherBrand). Syringe pump used for introduction of cancer cells into devices and continued culture media flow (Harvard Apparatus). Cancer cell growth monitored with combination of standard fluorescence microscopy (Olympus IX70, Hamamatsu C9300, Plan Fluor 10x & 20x, NA: 0.3, RI:1) and fluorescence confocal microscopy (Nikon C2+, Apo 4x). All image processing performed in FIGI (ImageJ) software. All other reagents not mentioned were used directly without purifying.

5.2.2 Microfluidic device fabrication

Bi-layer microfluidic platforms were produced following similar techniques outlined in previous microfluidic works from the Liu group [56]–[58], [253], [254]. The devices produced for expedited tumor spheroid growth contained a semi-permeable polycarbonate membrane that functioned to separate the apical and basal halves of the microfluidics. The circular chamber where the cancer cells were grown measured 3mm in diameter and 1.5mm in height. The straight sections of channel in the microfluidic devices measured 600µm in height and width. The use of the semi-permeable membrane within the system functioned to prevent the cancer cells introduced into the system from being washed downstream and out of the channel, which had an average pore diameter of 800nm. A depiction of the microfluidic setup can be viewed in Fig 5.1.

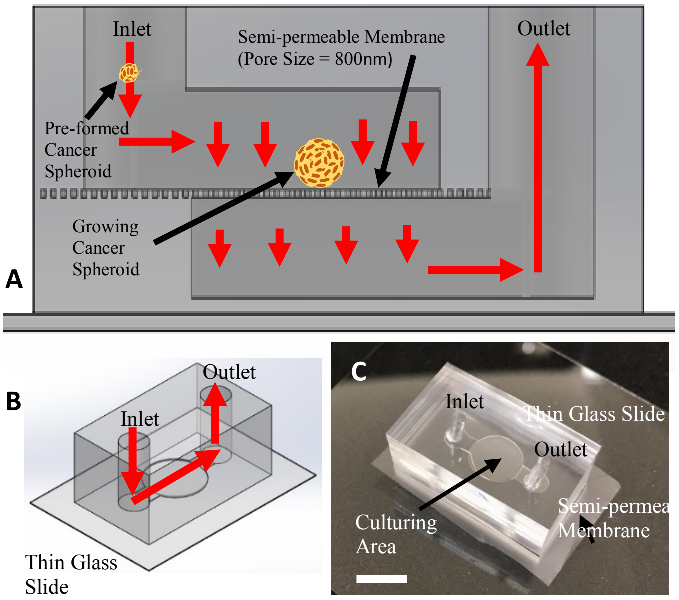

Figure 5.1 Microfluidic device schema depicting device structure and cancer cell capture function utilizing semi-permeable membrane. Flow direction indicated by red arrows. (A) Device schema cross-section. (B) Device schema overview. (C) Image of sample microfluidic device utilized in experimental testing (white scale bar is 3mm long).

In addition to the bi-layer device designed to facilitate the growth of single tumors, a larger format microfluidic device was developed in order to facilitate larger scale growth for high throughput screening applications. The high throughput screening system was modeled after standard well plate systems designed for use in plate readers. The microfluidic model relies on the use of channels integrated into the lid of the well plate system to facilitate fluid flow to the individual wells of the device. Each well of the device is connected to another well via a microfluidic channels that are mounted onto the bottom of the plate. The size and geometry of the microfluidic channels are varied based on desired testing outcomes. Fig 5.2 depicts a CAD version of the modeled prototype along with images of the 3D printed prototype used to validate the overall function of the system. The validation of the prototype design involved flowing FITC dye through the device in the apical channel and measuring the fluorescence intensity of the dye that freely transported into the basal channel. The testing was run at various concentrations of FITC dye and compared to equal concentrations of the dye present under static conditions in a standard well plate.

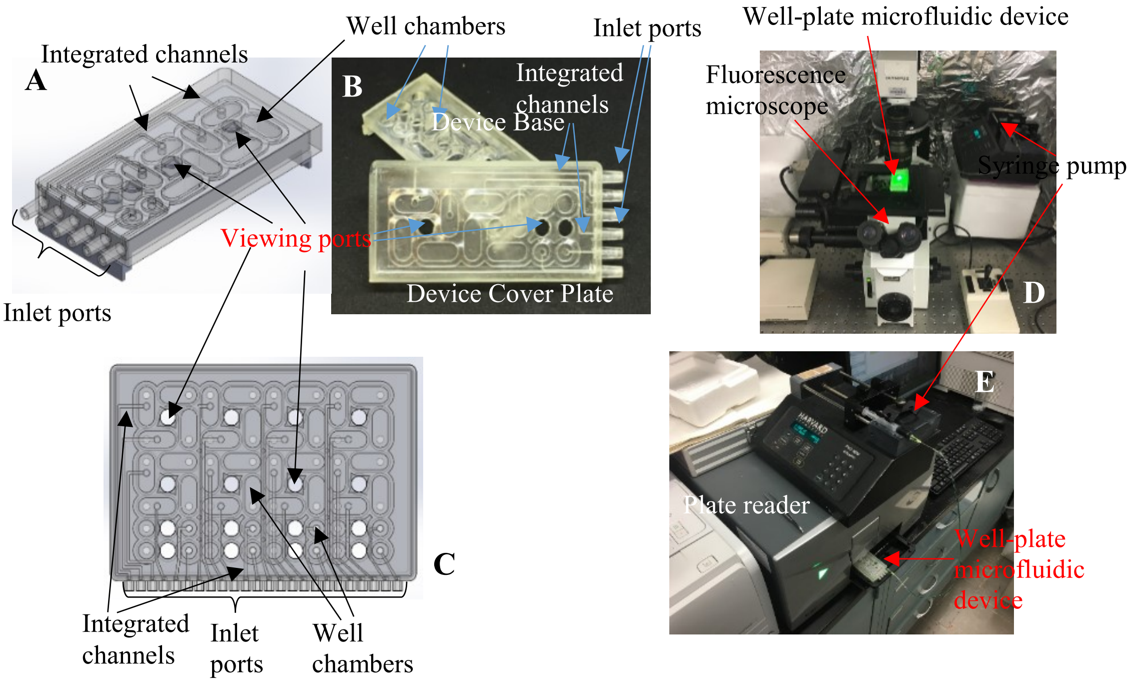

Figure 5.2 High-throughput microfluidic well plate device. (A) Partial CAD prototype used to produce 3D printed device. (B) Image of 3D printed prototype used to validation testing in the plate reader. (C) Full CAD prototype. (D) Representative image of 3D printed prototype being used to scan FITC dye fluorescence intensity with a fluorescence microscope. (E) Representative image of 3D printed prototype being used to scan FITC dye fluorescence intensity with a plate reader.

5.2.3 Leukemia cell growth

Leukemia cancer cells were flown into the system using a syringe pump (PHD 2000, Harvard Apparatus) with culture media (DMEM(1x) + GlutaMAX – I (gibco, life technologies), 10% HI-FBS (Sigma-Aldrich), 1% Penn/Strep Antibiotic(1X) (gibco, life technologies)). Due to the small pores of the semi-permeable membrane, the cancer cells were captured by the membrane and all held in the same viewing plane within the devices. The initial count of cells introduced into all devices was held constant at $1X10^5$, which corresponds to the lower end of the range of leukemia cells per milliliter typically drawn in patient samples [255]–[258]. Culture media was continuously flown within the devices for the flow based test cases. Static test cases, only received an initial influx of culture media during the cell seeding process. For flow based tests, specific flow rates of $3.4X10^3$μL/hr and $3.4X10^4$μL/hr were generated in order to introduce a large quantity of nutrients into the growth system.

5.2.4 HCT116 spheroid growth

Tumors were grown using HCT116 human colorectal cancer cells. All spheroids utilized in this work were grown from an initial suspensions of 30 cells which were pre-formed into loose tumor spheroids via an 8 hour incubation in a low adhesion round bottom well plate under static conditions. The pre-formed spheroids were then collected and flown into their respective microfluidic devices. Once inside the microfluidic devices, the semi-permeable membrane functioned to capture the pre-spheroids and hold them in place over the duration of the experimentation. The same process of an 8 hour incubation in a low adhesion well plate to pre-form spheroids was utilized for the static based tests. After pre-forming the initial static test case spheroids, Matrigel was added to the well plate in order to further facilitate spheroid growth over the course of 120 hours. Tumor spheroids grown under flow conditions were established as noted in the leukemia growth section at specific flow rates of $3.4X10^3$μL/hr and $3.4X10^4$μL/hr.

5.2.5 Minimum cell growth requirements

In order to determine the minimum number of HCT116 cells required to produce tumor spheroids, a range of initial cell counts were tested within the microfluidic device. HCT116 cells were pre-clustered for 8 hours in low-adhesion 96 well plates in order to form loosely associated pre-spheroids as described in the previous section. The cells were maintained under standard culturing conditions coupled with slow swirling of the entire plate on a shaker for 4 hours followed by static culturing for the remaining 4 hours. Once the pre-spheroids were formed and stable enough to be transported out of the wells, a syringe was used to transfer the spheroids into the microfluidic devices as described above. Further culturing of the spheroids occurred within the microfluidic devices following the protocol described above for the HCT116 cells. The total range of initial cell counts tested was: 1, 3, 5, 8, 10, 13, 15, 18, 20, 23, 25, 28, 30, and 33. Three rounds of testing were performed with 8 replicates of each initial cell count run per round. The frequency of successfully forming pre-spheroids for each initial cell count can be seen in Fig 5.3.

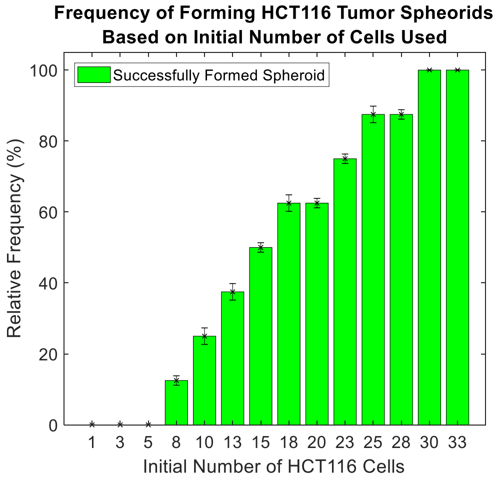

Figure 5.3 Relative frequency of HCT116 tumor spheroid formation based on the initial number of cancer cells introduced into the microfluidic device (n=24). No spheroid formation is observed between 1 and 5 cells. The smaller number of cells required to form a spheroid is 8 cells with roughly a 12.5% likelihood of success. Consistent (100%) spheroid formation occurs when using 30 cells or higher.

5.2.6 Cancer growth measurements

Cancer growth was monitored daily over the course of five days with brightfield and fluorescence imaging. All data collected from the leukemia growth studies was accomplished using CellTracker^{TM} Stain (10µM red, Thermo Fisher Scientific) and standard fluorescence imaging (Olympus IX70, Hamamatsu C9300, Plan Fluor 10x & 20x, NA: 0.3, RI: 1). Data collection for spheroid growth was accomplished utilizing CellTracker^{TM} Stain (10µM red, Thermo Fisher Scientific) and confocal microscopy (Nikon C2+, Apo 4X). Images of each cancer growth set-up were captured every 12 hours over the course of 5 days. All images were processed with FIGI (ImageJ) in order to measure HCT116 tumor sizes and cell counts for leukemia tests.

5.2.7 Statistical analysis

Statistical analysis of all obtained results were run utilizing IBM's SPSS statistical software package (IBM Corp.). All of the figures have significant differences indicated above elements within the plots. One way ANOVA tests were run for each data set with confidence levels of 95% held throughout all plots. All analyses were carried out under conditions of Tukey equal variances assumed, along with tests of homogeneity of variance further verified by both Brown-Forsythe and Welch analyses. All line plots show statistically significant differences in means compared against the baseline tests for the statically grown cancer cells, indicated by "*". Significance between 3.4X10^{3}μL/hr and 3.4X10^{4}μL/hr test data is indicated by " ** ", noting that all differences are given at a confidence level of 95%. Sample sizes for all experimental testing were determined by performing estimation for multiple-sample one-way ANOVA pairwise comparison based on pilot studies utilizing the standard sample size approximation of: $\boldsymbol{n_{ij}} = \frac{2(z\frac{a}{2\tau}+z\beta)^2\sigma^2}{\varepsilon_{ij}^2}$.

5.3 Results and Discussion

5.3.1 Microfluidic device fabrication

A microfluidic platform has been developed which is capable of delivering a continuous nutrition supply to growing cells. The microfluidic device channels are made of Polydimethylsiloxane (PDMS) through standard photolithography [56], [57], [254], [259]. Both the upper and lower channels are comprised of a short straight section of channel which leads into a large circular portion. The width of the straight sections for both channels are 600μm and the diameter of the circular portion is 3mm. The height of the both upper and lower channels is also 1.5mm over the entire length of the straight and circular channel regions of the device. Fig 5.1 shows the overall design and layout of the microfluidic platform. The upper and lower channels of the device are separated by a polycarbonate semi-permeable membrane that contains uniformly distributed pores with 800nm diameters. The presence of the semi-permeable membrane functions to retain cancer cells and tumor spheroids inside of the device and serves to keep all cells in the same viewing plane. The pores in the semi-permeable membrane also allow transport of culture media and cellular waste products through and out of device. Using the microfluidic system, non-adherent cancer cells and small preformed tumor spheroids can be grown and monitored over long time durations of a week or more.

In addition to the microfluidic configuration shown in Fig 5.1, tumor growth was attempted in a reverse manner where the pre-spheroids and culture media were flown into the basal channel and pressed up against the bottom of the semi-permeable membrane. This particular configuration functioned well when the tumor spheroids were small and could be suspended up against the bottom of the membrane (up to first 72 hours), however as the spheroids grew in size, they became too heavy for the fluid flow to support (72 hours and beyond). As a result, the spheroids dropped to the bottom of the basal channel and were prone to move around within the channel as the culture media flow pushed them.

Besides the reverse configuration, an approach was tested where the tumor spheroid were flown into channels with metal wire mesh running across the cross-section of the channel. This approach utilized mesh with a larger pore size compared to the semi-permeable membrane opted for in the final version. The use of metal mesh resulted in issues with imaging because the mesh was not transparent and portions of the tumors were not visible.

Additionally, the larger pore size of the metal mesh allowed the tumor spheroids to grow around and engulf the mesh which is not ideal if the tumors need to be recovered from the devices and because the influence of the mesh on the growth of the tumors introduces additional variable to be considered. Lastly, the fabrication of the devices with a metal mesh screen running across the cross-section of the channel was difficult and frequently suffered from leaking which is not ideal for controlled flow assisted growth experimentation.

As a result, the microfluidic device configuration shown in Fig 5.1 was chosen as the most suitable option to provide ease of use, ease of imaging, ability to recover tumor spheroids from the devices if needed for post-analysis, ease of production, and low cell adhesion properties of the semi-permeable membrane. However, the designed used to grow tumors is only capable of facilitating the growth and drug screening of a single tumor. In order to improve the throughput of the testing system, a high throughput prototype was developed to facilitate high throughput drug screening once tumors are grown.

In order to achieve high throughput screening, multiple tumors must be grown simultaneously on a single device that facilitates nutrient and therapeutic flows. As a result of the larger number of tumors being grown and tested simultaneously, faster methods of data collection are ideal to further expedite the screening process. One common technology that facilitates faster data collection are plate readers which are capable of scanning a large number of wells automatically. As such, a well plate inspired design was adopted for the high throughput screening prototype microfluidic system. The design of the well plate microfluidic system in turn was informed by the size and geometry of standard well plates to ensure a proper fit and alignment within the plate reader for data collection.

In Fig 5.2 fluid inlets into the device can be observed, where needles and tubing are attached in order to facilitate flow through the system via syringe pump. An alternative solution to facilitate fluid flow through the system would be the use of an air pressure driven system. The air pressure driven system relies on the liquid stored within each well of the plate which in turn limits the overall run time achievable without needing to interrupt the system to refill the wells with liquid. Despite this limitation, an air pressure driven system typically requires less space, as a single air pump can be used to generate the required pressure. When considering the syringe pump driven system, the benefit is that larger volumes of media or therapeutics can be flown through the device based on the size of the syringe being used. The ability to flow large volumes of liquid through the device without interruption is beneficial for long-term studies where growth or screening occur. The downside to this approach of establishing fluid flow is that the system is much larger as it requires a large number of syringes and syringe pumps that occupy additional space. However, despite the differences in establishing flow, the system can function using either approach and as such the method can be chosen based on the need of the particular experiment being run.

The validation of the prototype model utilized syringe pumps to facilitate the flow of FITC dye through the device. The fluorescence intensity of the FITC dye within the device was used to verify that readings from the microfluidic well plate system agreed well with standard well plates at varying concentrations. Fig 5.4 depicts the fluorescence intensity of the FITC dye measured in the basal channel of the microfluidic well plate and a standard well plate over the concentration range of 1μM to 250μM. From the data shown in Fig 5.4, a good agreement between the two systems was observed indicating that the prototype design functions well to facilitate high throughput data collection with a plate reader.

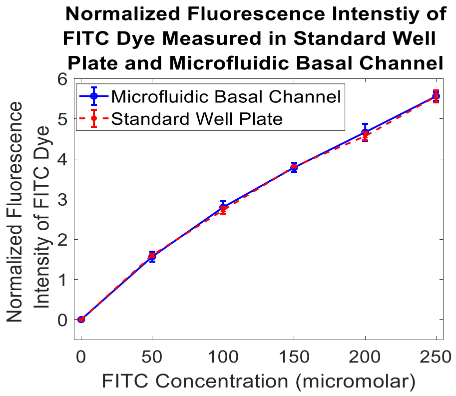

Figure 5.4 Normalized fluorescence intensities of FITC dye measured in the basal channel of the well plate microfluidic device at varying concentrations vs. the normalized fluorescence intensities of FITC dye in a standard well plate over the same concentration range.

5.3.2 Cancer cell culturing and imaging

Adherent cancer cells (HCT116) grown within the devices were first aggregated together under static culturing conditions within low adhesion well plates. The cells were added to the wells and given 8 hours to adhere into loose spheroids before being introduced into the microfluidic devices. Both leukemia and HCT116 cancer cells were successfully cultured within the microfluidic devices. Fig 5.5(C) depicts representative images of leukemia cells grown within the devices when subjected to a flow rate of $3.4X10^4$ μL/hr over the course of 120 hours. Fig 5.6(C) depicts representative images of HCT116 cells grown when subjected to a flow rate of $3.4X10^4$ μL/hr over the course of 120 hours. Both representative figures show overall increases in cell counts as time progresses as is indicated by the presented growth data in Figs 5.5(A) and 5.6(A). Additionally, control cancer populations were grown under static conditions in well plates that can be seen in Fig 5.7 (leukemia) and Fig 5.8 (HCT116).

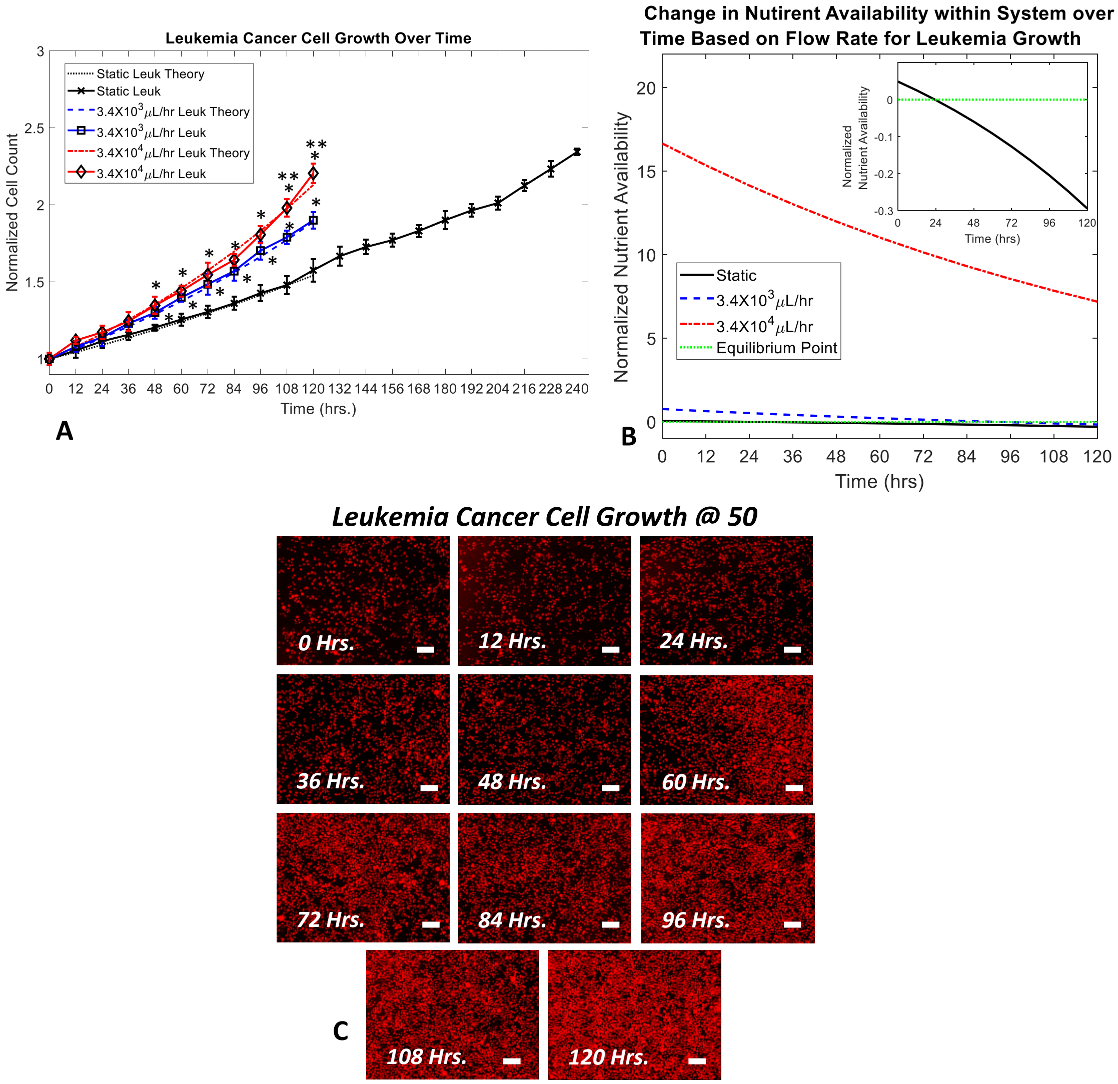

Figure 5.5 Leukemia cell growth over time based on flow conditions (10^5 cell initial count). (A) Normalized leukemia cell count over time for various flow conditions and theoretical model predictions. (B) Normalized leukemia nutrient availability within microfluidic system over time for various flow conditions. Equilibrium point indicates when nutrient availability within the system can no longer satisfy the requirements of the entire cancer cell population. Inset figure shows magnified view of the static test case crossing over equilibrium point. (C) Representative fluorescence images of leukemia cell growth over the course of 120 hours under a flow rate of $3.4X10^4$ μL/hr (stained with CellTracker Red^{TM}) (scale bars are 150μm). Statistical significance indicated by "*" between flow based tests and static conditions and "**" between flow based tests at $p \leq 0.05$.

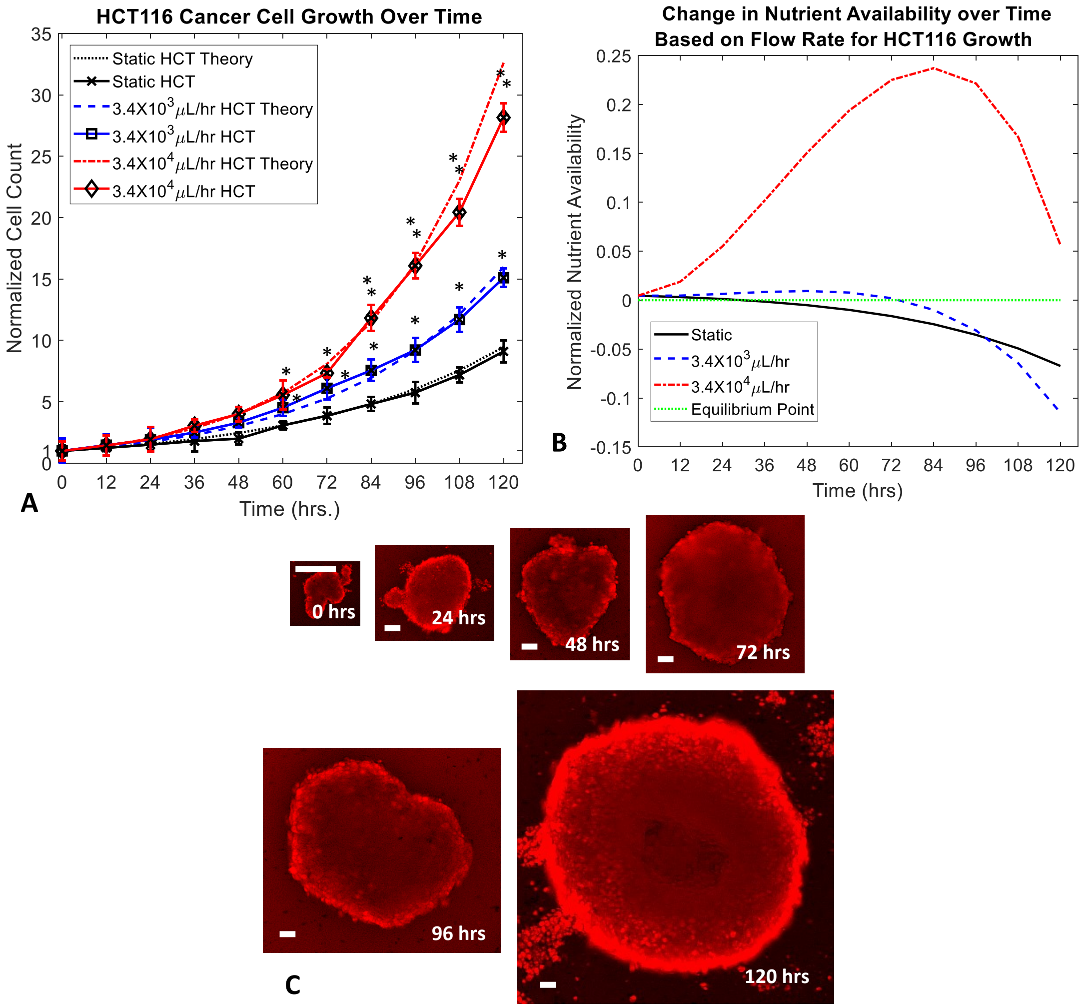

Figure 5.6 HCT116 cell growth over time based on flow conditions (30 cell initial count). (A) Normalized HCT116 cell count over time for various flow conditions and theoretical model predictions. (B) Normalized nutrient availability within microfluidic system over time for various flow conditions. Equilibrium point indicates when nutrient availability within the system can no longer satisfy the requirements of the entire cancer cell population. (C) Representative fluorescence images of HCT116 tumor spheroid growth over the course of 120 hours under a flow rate of 3.4X10^4 µL/hr (scale bars are 60µm). Statistical significance indicated by "*" between flow based tests and static conditions and "**" between flow based tests at $p \leq 0.05$.

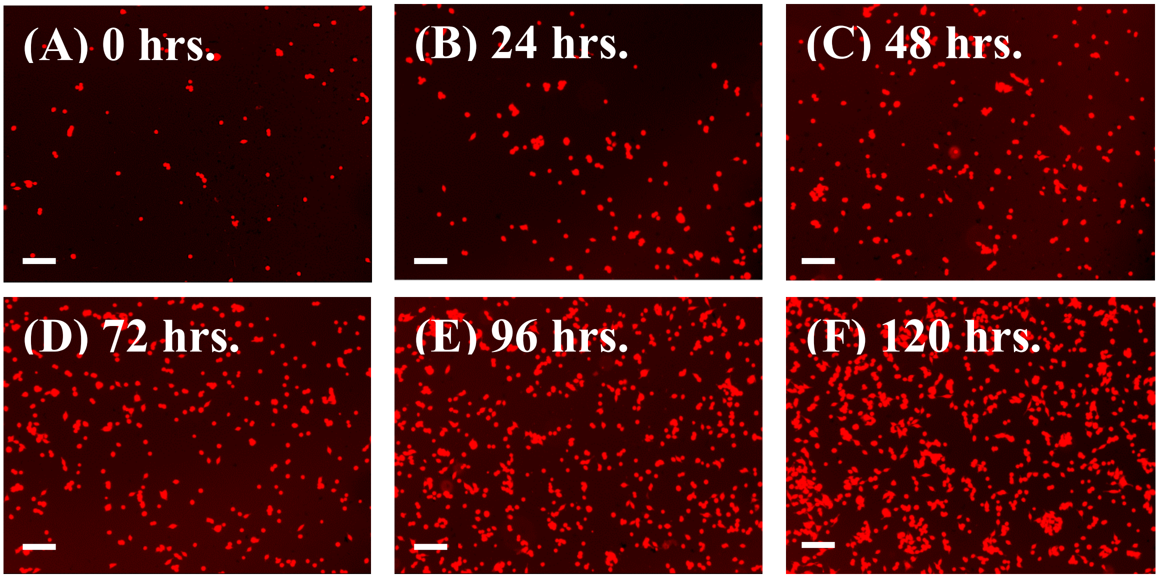

Figure 5.7 Representative fluorescent images of Leukemia cell static growth suspended in Matrigel stained with CellTrackerRed^{TM}. (A) 0 hrs. (B) 24 hrs. (C) 48 hrs. (D) 72 hrs. (E) 96 hrs. (F) 120 hrs. All white scale bars are 100µm in length.

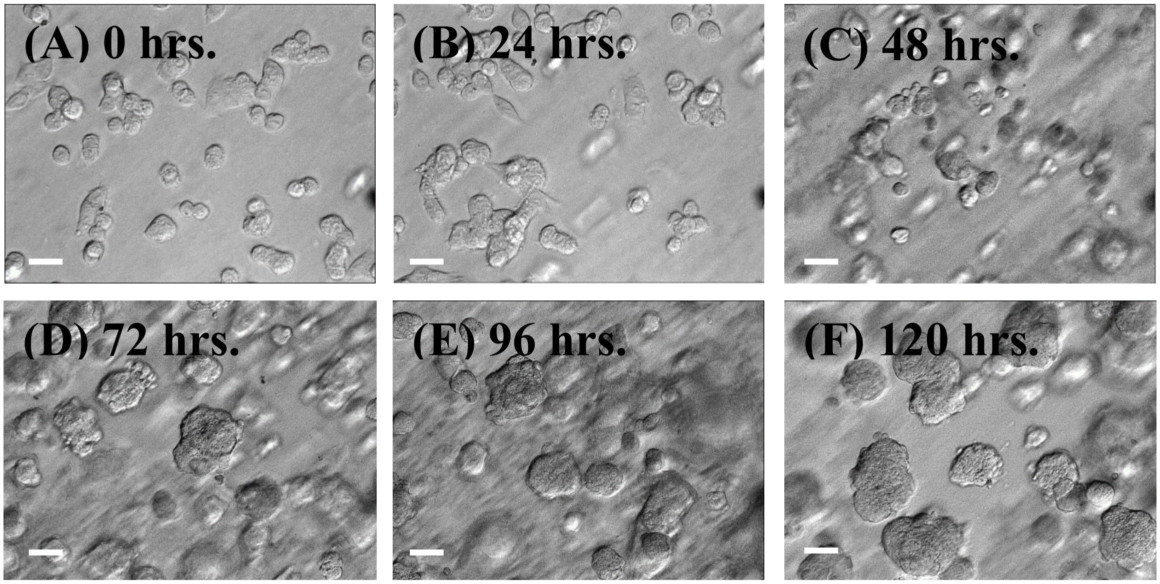

Figure 5.8 Representative brightfield images of HCT116 cell static growth suspended in Matrigel. (A) 0 hrs. (B) 24 hrs. (C) 48 hrs. (D) 72 hrs. (E) 96 hrs. (F) 120 hrs. All white scale bars are 100µm in length.

5.3.3 Cancer growth measurements and nutrient availability

Successful culturing of both adherent and non-adherent cancer cell lines was accomplished, as demonstrated by the growth of human colorectal (HCT116) and human leukemia (AR230-r), respectively, in Fig 5.5(A) and 5.6(A). Growth of the cancer populations within the devices was measured directly through confocal imaging with CellTracker^{TM} red stain. Through the application of various flow rates within the microfluidic devices, the rate of growth for the cancer cell populations was controlled, as shown in Fig 5.5(B) and 5.6(B). The use of convective flow allowed for a maximum of 1.27 to 4.76 times faster cancer cell growth when compared to the static growth cases for AR230-r and HCT116, respectively. When compared to the static test cases, introducing $3.4X10^3$μL/hr nutrient flow into the systems containing leukemia cells results in an overall increase in the cell population by a factor of 1.27 at the end of 120 hours. Similarly, the normalized number of leukemia cells present after 120 hours of growth under flow conditions of $3.4X10^4$μL/hr, was improved by a factor of 1.38. More significant were the observed increases in HCT116 growth with the $3.4X10^3$μL/hr test case resulting in a 2.47 factor increase in the cell population. Even more impressive was the observed increase in HCT116 growth when supplied with a nutrient flow of $3.4X10^4$μL/hr, which resulted in a 4.76 factor increase in the cell population. Representative images collected for static culturing conditions of both cell types can be seen in Fig 5.7 and Fig 5.8, respectively. The observed growth of both cancer types had good agreement with the theoretical predications made based on the mathematical growth model developed based on the transport of nutrients throughout tumors, as shown below. The model is a combination of equations for static cell growth that have been modified to include components of fluid transport in tissues specific for our microfluidic model and cell types utilized [260]–[266]. First the growth of the cell lines was verified under static conditions. The growth of either cell population is described by:

$N_p = N_o e^{r_o t}$ **(1)**

where N_p is the number of cancer cells after a growth time t, N_o is the initial number of cells in the population, r_o is the static growth rate constant for the particular cell type (Leuk=0.00330 & HCT=0.01937), and t is time. As time increases, the population of cells increases based on a growth rate that is specific for each cell type. Once the static growth estimations are verified to agree well with experimental results, the consumption of the entire population of cells under static conditions can be determined by:

$C_p = C_c N_p$ **(2)**

where C_p is the nutrient consumption rate by the whole population of cells and C_c is the nutrient consumption rate of an individual cell based on type. Using equations 1 and 2 provide the ability to predict the growth and rate of nutrient consumption for static growth conditions however are not suitable for make predictions when convective nutrient transport is applied to the system. In order to model growth in the system, the convective transport, diffusion and consumption of nutrients must be considered. To start, the rate of nutrient convection to the cancer population is defined differently for adherent and non-adherent cells. In the case of non-adherent cells, the rate of nutrient convection (C_{Tnad}) simply takes the form:

$c_{Tnad} = Q_{ch} \times [Nu_o]$ **(3)**

where $[Nu_o]$ is the stock media nutrient concentration and Q_{ch} is the flow rate established in the microfluidic channel. However when considering adherent cells growing in a tumor spheroid, the model requires additional considerations. Specifically, the influences of interstitial fluid pressure, channel flow rate, tumor surface area, tumor permeability, and nutrient concentration gradient within the tumor must be taken into consideration. The flow rate of interstitial fluid out of the tumor is defined as:

$$Q_{IFP} = \left(\frac{p \times q_{if} \times a_T}{3}\right) \times A_T \text{ } \mathbf{(4)}$$

where Q_{IFP} is the flow rate out the tumor resulting from interstitial fluid pressure, p is the tumor density, q_{if} is the net fluid loss from the tumor periphery, a_T is the radius of the tumor, A_T is the cross sectional area of the tumor (πa^2). The calculated flow rate of interstitial fluid leaving the tumor is subtracted from the flow rate in the channel to obtain the flow rate of nutrients interacting with the tumors surface as:

$$Q_T = Q_{ch} - Q_{IFP} \text{ } \mathbf{(5)}$$

where Q_T is the flow rate interacting with the tumor. We next determine the volume of culture media interacting with the tumor (v_T) as:

$$v_T = Q_T \times t \text{ } \mathbf{(6)}$$

In order to determine the rate of nutrient convection into the tumor, the convective flux into the tumor is determined by:

$$SV_T = \frac{SA_T}{V_T} \text{ } \mathbf{(7)}$$

$c_{flux} = P \times SV_T \times ([Nu_o] - [Nu_i])$ **(8)**

where SV_T is the ratio of tumor surface area to tumor volume, SA_T is the surface area of the tumor, V_T is the volume of the tumor, c_{flux} is the convective flux of nutrients into the tumor, P is the permeability of the tumor tissue, and $[Nu_i]$ is the interstitial nutrient concentration. Finally, the rate of nutrient convection into an adherent cell tumor (c_{Tad}) is determined by:

$c_{Tad} = c_{flux} \times v_T$ **(9)**

Beyond convection in the growth system, the amount of nutrients within the tumor relies on diffusion of nutrients. While the contribution of diffusion is relatively small when compared to convection, it is still important to consider in order to have a well developed model. It should also be noted that diffusion of nutrients is only considered for the adherent tumor spheroids and not the leukemia cancer. This is because there is no tissue for nutrient to diffuse through in the leukemia model and as such is disregarded. For the tumor spheroids, the diffusion of nutrients is defined by the concentration gradient across the tumor, the rate of nutrient diffusion in the tumor tissue, the diffusive flux of nutrients within the tissue and the surface area of the tumor as follows:

$\nabla_{Nu} = \frac{[Nu_i]-[Nu_o]}{0-a_T}$ **(10)**

$D_{flux} = D \times \nabla_{Nu}$ **(11)**

$D_T = D_{flux} \times SA_T$ **(12)**

where ∇_{nu} is the concentration gradient of nutrients within the tumor, D_{flux} is the diffusive flux of nutrients into the tumor, D is the diffusion coefficient of nutrients into the tumor, and D_T is the rate of nutrient diffusion into the tumor. Once the rates of nutrient convection and diffusion into the tumor have been determined, the change in nutrient availability within the tumor (Δ_{Nu}) at any given time point can be calculated as:

$$\Delta_{Nu} = (C_T + D_T - C_p) \times t \quad \textbf{(13)}$$

Then in order to determine an updated growth rate to use in the cell growth equation, the average nutrient availability (Nu_{avg}) within the tumor is calculated over the entire duration of the flow-assisted growth (120 hours in our tests):

$$Nu_{avg} = \frac{\sum_0^t \Delta_{Nu}}{t_n} \quad \textbf{(14)}$$

where t_n is the total number of time points during time-course t. From the average nutrient availability within the tumors over the growth time-course, an updated growth rate can be determined based on the specific nutrient flow rate used within the device. The equations governing the conversion of average nutrient availability to an updated growth rate are as follows:

$$r_N = \frac{(\log_b(Nu_{avg} + c) + d)}{a} \quad \textbf{(15)}$$

where *a, b, c* and *d* are constants determined based on a fit of the experimental growth rates observed and the average nutrient availability, which are cell type specific with HCT:(*a*=102.4, *b*=1000, *c*=0.0229, *d*=3.25) and Leuk:(*a*=1500, *b*=10, *c*=0.1046, *d*=8.4). r_N is the adjusted growth rate constant for each cell type. Lastly, the updated growth rate constant that is determined can be used to predict the growth curve of the cancer cells using the following equation:

$N_p = N_o e^{r_N t}$ **(16)**

It should be noted that the growth model is exactly the same as the one for the static growth cases, with the exception of the updated growth rate to reflect the changes introduced as a result of nutrient flow within the system. Values which were set based on literature values include: C_c=7.7X10^{-9} and 6.5X10^{-6} g/hr/cell for leukemia and HCT116 respectively, p=1.08 g/mL, q_{if}=0.18mL/hr, P=57.34X10^{-7}cm/sec), and D=2.57X10^{-8}cm^2/sec [260]–[266]. All other values were determined experimentally or specifically chosen based on desired experimental testing conditions.

The above set of equations were used to model the growth of both cell types under static and flow based conditions. The method of generating updated growth rate values for the flow cases has been shown to produce predicted growth curves that closely match the experimental results for the slow and fast flow rates used on both cell types. The close agreement of the models predictions and experimental results can be seen in Figs 5.5(A) and 5.6(A). In addition to predicting cell growth, the same governing model was used to predict the time point at which the rate of nutrient delivery into the tumor balances with rate of nutrient consumption by cells within the system, referred to as an equilibrium point. The predicted timeframes in Figs 5.5(B) and 5.6(B) for these equilibrium points, corresponds to the timeframes when the cancer growth curves in Figs 5.5(A) and 5.5(B) fall behind the maximum growth curve (red curves). As an example, the nutrient availability graph in Fig 5.6(B) for the HCT116 spheroids, predicts that the amount of available nutrients in the tumor will drop below the total nutrient demand of the tumor for the $3.4X10^3$µL/hr test case (blue curve) around hour 72. This prediction of insufficient nutrient supply to feed the entire tumor around hour 72 corresponds well with the point in time when the $3.4X10^3$µL/hr test case (blue curve) in Fig 5.6(A) drops away from the $3.4X10^4$µL/hr test case (red curve) which still has a sufficient supply of nutrients around hour 72. The ability to make such predicts along with the close predictions of both static and unrestricted nutrient supply ($3.4X10^4$µL/hr test case) cell growth for both cell types indicates that the model developed to describe the nutrient delivery within the microfluidic system closely mimics what occurs during experimental testing.

Based on the observed results and predictions made by the developed mathematical model, the $3.4X10^4$µL/hr test case for both cell types showed continuous expedited cell growth even at 120 hours, while the static and $3.4X10^3$µL/hr test cases entered into conditions of insufficient nutrient supply for the entire cell populations prior to reaching the 120 hour time point. Additionally for the $3.4X10^4$µL/hr test cases, sufficient cancer cell populations were reached around hour 72, indicating that therapeutic screening could commence after 72 hours of culturing within the device.

In order to further verify the formation of spherical tumor clusters, representative confocal scans were periodically run. Fig 5.9 depicts one of the representative confocal scans showing a typical spherical tumor cluster produced within the microfluidic system. Additionally, the expression of E-Cadherin under static and flow conditions were tested in 2D and 3D cultures as shown in Fig 5.10. The level of expression between all 4 groups tested were very similar indicating that no major changes in cell-cell junction protein expression were occurring as a result of the expedited 3D growth system. Lastly, in order to test the systems capability to grow tumor spheroid from limited amount of cells, a set of tumor spheroid growth experiments were run which utilized a range of initial cell numbers in the devices to grow tumors. A process of pre-clustering the cells into loose spheroids was utilized which involved a slow swirling of the cancer cells in a low adhesion well plate for 4 hours followed by 4 hours of static culture, both under standard culturing conditions. The resulting loosely associated spheroids after 8 hours could be transferred into the microfluidic devices for further culturing. The results in Fig 5.3 indicate that a minimum of 8 cells are required for this growth technique with a likelihood of success around 12.5%. Further testing indicated that the initial use of 30 cells or more almost guaranteed the formation of tumor spheroids for growth within the device.

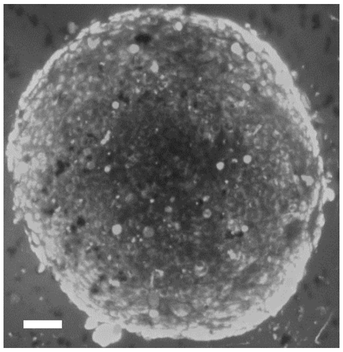

Figure 5.9 HCT116 tumor spheroid grown in microfluidic device displaying high degree of sphericity. White scale bar is 60μm in length.

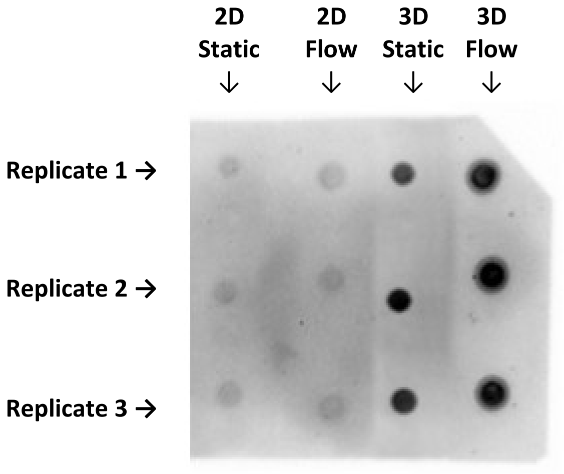

Figure 5.10 Dot plot testing results for E-Cadherin screening. Similar levels of E-Cadherin expression are observed for static and flow conditions for both two-dimensional and three dimensional cancer cell growth.

5.4 Conclusions

From this work, a platform for the expedited growth of cancers is offered which can function with both adherent and non-adherent cell lines. The overall goal of the study was to demonstrate the influence of active convective flow on the growth rate of cancer cell populations within the microfluidic system. The system has been shown to facilitate a range of culturing conditions from static up to flow rates of $3.4X10^4$µL/hr which influence the rate at which cancer cells grow over the course of 120 hours. The design of the device allows for direct observations and measurements of the HCT116 and leukemia cancer population to be made via brightfield and fluorescence microscopy over the entire time-course of the study. In addition, the prototype high throughput well plate device was shown to function well in a plate reader when measuring the fluorescence intensity of FITC dye at various concentrations. The validation of the high throughput prototype design, allows for improvements in the fabrication process and material choices in order to facilitate the growth of cells on the platform. Because 3D printing was used to produce the current prototype, harsh chemicals exist within the device that do not facilitate cell growth of any kind. Future work involving cell growth will act to further validate the functionality of the high throughput system. However, in the meantime the individual microfluidic devices were used to validate the process of expedited tumor growth.

The outcomes from this work indicate that the growth of both cell types are assisted by the active convective flow of nutrients through the devices. The degree of growth improvement has been shown to be controlled by the type of cell being used and the flow rate at which nutrients are introduced into the devices. Overall, the improved growth of the leukemia cells with the addition of nutrient flow was less than the improvement observed when flow was applied to the HCT116 cells. This difference in growth improvement is attributed to a couple of factors. The first is that the leukemia cells are non-adherent cells and as such, do not grow in a tightly associated spheroid. The leukemia cells spread out, growing in the same plane of the device and as such nutrient transport to a given cell in the population is not hindered by any surrounding cells. The HCT116 cells grow as a single mass making it difficult to deliver nutrients to cells within the tumor without the aid of convection. Therefore when convection driven nutrient transport is applied, the HCT116 tumor mass receives more benefit when compared to the individually growing leukemia cells as nutrients are forced further into the core of the HCT116 spheroids. The second reason why a more significant improvement in HCT116 growth was observed when compared to the leukemia cells is because the HCT116 cells have a naturally faster growth rate even under static conditions. The faster growth rate for the HCT116 cells allows the cells to turn over new generations of cells in a shorter period of time, which then can go on to further take advantage of the excess nutrients supplied by the culture media flow. When compared to the static test cases, introducing $3.4X10^3 \mu L/hr$ nutrient flow into the systems containing leukemia cells results in an overall increase in the cell population by a factor of 1.27 at the end of 120 hours. Similarly, the normalized number of leukemia cells present after 120 hours of growth under flow conditions of $3.4X10^4 \mu L/hr$, was improved by a factor of 1.38. More significant were the observed increases in HCT116 growth with the $3.4X10^3 \mu L/hr$ test case resulting in a 2.47 factor increase in the cell population. Even more impressive was the observed increase in HCT116 growth when supplied with a nutrient flow of $3.4X10^4 \mu L/hr$, which resulted in a 4.76 factor increase in the cell population.

The increased growth observed under flow conditions for both cancer types is attributed to the convective flow of nutrients to the cancer cells. While static culturing conditions rely purely on diffusion of nutrients within the system, the application of convective flow provides a continuously refreshed source of nutrients while also removing cellular waste excreted by the cancer cells. This two-fold effect in turn can be used to ensure that the cells growing in the population are never lacking nutrients. The function of the convective nutrient flow for the spheroid based tests also facilitates deeper penetration of fresh nutrients into the core of the tumors because the flowing nutrients are forced between intercellular gaps in the tumor tissue. When compared to static cultures, the nutrient transport through intercellular gaps can only occur via diffusion which requires long periods of time for transport over such long distances to reach the cores of the growing tumors. As such, static culturing conditions often result in necrotic tumor spheroid cores as demonstrated heavily in literature [267]–[271].

Besides simply observing expedited growth of cancer populations under such convective flows of nutrients, a mathematical model has been developed to describe and predict the outcomes of such flow experiments. The mathematical model has been based on the active convection of nutrients resulting from flow, the passive diffusion of nutrients within the spheroids, and the consumption of nutrients by the cancer cell populations over time. The developed model has been simplified for ease of use, with the major factors resulting in the growth of cancer populations being taken into consideration. Despite the simplified nature of the model, good agreements with experimental testing have been achieved which indicates that the model can be used to predict the growth of cancer cells within the microfluidic system. The application of the model in a predictive manner in conjunction with the microfluidic growth system can result in expedited cancer growth of adherent and non-adherent cancer cells for therapeutic screening or genetic analysis. In addition, the models ability to predict nutrient availability within the growth system, allows for a control feedback loop to be established in order to vary the nutrient supply rate to maximized cell growth while limiting waste. An example of such a feedback loop would involve the continuous monitoring of cell growth which in turn would be used to update the mathematical model. The initial nutrient supply rate can be very low and slowly increased as the cell population grows over time. By doing so, expensive reagents can be used sparingly while not limiting the total potential growth of the cancer cells. As a final note, the predictive nature of the developed model shows good agreement with the timeframes when variations in experimental cell growth were expected. By predicting the availability of nutrients within the system, it is possible to identify how long it will take before the cell population runs into a deficit of nutrients. The predicted times to reach conditions of nutrient deficit for each testing condition (static and two flow cases) correspond well with the time points in the experimental data where the static and slow flow rate growth curves fall behind the growth of the faster flow rate. This correlation between the predicted and observed results indicates that the developed model is sufficient enough to represent the experimental conditions being tested.

As a final analysis, the minimum number of required HCT116 cancer cells required to successfully form tumor spheroids was tested. The conclusions indicate that at least 8 cells must be present in order to successfully form a spheroid with a success rate of around 12.5%. However, when 30 cells or more are used within the device to produce a spheroid, the successful formation of such a spheroid is almost guaranteed. These results are important to understand if such a device is to be used in a clinical setting with very limited number of cells from patient samples. The number of such cells collected from patient samples are typically very low and as such, having a method to successfully form spheroids for drug screening will need to function under such conditions. It should be noted however that the cells used in this study were well established cell lines routinely grown in a laboratory setting. Future work along these lines will include tests run with patient derived cancer cells in order to more fully validate the system for potential future use in the clinical space.

Overall, the developed microfluidic system has been shown to facilitate the growth of adherent and non-adherent cancer cell types in an expedited fashion through the application of nutrient flow. The improvement in cancer cell growth is attributed to the continuous convective delivery of fresh nutrients to the cells while also actively removing cellular waste. The expression of cell-cell adhesion molecule E-Cadherin has also been examined to show that the growth method does not interfere or influence the normal phenotypic expression of such cell-surface proteins. The developed mathematical model has been shown to serve as a good predictor of cancer growth within the system and can be used as a feedback loop to adjust the rate at which nutrients are supplied to cancer cell populations. Lastly the minimum require number of HCT116 cells has been determined in order to successfully form tumor spheroids with the microfluidic system. As a final overview of the entire dissertation, a summary and outlook for each individual work is noted in the following chapter.

Chapter 6: Summary and Outlook

The dissertation described several techniques that may significantly benefit cancer therapeutic discovery and *in vitro* cancer model generation. The research of the dissertation was mainly geared around techniques and models designed to facilitate the analysis of cancer therapeutics and therapeutic carriers such as nanoparticles. First, a single layer microfluidic device was developed which facilitated cancer cell monolayer growth and was used to screen solid lipid nanoparticle formulations designed to target cancerous tissue using various anti-EpCAM and PEG surface coatings. Second, the microfluidic system was improved to a bi-layer setup that facilitated the introduction of a mimicked blood vessel and cancerous region in order to study the influence of vascular permeability on therapeutic transport from the vessel to the cancer monolayer. Third, the same microfluidic setup was used to analyze the delivery of nanoparticles of various shapes as potential therapeutic carriers in order to improve delivery to cancerous microenvironments. Lastly, in order to better realize a more physiologically relevant cancer microenvironment, a bi-layer microfluidic system was developed which was capable of producing tumor spheroids in an expedited fashion for therapeutic screening applications. Next, brief summaries and future outlooks are discussed for each project.

6.1 Assessment of PEGylated cancer targeting solid lipid nanoparticles in a microfluidic device

Targeted treatment of disease conditions such as cancerous sites requires delivery of therapeutics directly to the diseased site with minimized therapeutic interaction with surrounding tissue. The use of functionalized nanoparticles is one approach to achieve the goal of targeted delivery strictly to diseased tissue through the use of antibodies and polymer chain coatings. This work uses a microfluidic platform capable of growing cancer cells in confluent monolayers to test various anti-epithelial cell adhesion molecule and polyethylene glycol surface coating densities on solid lipid nanoparticles with the goal of increasing targeted delivery while limiting non-specific adhesion. The amount of non-specific binding of bare solid lipid nanoparticles was shown to not change with the presence or absence of cancer cells within the microfluidic devices. Total amounts of solid lipid nanoparticle binding were shown to decrease with increased shear rates and increased polyethylene glycol surface coating percentages. A polyethylene glycol surface coating percentage of 37% was observed to provide the greatest amount of cell bound solid lipid nanoparticles when compared to the total amount of solid lipid nanoparticle binding within the microfluidic devices. Overall, a general trend has been observed where the percentage of cell specific binding compared to the total binding starts out very low when no polyethylene glycol is present on the surface of the solid lipid nanoparticles. As the polyethylene glycol coating percentage increases, an overall increase in the percentage of cell specific binding was observed up to a polyethylene glycol coating of 37%, after which the percentage of cell specific binding decreases when compared to the total binding. From such findings, it is proposed that addition of polyethylene glycol onto the surface of the solid lipid nanoparticles assists in reducing non-specific binding to a certain point, after which further addition of polyethylene glycol over-crowds the surface of the solid lipid nanoparticles and begins to hinder the normal function of target specific antibodies such as anti-epithelial cell adhesion molecule. As such, a careful balance exists where antibody derived targeted binding is enhanced through the addition of polyethylene glycol polymer chains which function to reduce non-specific adhesion without hindering the targeted function of the antibody. Utilizing this knowledge, future testing is planned to use SLNPs with active therapeutic loads to confirm that the 37% PEG surface coating percentage produces the greatest amount of therapeutic impact for reducing cancer cell populations within the microfluidic devices. In addition, future testing will also be conducted to see if linker molecules can be used to offset the location of the target antibodies further away from the surface of the SLNP to allow for higher PEG coating percentages to be used without interference. Using such an approach may serve to better reduce the non-specific adhesion of such SLNPs while still providing a means of targeted delivery to sites of cancerous tissues.

6.2 Biomimetic microfluidic platform for the quantification of transient endothelial monolayer permeability and therapeutic transport under mimicked cancerous conditions

Therapeutic delivery from microvasculature to cancerous sites is influenced by many factors including, endothelial permeability, vascular flow rates/pressures, cancer secretion of cytokines and permeabilizing agents, and characteristics of the chosen therapeutics. This work, uses bi-layer microfluidics capable of studying dye and therapeutic transport from a simulated vessel to a cancerous region while allowing for direct visualization and quantification of endothelial permeability. 2.5 to 13 times greater dye transport was observed when utilizing small dye sizes (FITC) when compared to larger molecules (FITC-Dextran 4kDa and FITC-Dextran 70kDa), respectively. The use of lower flow rates/pressures are shown to improve dye transport by factors ranging from 2.5 to 5 times, which result from increased dye diffusion times within the system. Furthermore, subjecting confluent endothelial monolayers to cancerous cells resulted in increased levels of vascular permeability. Situations of cancer induced increases in vascular permeability are shown to facilitate enhanced dye transport when compared to non-diseased endothelial monolayers. Subsequent introduction of paclitaxel or doxorubicin into the system was shown to kill cancerous cells resulting in the recovery of endothelial confluency overtime. The response of endothelial cells to paclitaxel and doxorubicin are quantified to understand the direct influence of anti-cancer therapeutics on endothelial growth and permeability. Introduction of therapeutics into the system showed the recovery of endothelial confluency and dye transport back to conditions experienced prior to cancer cell introduction after 120 hours of continuous treatment. Overall, the system has been utilized to show that therapeutic transport to cancerous sites depends on the size of the chosen therapeutic, the flow rate/pressure established within the vasculature, and the degree of cancer induced endothelial permeability. In addition, treatment of the cancerous region has been demonstrated with anti-cancer therapeutics, which are shown to influence vascular permeability in direct (therapeutics themselves) and indirect (death of cancer cells) manners. Lastly, the system presented in this work is believed to function as a versatile testing platform for future anti-cancer therapeutic testing and development. Future applications of this technology towards early stage testing of personalized therapeutic options has the potential of utilizing patient derived cells as a means of improving the delivery and effectiveness of therapeutic systems. Future work for the system is being focused on improving functionality for improved testing. Some specific improvements include the establishment of a more diversified set of applications for additional disease models (inflammation and gastrointestinal drug delivery), establishment of culturing procedures to provide a wider range of cell types to be used, and introduction of a 3D environment for growth of tumor spheroids as opposed to monolayers of cancer cells as utilized in the current work.

6.3 The shape effect on polymer nanoparticle transport in a blood vessel

Nanoparticle therapeutic delivery is influenced by many factors including physical, chemical, and biophysical properties along with local vascular conditions. In recent years, nanoparticles of various shapes have been fabricated and have shown significant impact on transport efficiency. Identification of which nanoparticle shape helps to improve the therapeutic delivery process allows for enhanced therapeutic effect, yet is hard to be quantified *in vivo* due to the complex nature of the *in vivo* environment. In this work, we turn to biological models as a guide for informing improved nanoparticle therapeutic delivery, and quantify the contribution of various factors on delivery efficiency. Here we showed that with a mimetic blood vessel, improved therapeutic delivery was achieved using long filamentous rod nanoparticles under low-pressure conditions. When considering medium pressure conditions, a combination of nanoparticle shapes presents improved therapeutic delivery over the treatment time-course starting with long filamentous rod nanoparticles, followed by short rod nanoparticles. Conditions of high pressure required a combination of short rod nanoparticles, followed by spherical nanoparticles to achieve enhanced therapeutic delivery. Overall, improvement of therapeutic delivery via nanoparticle carriers is likely to require a combination of nanoparticle shapes administered at different times over the treatment time-course, given patient specific conditions. Future work geared around additional nanoparticle shapes and shape-changing particles may offer carriers even better adapted for therapeutic delivery to diseased sites. In addition, more diverse future studies of various disease conditions beyond tumor environments are possible which could utilize nanoparticles carrying therapeutic loads.

6.4 Bi-layer microfluidic platform for expedited tumor growth towards drug evaluation

Patient derived organoids have recently emerged as robust preclinical models. Such organoid models have included ovarian and leukemia cancers, as progression of the disease in patients can occur quickly making it difficult to treat at later stages with chemotherapeutics. Current 2D culturing methods do not provide a physiological response when treated with therapeutics that leads to the potential of selecting inappropriate therapeutics for treatment *in vivo*. New cancer models are being developed which are capable of culturing 3D tumors that more closely reproduce physiological responses observed *in vivo*. Despite the advances made by such 3D culturing system, the experimental setup often requires long periods of time to grow tumors in *in vitro* or *in vivo* environments. The duration of growth for such 3D models can take anywhere from a week to a month to fully establish before any therapeutic testing can occur. Additionally, such growth system often require large initial populations for cells to facilitate the formation of tumors for therapeutic testing. Due to the relative rarity of cancer cells for some cancer types, these 3D growth methods are often not feasible options for drug screening. As a solution to these issues, a 3D culturing system has been developed which is capable of producing physiologically relevant tumors in an expedited fashion while only requiring a small number of initial cancer cells. A bi-layer microfluidic system has been developed which is capable of facilitating active convective nutrient supply to populations of cancer cells. The system has been shown to function well with adherent and non-adherent cell types by expediting cell growth by a factor ranging from 1.27 to 4.76 greater than growth under static conditions. Utilizing such an approach has enable to formation of tumors ready for therapeutic screening within 3 days utilizing a method of dynamic nutrient supply. A mathematical model has been developed which allows adjustments to be made to the dynamic delivery of nutrients in order to efficiently use culture media without excessive waste. We believe this work to be the first attempt to grow cancers in an expedited fashion utilizing only a convective nutrient supply, which has the potential to offer improved drug screening for patients in clinical settings. There exists many routes of future work along the lines of the developed cancer growth device. Such future work will include the incorporation of therapeutic testing after the formation of spheroids by introducing therapeutic doped media into the flow of the system. Such therapeutic based studies will function to further validate the response of spheroids within the system, while using *in vivo* clinical data for the tested therapeutics as benchmarks. Further expediting the growth of cancer cell populations will also be tested through the introduction of growth factors into the nutrient flow. However, changes in cell phenotype and protein expression will need to be closely monitored to ensure that the system is still representative of phenotypically normal conditions. Lastly, further testing of additional cancer cell types, both established and patient derived, is needed to expand the scope of the model as a whole. Tests run with patient derived cancer cells will also serve to identify the minimum number of cells required for successful formation of spheroids for potential clinical use in drug screening assays and genetic analyses.

References

[1] A. M. H. Krebber, L. M. Buffart, G. Kleijn, I. C. Riepma, R. De Bree, C. R. Leemans, A. Becker, J. Brug, A. Van Straten, P. Cuijpers, and I. M. Verdonck-De Leeuw, “Prevalence of depression in cancer patients: A meta-analysis of diagnostic interviews and self-report instruments,” *Psycho-Oncology*, vol. 23, no. 2. pp. 121–130, 2014.

[2] L. A. Torre, F. Bray, R. L. Siegel, J. Ferlay, J. Lortet-tieulent, and A. Jemal, “Global Cancer Statistics, 2012,” *CA a cancer J. Clin.*, vol. 65, no. 2, pp. 87–108, 2015.

[3] K. D. Miller, R. L. Siegel, C. C. Lin, A. B. Mariotto, J. L. Kramer, J. H. Rowland, K. D. Stein, R. Alteri, and A. Jemal, “Cancer treatment and survivorship statistics, 2016,” *CA. Cancer J. Clin.*, vol. 66, no. 4, pp. 271–289, 2016.

[4] C. G. Begley and L. M. Ellis, “Drug development: Raise standards for preclinical cancer research,” *Nature*, vol. 483, no. 7391, pp. 531–533, Mar. 2012.

[5] D. S. Alberts, O. M. Colvin, A. H. Conney, V. L. Ernster, J. E. Garber, P. Greenwald, L. J. Gudas, K. H. Waun Ki Hong, G. J. Kelloff, R. A. Kramer, C. E. Lerman, D. J. Mangelsdorf, A. Matter, J. D. Minna, W. G. Nelson V, J. M. Pezzuto, F. G. Prendergast, V. W. Rusch, M. B. Sporn, L. W. Wattenberg, and I. B. Weinstein, “Prevention of cancer in the next millennium: Report of the Chemoprevention Working Group to the American Association for Cancer Research.,” *Cancer Res.*, vol. 59, no. 19, pp. 4743–58, Oct. 1999.

[6] L. J. Solin, B. L. Fowble, D. J. Schultz, and R. L. Goodman, “The significance of the pathology margins of the tumor excision on the outcome of patients treated with definitive irradiation for early stage breast cancer,” *Int. J. Radiat. Oncol.*, vol. 21, no. 2, pp. 279–287, 1991.

[7] B. Fertil and E.-P. Malaise, “Inherent cellular radiosensitivity as a basic concept for human tumor radiotherapy,” *Int. J. Radiat. Oncol.*, vol. 7, no. 5, pp. 621–629, 1981.

[8] N. Y. Rapoport, A. M. Kennedy, J. E. Shea, C. L. Scaife, and K.-H. Nam, “Controlled and targeted tumor chemotherapy by ultrasound-activated nanoemulsions/microbubbles,” *J. Control. Release*, vol. 138, no. 3, pp. 268–276, 2009.

[9] G. Poste and I. J. Fidler, “The pathogenesis of cancer metastasis.,” *Nature*, vol. 283, no. 5743, pp. 139–46, Jan. 1980.

[10] B.-D. Chang, M. E. Swift, M. Shen, J. Fang, E. V Broude, and I. B. Roninson, “Molecular determinants of terminal growth arrest induced in tumor cells by a chemotherapeutic agent.,” *Proc. Natl. Acad. Sci. U. S. A.*, vol. 99, no. 1, pp. 389–94, Jan. 2002.

[11] Z.-G. Gao, H. D. Fain, and N. Rapoport, “Controlled and targeted tumor chemotherapy by micellar-encapsulated drug and ultrasound,” *J. Control. Release*, vol. 102, no. 1, pp. 203–222, 2005.

[12] C. Zhang, W. Wang, T. Liu, Y. Wu, H. Guo, P. Wang, Q. Tian, Y. Wang, and Z. Yuan, “Doxorubicin-loaded glycyrrhetinic acid-modified alginate nanoparticles for

liver tumor chemotherapy," *Biomaterials*, vol. 33, no. 7, pp. 2187–2196, 2012.

[13] K. M. Yamada and E. Cukierman, "Modeling Tissue Morphogenesis and Cancer in 3D," *Cell*, vol. 130, no. 4, pp. 601–610, 2007.

[14] A. Reininger-Mack, H. Thielecke, and A. A. Robitzki, "3D-biohybrid systems: applications in drug screening," *Trends Biotechnol.*, vol. 20, no. 2, pp. 56–61, 2002.

[15] C. Fischbach, R. Chen, T. Matsumoto, T. Schmelzle, J. S. Brugge, P. J. Polverini, and D. J. Mooney, "Engineering tumors with 3D scaffolds," *Nat. Methods*, vol. 4, no. 10, pp. 855–860, Oct. 2007.

[16] M. Ferrari, "Cancer nanotechnology: Opportunities and challenges," *Nature Reviews Cancer*, vol. 5, no. 3. pp. 161–171, 2005.

[17] K. Riehemann, S. W. Schneider, T. A. Luger, B. Godin, M. Ferrari, and H. Fuchs, "Nanomedicine - Challenge and perspectives," *Angewandte Chemie - International Edition*, vol. 48, no. 5. pp. 872–897, 2009.

[18] A. Jemal, R. Siegel, J. Xu, and E. Ward, "Cancer Statistics, 2010," *CA. Cancer J. Clin.*, vol. 60, no. 5, pp. 277–300, 2010.

[19] K. A. Conklin, "Dietary antioxidants during cancer chemotherapy: Impact on chemotherapeutic effectiveness and development of side effects," *Nutrition and Cancer*, vol. 37, no. 1. pp. 1–18, 2000.

[20] H. B. Nair, B. Sung, V. R. Yadav, R. Kannappan, M. M. Chaturvedi, and B. B. Aggarwal, "Delivery of antiinflammatory nutraceuticals by nanoparticles for the prevention and treatment of cancer," *Biochemical Pharmacology*, vol. 80, no. 12. pp. 1833–1843, 2010.

[21] K. K. Jain, "Nanotechnology-based Drug Delivery for Cancer," *Technol. Cancer Res. Treat.*, vol. 4, no. 4, pp. 407–416, 2005.

[22] T. M. Allen, "Ligand-targeted therapeutics in anticancer therapy," *Nature Reviews Cancer*, vol. 2, no. 10. pp. 750–763, 2002.

[23] P. Sapra, P. Tyagi, and T. M. Allen, "Ligand-targeted liposomes for cancer treatment.," *Curr. Drug Deliv.*, vol. 2, no. 4, pp. 369–81, 2005.

[24] F. X. Gu, R. Karnik, A. Z. Wang, F. Alexis, E. Levy-Nissenbaum, S. Hong, R. S. Langer, and O. C. Farokhzad, "Targeted nanoparticles for cancer therapy," *Nano Today*, vol. 2, no. 3, pp. 14–21, 2007.

[25] J. Cheng, B. A. Teply, I. Sherifi, J. Sung, G. Luther, F. X. Gu, E. Levy-Nissenbaum, A. F. Radovic-Moreno, R. Langer, and O. C. Farokhzad, "Formulation of functionalized PLGA-PEG nanoparticles for in vivo targeted drug delivery," *Biomaterials*, vol. 28, no. 5, pp. 869–876, 2007.

[26] O. Veiseh, J. W. Gunn, and M. Zhang, "Design and fabrication of magnetic nanoparticles for targeted drug delivery and imaging," *Advanced Drug Delivery Reviews*, vol. 62, no. 3. pp. 284–304, 2010.

[27] T. M. Allen and P. R. Cullis, "Drug Delivery Systems: Entering the Mainstream," *Science*, vol. 303, no. 5665. pp. 1818–1822, 2004.

[28] D. F. Emerich and C. G. Thanos, "Targeted nanoparticle-based drug delivery and diagnosis," *Journal of Drug Targeting*, vol. 15, no. 3. pp. 163–183, 2007.

[29] R. Singh and J. W. Lillard, "Nanoparticle-based targeted drug delivery," *Experimental and Molecular Pathology*, vol. 86, no. 3. pp. 215–223, 2009.

[30] P. Kocbek, N. N. Obermajer, M. Cegnar, J. Kos, and J. Kristl, "Targeting cancer

cells using PLGA nanoparticles surface modified with monoclonal antibody.," *J. Control. Release*, vol. 120, no. 1–2, pp. 18–26, 2007.

[31] S. M. Moghimi, A. C. Hunter, and J. C. Murray, "Long-circulating and target-specific nanoparticles: theory to practice.," *Pharmacol. Rev.*, vol. 53, no. 2, pp. 283–318, 2001.

[32] C. G. Uhl, Y. Gao, S. Zhou, and Y. Liu, "The shape effect on polymer nanoparticle transport in a blood vessel," *RSC Adv.*, vol. 8, no. 15, 2018.

[33] C. G. Uhl, V. R. Muzykantov, and Y. Liu, "Biomimetic microfluidic platform for the quantification of transient endothelial monolayer permeability and therapeutic transport under mimicked cancerous conditions," *Biomicrofluidics*, vol. 12, no. 1, 2018.

[34] E. Rostami, S. Kashanian, A. H. Azandaryani, H. Faramarzi, J. E. N. Dolatabadi, and K. Omidfar, "Drug targeting using solid lipid nanoparticles," *Chemistry and Physics of Lipids*, vol. 181. pp. 56–61, 2014.

[35] D. Ricklin and J. D. Lambris, "New milestones ahead in complement-targeted therapy," *Seminars in Immunology*, vol. 28, no. 3. pp. 208–222, 2016.

[36] E. W. Esch, A. Bahinski, and D. Huh, "Organs-on-chips at the frontiers of drug discovery," *Nature Reviews Drug Discovery*, vol. 14, no. 4. pp. 248–260, 2015.

[37] A. Polini, L. Prodanov, N. S. Bhise, V. Manoharan, M. R. Dokmeci, and A. Khademhosseini, "Organs-on-a-chip: a new tool for drug discovery," *Expert Opin. Drug Discov.*, vol. 9, no. 4, pp. 335–352, 2014.

[38] C. Moraes, G. Mehta, S. C. Lesher-Perez, and S. Takayama, "Organs-on-a-Chip: A focus on compartmentalized microdevices," *Ann. Biomed. Eng.*, vol. 40, no. 6, pp. 1211–1227, 2012.

[39] Š. Selimović, M. R. Dokmeci, and A. Khademhosseini, "Organs-on-a-chip for drug discovery," *Curr. Opin. Pharmacol.*, vol. 13, no. 5, pp. 829–833, 2013.

[40] C. G. Uhl, W. Shi, and Y. Liu, "Organ-on-Chip Devices towards Applications in Drug Development and Screening: A Review," *J. Med. Device*, vol. in press, 2018.

[41] N. S. Bhise, J. Ribas, V. Manoharan, Y. S. Zhang, A. Polini, S. Massa, M. R. Dokmeci, and A. Khademhosseini, "Organ-on-a-chip platforms for studying drug delivery systems," *J. Control. Release*, vol. 190, pp. 82–93, 2014.

[42] A. Skardal, T. Shupe, and A. Atala, "Organoid-on-a-chip and body-on-a-chip systems for drug screening and disease modeling," *Drug Discovery Today*, vol. 21, no. 9. pp. 1399–1411, 2016.

[43] N. Gupta, J. R. Liu, B. Patel, D. E. Solomon, B. Vaidya, and V. Gupta, "Microfluidics-based 3D cell culture models: Utility in novel drug discovery and delivery research," *Bioeng. Transl. Med.*, vol. 1, no. 1, pp. 63–81, Mar. 2016.

[44] P. Gravesen, J. Branebjerg, O. S. Jensen, J. J. H. and A. J. B. Terry S C, T. D. B. and P. R. F. W, B. P. W. and A. J. A. Zdeblick M J, T. H. H. and K. L. Bassous E, P. K. E, P. K. E, van de P. F. C. M. and B. J, T. L. and H. B. Tirén J, M. M. S. L. T. A. and S. M. A. Huff M A, J. J. H, S. O. and G. P, M. Y. M. Y. W. Y. M. H. and S. K. Manz A, G. M. L. and S. S. D. Young A M, P. M. and M. J. Gadgil P N, van der S. B. H. and de R. N. F. Gass V, B. P. C. and F. J. H. J. van de Pol F C M, S. N. R. and N. A, T. N. R. E. M. and F. J. H. J. Lammerink T S J, I. D. J. and T. H. A. C, K. W. H. and P. J. M. Park S, Z. M. J, R. M. B. F. R. A. and S. H. Zengerle R, P. E. L. and R. H. V, H. H. M. W. and W. F. Vollmer J, H. J. and B.

H. G. and liquid flow in small channels Pfahler J, A. E. B. and B. K. S, S. J. B, K. B. M. P. A. P. and H. R. E. Cho Y H, B. J. and G. P, B. R. F. and W. R. O. Choi S B, H. J. B. H. and Z. J. Pfahler J, K. G. and N. B. Stemme G, T. M. A. and S. N. D. Ariman T, M. H. and C. J. E, van de P. F. C. M. and B. S. van Lintel H T G, S. J. G, H. M. A. L. T. A. and S. M. A. Mettner M S, G. T. M. J. M. M. T. H. P. and W. M. Döring C, S. L, O. H. Y. I. and Y. R. Miyake R, L. T. S. J. E. M. and F. J. H. J. Miyake R, Z. M. J. and A. J. A, F. T. R. J. and B. U. Ohnstein T, J. J. H, K. H. and T. A. Yanagisawa K, S. K. and T. S. Shikida M, W. D. G. J. E. M. and F. J. H. J. van de Pol F C M, R. A. and S. H. Zengerle R, S. L. and H. B, E. M. and M. T. Shoji S, S. S. and E. M. Nakagawa S, G. J. R. and S. M. A. Huff M A, T. L. T. J. and H. B. Lindberg U, E. M, van L. H. T. G. E. M. and F. J. H. J. van de Pol F C M, van der S. B. de R. N. and E. M. Shoji S, K. P. and L. R. Bouwstra S, B. R. W. and C. S. D. Schmidt R L, H. M. A. and S. M. A, S. S. and N. A. Esashi M, E. M. van der S. B. and de R. N. Shoji S, S. W. and S. B, H. B. M. G. S. H. T. U. and W. W. Bosch D, C. L. P. K. E. M. J. and B. J. Pourahmadi F, van de P. F. C. M. and B. S. van Lintel H T C, van den B. A. J. S. de R. N. F. and G. A. A. van der Schoot B H, van der S. B. H. J. S. and de R. N. F. Gass V, E. M. and F. J. H. J. Lammerink T S J, van der S. B. H. J. S. and de R. N. F. Gass V, T. T. and P. D. L. Judy J W, B. P. M. W. and S. W. K. Rapp R, S. E. and S. G, S. E. and S. G, R. A. and S. H, P. A. H. K. A. and S. H. Richter A, P. A. H. K. A. and S. H. Richter A, H. K. A. P. A. and S. H. Richter A, T. L. S. M. M. and L. J. H. Bart S F, S. H. and P. A. Richter A, F. J. C. V. E. H. D. J. L. H. and W. H. M. Manz A, H. D. J. F. J. C. V. E. L. and W. H. M. Manz A, W. R. M. and H. R. T. Moroney R M, K. T. and A. M. Miyazaki S, B. J. and R. W. Petersen K E, E. S. M. T. and C. S. Esashi M, J. R. G. and H. R. E, S. J. P. and V. W. Huijsing J H, S. G. N, van O. B. W. and H. J. H, S. G, T. Y.-C. and M. R. S, L. R. T. H. A. C. and E. M. Bouwstra S, L. R. and B. H. Moser D, E. M, D. B. J. M. R. F. R. V. O. B. W. and H. J. H. Bosman A, van O. B. W, H. R. T. S. S. D. and H. J. H. Schmidt M A, S. M. A, S. J. and S. M. A. N Kay-Yip, S. O. L. N. G. L. O. and S. H. Branebjerg J, Y. C. and S. H, H. R. M. T. B. W. and W. B. Fuhr G, C. S. T. and W. K. D, L. H. and W. H. M. Graber N, G. W. and M. B. Schelter W, S. S. and E. M, van der S. B. and B. P, van der S. B. H. C. F. and B. P. Olthuis W, H. S. et al, N. S. and E. M. Shoji S, van den V. H. H. and de R. N. F. van der Schoot B H, J. S. van den B. A. and de R. N. F. van der Schoot B H, M. A. W. H. M. van der S. B. and de R. N. F. Verpoorte E, M. A. L. H. and W. H. M. Fettinger J C, J. S. van den B. A. and de R. N. F. van der Schoot B H, H. D. J. V. E. and W. H. M. Manz A, G. P. G. and M. A. Harrison D J, M. A. V. E. de R. N. F. and W. H. M. Burggraf N, F. Z. S. K. and F. K. Harrison D J, M. A. and W. H. M. Effenhauser C S, V. E. E. C. S. B. N. R. D. E. H. D. J. and W. H. M. Manz A, M. A. and G. P. G. Harrison D J, S. K. M. A. and F. Z. Harrison D J, B. P. P. and A. J. B. Zdeblick M J, W. J. M. P. M. and P. P. A. Hu F Q, W. S. W. and W. R. M. Martin B A, T. Y. P. K. and H. C. Liu J, S. G. K. G. and P. K. Stenberg M, and H. W. F. and B. J. A, "Microfluidics-a review," *J. Micromechanics Microengineering*, vol. 3, no. 4, pp. 168–182, Dec. 1993.

[45] I. U. Khan, C. A. Serra, N. Anton, and T. Vandamme, "Microfluidics: A focus on improved cancer targeted drug delivery systems," *Journal of Controlled Release*, vol. 172, no. 3. pp. 1065–1074, 2013.

[46] K. Sato, N. Sasaki, H. A. Svahn, and K. Sato, “Microfluidics for nano-pathophysiology,” *Advanced Drug Delivery Reviews*, vol. 74. pp. 115–121, 2014.

[47] L. Y. Wu, D. Di Carlo, and L. P. Lee, “Microfluidic self-assembly of tumor spheroids for anticancer drug discovery,” *Biomed. Microdevices*, vol. 10, no. 2, pp. 197–202, 2008.

[48] S. N. Bhatia and D. E. Ingber, “Microfluidic organs-on-chips,” *Nature Biotechnology*, vol. 32, no. 8. pp. 760–772, 2014.

[49] P. M. van Midwoud, E. Verpoorte, and G. M. M. Groothuis, “Microfluidic devices for in vitro studies on liver drug metabolism and toxicity.,” *Integr. Biol. (Camb).*, vol. 3, no. 5, pp. 509–521, 2011.

[50] J. de Jong, R. G. H. Lammertink, and M. Wessling, “Membranes and microfluidics: a review,” *Lab Chip*, vol. 6, no. 9, p. 1125, 2006.

[51] B. Ziaie, A. Baldi, M. Lei, Y. Gu, and R. A. Siegel, “Hard and soft micromachining for BioMEMS: review of techniques and examples of applications in microfluidics and drug delivery,” *Adv. Drug Deliv. Rev.*, vol. 56, no. 2, pp. 145–172, 2004.

[52] J. Godin, C. H. Chen, S. H. Cho, W. Qiao, F. Tsai, and Y. H. Lo, “Microfluidics and photonics for bio-System-on-a-Chip: A review of advancements in technology towards a microfluidic flow cytometry chip,” *Journal of Biophotonics*, vol. 1, no. 5. pp. 355–376, 2008.

[53] M. Wörner, “Numerical modeling of multiphase flows in microfluidics and micro process engineering: a review of methods and applications,” *Microfluid. Nanofluidics*, vol. 12, no. 6, pp. 841–886, May 2012.

[54] Y. K. Suh and S. Kang, “A review on mixing in microfluidics,” *Micromachines*, vol. 1, no. 3. pp. 82–111, 2010.

[55] Y. Zheng, J. Chen, M. Craven, N. W. Choi, S. Totorica, A. Diaz-Santana, P. Kermani, B. Hempstead, C. Fischbach-Teschl, J. A. Lopez, and A. D. Stroock, “In vitro microvessels for the study of angiogenesis and thrombosis,” *Proc. Natl. Acad. Sci.*, vol. 109, no. 24, pp. 9342–9347, 2012.

[56] A. Thomas, S. Wang, S. Sohrabi, C. Orr, R. He, W. Shi, and Y. Liu, “Characterization of vascular permeability using a biomimetic microfluidic blood vessel model,” *Biomicrofluidics*, vol. 11, no. 2, 2017.

[57] C. G. Uhl, V. R. Muzykantov, and Y. Liu, “Biomimetic microfluidic platform for the quantification of transient endothelial monolayer permeability and therapeutic transport under mimicked cancerous conditions,” *Biomicrofluidics*, vol. 12, no. 1, 2018.

[58] A. Thomas, H. Daniel Ou-Yang, L. Lowe-Krentz, V. R. Muzykantov, and Y. Liu, “Biomimetic channel modeling local vascular dynamics of pro-inflammatory endothelial changes,” *Biomicrofluidics*, vol. 10, no. 1, 2016.

[59] Y. Tang, F. Soroush, J. B. Sheffield, B. Wang, B. Prabhakarpandian, and M. F. Kiani, “A Biomimetic Microfluidic Tumor Microenvironment Platform Mimicking the EPR Effect for Rapid Screening of Drug Delivery Systems,” *Sci. Rep.*, vol. 7, no. 1, p. 9359, 2017.

[60] Z. Dereli-Korkut, H. D. Akaydin, A. H. R. Ahmed, X. Jiang, and S. Wang, “Three dimensional microfluidic cell arrays for ex vivo drug screening with mimicked vascular flow,” *Anal. Chem.*, vol. 86, no. 6, pp. 2997–3004, 2014.

[61] W. Siyan, Y. Feng, Z. Lichuan, W. Jiarui, W. Yingyan, J. Li, L. Bingcheng, and W. Qi, “Application of microfluidic gradient chip in the analysis of lung cancer chemotherapy resistance,” *J. Pharm. Biomed. Anal.*, vol. 49, no. 3, pp. 806–810, 2009.

[62] T. J. Yeatman, “The future of clinical cancer management: one tumor, one chip,” *Am Surg*, vol. 69, no. 1, pp. 41–44, 2003.

[63] A. Y. Hsiao, Y. suke Torisawa, Y. C. Tung, S. Sud, R. S. Taichman, K. J. Pienta, and S. Takayama, “Microfluidic system for formation of PC-3 prostate cancer co-culture spheroids,” *Biomaterials*, vol. 30, no. 16, pp. 3020–3027, 2009.

[64] L. Zhao, Z. Wang, S. Fan, Q. Meng, B. Li, S. Shao, and Q. Wang, “Chemotherapy resistance research of lung cancer based on micro-fluidic chip system with flow medium,” *Biomed. Microdevices*, vol. 12, no. 2, pp. 325–332, 2010.

[65] D. Wlodkowic and J. M. Cooper, “Tumors on chips: Oncology meets microfluidics,” *Current Opinion in Chemical Biology*, vol. 14, no. 5. pp. 556–567, 2010.

[66] J. M. Prot and E. Leclerc, “The current status of alternatives to animal testing and predictive toxicology methods using liver microfluidic biochips,” *Ann. Biomed. Eng.*, vol. 40, no. 6, pp. 1228–1243, 2012.

[67] R. Baudoin, A. Corlu, L. Griscom, C. Legallais, and E. Leclerc, “Trends in the development of microfluidic cell biochips for in vitro hepatotoxicity,” *Toxicology in Vitro*, vol. 21, no. 4. pp. 535–544, 2007.

[68] Y.-C. Toh, T. C. Lim, D. Tai, G. Xiao, D. van Noort, and H. Yu, “A microfluidic 3D hepatocyte chip for drug toxicity testing,” *Lab Chip*, vol. 9, no. 14, p. 2026, 2009.

[69] P. M. van Midwoud, M. T. Merema, E. Verpoorte, and G. M. M. Groothuis, “A microfluidic approach for in vitro assessment of interorgan interactions in drug metabolism using intestinal and liver slices,” *Lab Chip*, vol. 10, no. 20, p. 2778, 2010.

[70] S. R. Khetani and S. N. Bhatia, “Microscale culture of human liver cells for drug development.,” *Nat. Biotechnol.*, vol. 26, no. 1, pp. 120–6, 2008.

[71] H. Tavana, P. Zamankhan, P. J. Christensen, J. B. Grotberg, and S. Takayama, “Epithelium damage and protection during reopening of occluded airways in a physiologic microfluidic pulmonary airway model,” *Biomed. Microdevices*, vol. 13, no. 4, pp. 731–742, 2011.

[72] A. J. Bitonti and J. A. Dumont, “Pulmonary administration of therapeutic proteins using an immunoglobulin transport pathway,” *Advanced Drug Delivery Reviews*, vol. 58, no. 9–10. pp. 1106–1118, 2006.

[73] J. S. Patton, “Mechanisms of macromolecule absorption by the lungs,” *Advanced Drug Delivery Reviews*, vol. 19, no. 1. pp. 3–36, 1996.

[74] N. Doshi, B. Prabhakarpandian, A. Rea-Ramsey, K. Pant, S. Sundaram, and S. Mitragotri, “Flow and adhesion of drug carriers in blood vessels depend on their shape: A study using model synthetic microvascular networks,” *J. Control. Release*, vol. 146, no. 2, pp. 196–200, 2010.

[75] B. Prabhakarpandian, M.-C. Shen, J. B. Nichols, I. R. Mills, M. Sidoryk-Wegrzynowicz, M. Aschner, and K. Pant, “SyM-BBB: a microfluidic blood brain barrier model,” *Lab Chip*, vol. 13, no. 6, p. 1093, 2013.

[76] N. J. Abbott and I. A. Romero, “Transporting therapeutics across the blood-brain barrier,” *Molecular Medicine Today*, vol. 2, no. 3. pp. 106–113, 1996.
[77] R. Gabathuler, “Approaches to transport therapeutic drugs across the blood-brain barrier to treat brain diseases,” *Neurobiology of Disease*, vol. 37, no. 1. pp. 48–57, 2010.
[78] H. Maeda, J. Wu, T. Sawa, Y. Matsumura, and K. Hori, “Tumor vascular permeability and the EPR effect in macromolecular therapeutics: A review,” *Journal of Controlled Release*, vol. 65, no. 1–2. pp. 271–284, 2000.
[79] R. T. Tong, Y. Boucher, S. V. Kozin, F. Winkler, D. J. Hicklin, and R. K. Jain, “Vascular normalization by vascular endothelial growth factor receptor 2 blockade induces a pressure gradient across the vasculature and improves drug penetration in tumors,” *Cancer Res.*, vol. 64, no. 11, pp. 3731–3736, 2004.
[80] C. Luni, E. Serena, and N. Elvassore, “Human-on-chip for therapy development and fundamental science,” *Curr. Opin. Biotechnol.*, vol. 25, pp. 45–50, 2014.
[81] D. Huh, Y. Torisawa, G. A. Hamilton, H. J. Kim, and D. E. Ingber, “Microengineered physiological biomimicry: Organs-on-Chips,” *Lab Chip*, vol. 12, no. 12, p. 2156, 2012.
[82] D. Huh, G. A. Hamilton, and D. E. Ingber, “From 3D cell culture to organs-on-chips,” *Trends in Cell Biology*, vol. 21, no. 12. pp. 745–754, 2011.
[83] S. N. Bhatia and D. E. Ingber, “Microfluidic organs-on-chips,” *Nat. Biotechnol.*, vol. 32, no. 8, pp. 760–772, 2014.
[84] D. Huh, B. D. Matthews, A. Mammoto, M. Montoya-Zavala, H. Y. Hsin, and D. E. Ingber, “Reconstituting Organ-Level Lung Functions on a Chip,” *Science (80-.).*, vol. 328, no. 5986, pp. 1662–1668, 2010.
[85] D. Huh, H. J. Kim, J. P. Fraser, D. E. Shea, M. Khan, A. Bahinski, G. A. Hamilton, and D. E. Ingber, “Microfabrication of human organs-on-chips,” *Nat. Protoc.*, vol. 8, no. 11, pp. 2135–2157, 2013.
[86] R. K. Jain, “Delivery of novel therapeutic agents in tumors: Physiological barriers and strategies,” *J. Natl. Cancer Inst.*, vol. 81, no. 8, pp. 570–576, 1989.
[87] L. Gu and D. J. Mooney, “Biomaterials and emerging anticancer therapeutics: engineering the microenvironment,” *Nat. Rev. Cancer*, vol. 16, no. 1, pp. 56–66, 2015.
[88] S. M. Ong, C. Zhang, Y. C. Toh, S. H. Kim, H. L. Foo, C. H. Tan, D. van Noort, S. Park, and H. Yu, “A gel-free 3D microfluidic cell culture system,” *Biomaterials*, vol. 29, no. 22, pp. 3237–3244, 2008.
[89] E. Jedrych, Z. Pawlicka, M. Chudy, A. Dybko, and Z. Brzozka, “Evaluation of photodynamic therapy (PDT) procedures using microfluidic system,” *Anal. Chim. Acta*, vol. 683, no. 2, pp. 149–155, 2011.
[90] R. Fisher, L. Pusztai, and C. Swanton, “Cancer heterogeneity: Implications for targeted therapeutics,” *Nature*, vol. 509, no. 7502 SUPPL. pp. 479–485, 2014.
[91] D. Ricklin and J. D. Lambris, “Complement-targeted therapeutics,” *Nature Biotechnology*, vol. 25, no. 11. pp. 1265–1275, 2007.
[92] J. V Jokerst, T. Lobovkina, R. N. Zare, and S. S. Gambhir, “Nanoparticle PEGylation for imaging and therapy,” *Nanomedicine*, vol. 6, no. 4, pp. 715–728, 2011.
[93] P. Milla, F. Dosio, and L. Cattel, “PEGylation of Proteins and Liposomes: a

Powerful and Flexible Strategy to Improve the Drug Delivery," *Curr. Drug Metab.*, vol. 13, no. 1, pp. 105–119, 2012.

[94] J. Milton Harris and R. B. Chess, "Effect of pegylation on pharmaceuticals," *Nature Reviews Drug Discovery*, vol. 2, no. 3. pp. 214–221, 2003.

[95] H. Maeda, T. Sawa, and T. Konno, "Mechanism of tumor-targeted delivery of macromolecular drugs, including the EPR effect in solid tumor and clinical overview of the prototype polymeric drug SMANCS," in *Journal of Controlled Release*, 2001, vol. 74, no. 1–3, pp. 47–61.

[96] P. M. Valencia, O. C. Farokhzad, R. Karnik, and R. Langer, "Microfluidic technologies for accelerating the clinical translation of nanoparticles," *Nat. Nanotechnol.*, vol. 7, no. 10, pp. 623–629, 2012.

[97] P. S. Dittrich and A. Manz, "Lab-on-a-chip: Microfluidics in drug discovery," *Nature Reviews Drug Discovery*, vol. 5, no. 3. pp. 210–218, 2006.

[98] C. Chen, J. Skog, C.-H. Hsu, R. T. Lessard, L. Balaj, T. Wurdinger, B. S. Carter, X. O. Breakefield, M. Toner, and D. Irimia, "Microfluidic isolation and transcriptome analysis of serum microvesicles," *Lab Chip*, vol. 10, no. 4, pp. 505–511, 2010.

[99] A. Aravind, S. H. Varghese, S. Veeranarayanan, A. Mathew, Y. Nagaoka, S. Iwai, T. Fukuda, T. Hasumura, Y. Yoshida, T. Maekawa, and D. S. Kumar, "Aptamer-labeled PLGA nanoparticles for targeting cancer cells," *Cancer Nanotechnol.*, vol. 3, no. 1–6, pp. 1–12, 2012.

[100] P. Kocbek, N. Obermajer, M. Cegnar, J. Kos, and J. Kristl, "Targeting cancer cells using PLGA nanoparticles surface modified with monoclonal antibody," *J. Control. Release*, vol. 120, no. 1–2, pp. 18–26, 2007.

[101] T. J. Yoon, K. N. Yu, E. Kim, J. S. Kim, B. G. Kim, S. H. Yun, B. H. Sohn, M. H. Cho, J. K. Lee, and S. B. Park, "Specific targeting, cell sorting, and bioimaging with smart magnetic silica core-shell nanomaterials," *Small*, vol. 2, no. 2, pp. 209–215, 2006.

[102] L. Brannon-Peppas and J. O. Blanchette, "Nanoparticle and targeted systems for cancer therapy," *Advanced Drug Delivery Reviews*, vol. 64, no. SUPPL. pp. 206–212, 2012.

[103] R. P. Bagwe, L. R. Hilliard, and W. Tan, "Surface modification of silica nanoparticles to reduce aggregation and nonspecific binding," *Langmuir*, vol. 22, no. 9, pp. 4357–4362, 2006.

[104] T. Ishida, M. Ichihara, X. Y. Wang, K. Yamamoto, J. Kimura, E. Majima, and H. Kiwada, "Injection of PEGylated liposomes in rats elicits PEG-specific IgM, which is responsible for rapid elimination of a second dose of PEGylated liposomes," *J. Control. Release*, vol. 112, no. 1, pp. 15–25, 2006.

[105] T. A. Kelf, V. K. A. Sreenivasan, J. Sun, E. J. Kim, E. M. Goldys, and A. V. Zvyagin, "Non-specific cellular uptake of surface-functionalized quantum dots," *Nanotechnology*, vol. 21, no. 28, 2010.

[106] H. Xu, F. Yan, E. E. Monson, and R. Kopelman, "Room-temperature preparation and characterization of poly (ethylene glycol)-coated silica nanoparticles for biomedical applications.," *J. Biomed. Mater. Res. A*, vol. 66, no. 4, pp. 870–879, 2003.

[107] A. C. Templeton, W. P. Wuelfing, and R. W. Murray, "Monolayer-protected

cluster molecules," *Acc. Chem. Res.*, vol. 33, no. 1, pp. 27–36, 2000.

[108] M. Zheng, F. Davidson, and X. Huang, "Ethylene glycol monolayer protected nanoparticles for eliminating nonspecific binding with biological molecules," *J. Am. Chem. Soc.*, vol. 125, no. 26, pp. 7790–7791, 2003.

[109] Y. Cheng, A. C. Samia, J. D. Meyers, I. Panagopoulos, B. Fei, and C. Burda, "Highly efficient drug delivery with gold nanoparticle vectors for in vivo photodynamic therapy of cancer," *J. Am. Chem. Soc.*, vol. 130, no. 32, pp. 10643–10647, 2008.

[110] X. Gao, Y. Cui, R. M. Levenson, L. W. K. Chung, and S. Nie, "In vivo cancer targeting and imaging with semiconductor quantum dots," *Nat. Biotechnol.*, vol. 22, no. 8, pp. 969–976, 2004.

[111] W. S. Cho, M. Cho, J. Jeong, M. Choi, H. Y. Cho, B. S. Han, S. H. Kim, H. O. Kim, Y. T. Lim, B. H. Chung, and J. Jeong, "Acute toxicity and pharmacokinetics of 13??nm-sized PEG-coated gold nanoparticles," *Toxicol. Appl. Pharmacol.*, vol. 236, no. 1, pp. 16–24, 2009.

[112] Y. Son, "Determination of shear viscosity and shear rate from pressure drop and flow rate relationship in a rectangular channel," *Polymer (Guildf).*, vol. 48, no. 2, pp. 632–637, 2007.

[113] P. Nigro, J.-I. Abe, and B. C. Berk, "Flow shear stress and atherosclerosis: a matter of site specificity.," *Antioxid. Redox Signal.*, vol. 15, no. 5, pp. 1405–14, 2011.

[114] T. Nagaoka and A. Yoshida, "Noninvasive evaluation of wall shear stress on retinal microcirculation in humans," *Investig. Ophthalmol. Vis. Sci.*, vol. 47, no. 3, pp. 1113–1119, 2006.

[115] A. Thomas, J. Tan, and Y. Liu, "Characterization of nanoparticle delivery in microcirculation using a microfluidic device," *Microvasc. Res.*, vol. 94, pp. 17–27, 2014.

[116] Q. Xu, N. J. Boylan, S. Cai, B. Miao, H. Patel, and J. Hanes, "Scalable method to produce biodegradable nanoparticles that rapidly penetrate human mucus," *J. Control. Release*, vol. 170, no. 2, pp. 279–286, 2013.

[117] T. Scientific, "Polyethylene Glycol (PEG) and Pegylation of Proteins," 2016. [Online]. Available: https://www.thermofisher.com/us/en/home/life-science/protein-biology/protein-biology-learning-center/protein-biology-resource-library/pierce-protein-methods/polyethylene-glycol-peg-pegylation-proteins.html.

[118] E. C. Jensen, "Quantitative Analysis of Histological Staining and Fluorescence Using ImageJ," *Anatomical Record*, vol. 296, no. 3. pp. 378–381, 2013.

[119] M. Lundqvist, J. Stigler, G. Elia, I. Lynch, T. Cedervall, and K. A. Dawson, "Nanoparticle size and surface properties determine the protein corona with possible implications for biological impacts.," *Proc. Natl. Acad. Sci. U. S. A.*, vol. 105, no. 38, pp. 14265–70, 2008.

[120] S. P. Samuel, N. Jain, F. O'Dowd, T. Paul, D. Kashanin, V. A. Gerard, Y. K. Gun'ko, A. Prina-Mello, and Y. Volkov, "Multifactorial determinants that govern nanoparticle uptake by human endothelial cells under flow," *Int. J. Nanomedicine*, vol. 7, pp. 2943–2956, 2012.

[121] J. Davda and V. Labhasetwar, "Characterization of nanoparticle uptake by endothelial cells," *Int. J. Pharm.*, vol. 233, no. 1–2, pp. 51–59, 2002.

[122] P. B. van Wachem, C. M. Vreriks, T. Beugeling, J. Feijen, A. Bantjes, J. P.

Detmers, and W. G. van Aken, "The influence of protein adsorption on interactions of cultured human endothelial cells with polymers," *J. Biomed. Mater. Res.*, vol. 21, no. 6, pp. 701–718, 1987.

[123] M. S. Ehrenberg, A. E. Friedman, J. N. Finkelstein, G. Oberdörster, and J. L. McGrath, "The influence of protein adsorption on nanoparticle association with cultured endothelial cells," *Biomaterials*, vol. 30, no. 4, pp. 603–610, 2009.

[124] C. G. Uhl, Y. Gao, S. Zhou, and Y. Liu, "The shape effect on polymer nanoparticle transport in a blood vessel," *RSC Adv.*, vol. 8, no. 15, pp. 8089–8100, 2018.

[125] B. P. Eliceiri, R. Paul, P. L. Schwartzberg, J. D. Hood, J. Leng, and D. a Cheresh, "Selective requirement for Src kinases during VEGF-induced angiogenesis and vascular permeability.," *Mol. Cell*, vol. 4, no. 6, pp. 915–924, 1999.

[126] S. Shresta, K. L. Sharar, D. M. Prigozhin, P. R. Beatty, and E. Harris, "Murine Model for Dengue Virus-Induced Lethal Disease with Increased Vascular Permeability," *J. Virol.*, vol. 80, no. 20, pp. 10208–10217, 2006.

[127] S. M. Weis and D. A. Cheresh, "Pathophysiological consequences of VEGF-induced vascular permeability.," *Nature*, vol. 437, no. 7058, pp. 497–504, 2005.

[128] D. R. Senger, S. J. Galli, A. M. Dvorak, C. A. Perruzzi, V. S. Harvey, and H. F. Dvorak, "Tumor cells secrete a vascular permeability factor that promotes accumulation of ascites fluid.," *Science*, vol. 219, no. 4587, pp. 983–5, 1983.

[129] H. Maeda, J. Fang, T. Inutsuka, and Y. Kitamoto, "Vascular permeability enhancement in solid tumor: Various factors, mechanisms involved and its implications," in *International Immunopharmacology*, 2003, vol. 3, no. 3, pp. 319–328.

[130] A. K. Iyer, G. Khaled, J. Fang, and H. Maeda, "Exploiting the enhanced permeability and retention effect for tumor targeting," *Drug Discovery Today*, vol. 11, no. 17–18. pp. 812–818, 2006.

[131] R. K. Jain, "Normalization of tumor vasculature: an emerging concept in antiangiogenic therapy.," *Science (80-.).*, vol. 307, no. 5706, pp. 58–62, 2005.

[132] V. Torchilin, "Tumor delivery of macromolecular drugs based on the EPR effect," *Advanced Drug Delivery Reviews*, vol. 63, no. 3. pp. 131–135, 2011.

[133] J. Fang, H. Nakamura, and H. Maeda, "The EPR effect: Unique features of tumor blood vessels for drug delivery, factors involved, and limitations and augmentation of the effect," *Advanced Drug Delivery Reviews*, vol. 63, no. 3. pp. 136–151, 2011.

[134] H. Maeda, G. Y. Bharate, and J. Daruwalla, "Polymeric drugs for efficient tumor-targeted drug delivery based on EPR-effect," *European Journal of Pharmaceutics and Biopharmaceutics*, vol. 71, no. 3. pp. 409–419, 2009.

[135] R. Singh and J. W. Lillard, "Nanoparticle-based targeted drug delivery," *Experimental and Molecular Pathology*, vol. 86, no. 3. pp. 215–223, 2009.

[136] Y. H. Bae and K. Park, "Targeted drug delivery to tumors: Myths, reality and possibility," *Journal of Controlled Release*, vol. 153, no. 3. pp. 198–205, 2011.

[137] J. M. Brown and A. J. Giaccia, "The unique physiology of solid tumors: Opportunities (and problems) for cancer therapy," *Cancer Res.*, vol. 58, no. 7, pp. 1408–1416, 1998.

[138] S. K. Sriraman, B. Aryasomayajula, and V. P. Torchilin, "Barriers to drug delivery in solid tumors.," *Tissue barriers*, vol. 2, no. July, p. e29528, 2014.

[139] T. T. Batchelor, A. G. Sorensen, E. di Tomaso, W. T. Zhang, D. G. G. Duda, K. S.

Cohen, K. R. Kozak, D. P. Cahill, P. J. Chen, M. Zhu, M. Ancukiewicz, M. M. Mrugala, S. Plotkin, J. Drappatz, D. N. Louis, P. Ivy, D. T. T. Scadden, T. Benner, J. S. Loeffler, P. Y. Wen, and R. K. Jain, "AZD2171, a Pan-VEGF Receptor Tyrosine Kinase Inhibitor, Normalizes Tumor Vasculature and Alleviates Edema in Glioblastoma Patients," *Cancer Cell*, vol. 11, no. 1, pp. 83–95, 2007.

[140] M. R. Mancuso, R. Davis, S. M. Norberg, S. O'Brien, B. Sennino, T. Nakahara, V. J. Yao, T. Inai, P. Brooks, B. Freimark, D. R. Shalinsky, D. D. Hu-Lowe, and D. M. McDonald, "Rapid vascular regrowth in tumors after reversal of VEGF inhibition," *J. Clin. Invest.*, vol. 116, no. 10, pp. 2610–2621, 2006.

[141] K. J. Heyeraas and E. Berggreen, "Interstitial fluid pressure in normal and inflamed pulp.," *Critical reviews in oral biology and medicine : an official publication of the American Association of Oral Biologists*, vol. 10, no. 3. pp. 328–36, 1999.

[142] C.-H. Heldin, K. Rubin, K. Pietras, and A. Ostman, "High interstitial fluid pressure - an obstacle in cancer therapy.," *Nat. Rev. Cancer*, vol. 4, no. 10, pp. 806–13, 2004.

[143] C. Andrea Zanella LAUREANDO and A. Biral, "MICROFLUIDIC NETWORKING: MODELLING AND ANALYSIS," 2012.

[144] W. Rasband, "ImageJ," *U. S. Natl. Institutes Heal. Bethesda, Maryland, USA*, p. //imagej.nih.gov/ij/, 2017.

[145] H. F. Dvorak, "Vascular permeability factor/vascular endothelial growth factor: A critical cytokine in tumor angiogenesis and a potential target for diagnosis and therapy," *Journal of Clinical Oncology*, vol. 20, no. 21. pp. 4368–4380, 2002.

[146] D. R. Senger, L. Van De Water, L. F. Brown, J. A. Nagy, K. T. Yeo, T. K. Yeo, B. Berse, R. W. Jackman, A. M. Dvorak, and H. F. Dvorak, "Vascular permeability factor (VPF, VEGF) in tumor biology," *Cancer Metastasis Rev.*, vol. 12, no. 3–4, pp. 303–324, 1993.

[147] J. A. Nagy, A. M. Dvorak, and H. F. Dvorak, "Vascular hyperpermeability, angiogenesis, and stroma generation," *Cold Spring Harb Perspect Med*, vol. 2, no. 2, p. a006544, 2012.

[148] R. Green, Windhage.Ee, and G. Giebisch, "Protein Oncotic Pressure Effects on Proximal Tubular Fluid Movement in Rat," *Am. J. Physiol.*, vol. 226, no. 2, pp. 265–276, 1974.

[149] M. Stohrer, Y. Boucher, M. Stangassinger, and R. K. Jain, "Oncotic pressure in solid tumors is elevated," *Cancer Res.*, vol. 60, no. 15, pp. 4251–4255, 2000.

[150] E. S. Marie, R. K. Jain, and E. M. Sevick, "Effect of Red Blood Cell Rigidity on Tumor Blood Flow: Increase in Viscous Resistance during Hyperglycemia," *Cancer Res.*, vol. 51, no. 10, pp. 2727–2730, 1991.

[151] R. P. McCall and M. Sher, "The Physics of the Human Body.," *Am. J. Phys.*, vol. 80, no. 2, p. 174, 2012.

[152] K. H. Jensen, A. X. C. N. Valente, and H. A. Stone, "Flow rate through microfilters: Influence of the pore size distribution, hydrodynamic interactions, wall slip, and inertia," *Phys. Fluids*, vol. 26, no. 5, p. 52004, 2014.

[153] R. K. Jain, "Determinants of Tumor Blood Flow: A Review," *Cancer Res.*, vol. 48, no. 10, pp. 2641–2658, 1988.

[154] M. W. Radomski, R. M. Palmer, and S. Moncada, "Endogenous nitric oxide

inhibits human platelet adhesion to vascular endothelium.," *Lancet*, vol. 2, no. 8567, pp. 1057–8, 1987.

[155] R. J. Ober, C. G. Radu, V. Ghetie, and E. S. Ward, "Differences in promiscuity for antibody-FcRn interactions across species: implications for therapeutic antibodies.," *Int. Immunol.*, vol. 13, no. 12, pp. 1551–1559, 2001.

[156] J. Folkman, C. C. Haudenschild, and B. R. Zetter, "Long-term culture of capillary endothelial cells," *Proc Natl Acad Sci U S A*, vol. 76, no. 10, pp. 5217–5221, 1979.

[157] F. J. Byfield, R. K. Reen, T. P. Shentu, I. Levitan, and K. J. Gooch, "Endothelial actin and cell stiffness is modulated by substrate stiffness in 2D and 3D," *J. Biomech.*, vol. 42, no. 8, pp. 1114–1119, 2009.

[158] F. Pampaloni, E. G. Reynaud, and E. H. K. Stelzer, "The third dimension bridges the gap between cell culture and live tissue," *Nat. Rev. Mol. Cell Biol.*, vol. 8, no. 10, pp. 839–845, 2007.

[159] M. Muta, T. Yanagawa, Y. Sai, S. Saji, E. Suzuki, T. Aruga, K. Kuroi, G. Matsumoto, M. Toi, and E. Nakashima, "Effect of low-dose paclitaxel and docetaxel on endothelial progenitor cells," *Oncology*, vol. 77, no. 3–4, pp. 182–191, 2009.

[160] E. Pasquier, S. Honore, B. Pourroy, M. A. Jordan, M. Lehmann, C. Briand, and D. Braguer, "Antiangiogenic concentrations of paclitaxel induce an increase in microtubule dynamics in endothelial cells but not in cancer cells," *Cancer Res.*, vol. 65, no. 6, pp. 2433–2440, 2005.

[161] J. Folkman, "Angiogenesis and apoptosis," *Seminars in Cancer Biology*, vol. 13, no. 2. pp. 159–167, 2003.

[162] D. S. Grant, T. L. Williams, M. Zahaczewsky, and A. P. Dicker, "Comparison of antiangiogenic activities using paclitaxel (taxol) and docetaxel (taxotere)," *Int. J. Cancer*, vol. 104, no. 1, pp. 121–129, 2003.

[163] M. Sugihara-Seki and B. M. Fu, "Blood flow and permeability in microvessels," *Fluid Dynamics Research*, vol. 37, no. 1–2 SPEC. ISS. pp. 82–132, 2005.

[164] Y. Tang, F. Soroush, J. B. Sheffield, B. Wang, B. Prabhakarpandian, and M. F. Kiani, "A Biomimetic Microfluidic Tumor Microenvironment Platform Mimicking the EPR Effect for Rapid Screening of Drug Delivery Systems," *Sci. Rep.*, 2017.

[165] H. D. Bear, S. Anderson, A. Brown, R. Smith, E. P. Mamounas, B. Fisher, R. Margolese, H. Theoret, A. Soran, D. Lawrence Wickerham, and N. Wolmark, "The effect on tumor response of adding sequential preoperative docetaxel to preoperative doxorubicin and cyclophosphamide: Preliminary results from National Surgical Adjuvant Breast and Bowel Project Protocol B-27," *J. Clin. Oncol.*, vol. 21, no. 22, pp. 4165–4174, 2003.

[166] G. Maschek, N. Savaraj, W. Priebe, P. Braunschweiger, K. Hamilton, G. F. Tidmarsh, L. R. De Young, and T. J. Lampidis, "2-Deoxy-D-glucose Increases the Efficacy of Adriamycin and Paclitaxel in Human Osteosarcoma and Non-Small Cell Lung Cancers in Vivo," *Cancer Res.*, vol. 64, no. 1, pp. 31–34, 2004.

[167] J. Baselga, L. Norton, J. Albanell, Y. M. Kim, and J. Mendelsohn, "Recombinant humanized anti-HER2 antibody (herceptin(TM)) enhances the antitumor activity of paclitaxel and doxorubicin against HER2/neu overexpressing human breast cancer xenografts," *Cancer Res.*, vol. 58, no. 13, pp. 2825–2831, 1998.

[168] L. Hu, J. Hofmann, Y. Lu, G. B. Mills, and R. B. Jaffe, "Inhibition of

phosphatidylinositol 3???-kinase increases efficacy of paclitaxel in in vitro and in vivo ovarian cancer models," *Cancer Res.*, vol. 62, no. 4, pp. 1087–1092, 2002.
[169] F. Yuan, Y. Chen, M. Dellian, N. Safabakhsh, N. Ferrara, and R. K. Jain, "Time-dependent vascular regression and permeability changes in established human tumor xenografts induced by an anti-vascular endothelial growth factor/vascular permeability factor antibody.," *Proc. Natl. Acad. Sci. U. S. A.*, vol. 93, no. 25, pp. 14765–70, 1996.
[170] S. Goel, D. G. Duda, L. Xu, L. L. Munn, Y. Boucher, D. Fukumura, and R. K. Jain, "Normalization of the Vasculature for Treatment of Cancer and Other Diseases," *Physiol. Rev.*, vol. 91, no. 3, pp. 1071–1121, 2011.
[171] H. Walczak, R. E. Miller, K. Ariail, B. Gliniak, T. S. Griffith, M. Kubin, W. Chin, J. Jones, a Woodward, T. Le, C. Smith, P. Smolak, R. G. Goodwin, C. T. Rauch, J. C. Schuh, and D. H. Lynch, "Tumoricidal activity of tumor necrosis factor-related apoptosis-inducing ligand in vivo.," *Nat. Med.*, vol. 5, no. 2, pp. 157–163, 1999.
[172] J. P. Stevenson, M. Rosen, W. Sun, M. Gallagher, D. G. Haller, D. Vaughn, B. Giantonio, R. Zimmer, W. P. Petros, M. Stratford, D. Chaplin, S. L. Young, M. Schnall, and P. J. O'Dwyer, "Phase I trial of the antivascular agent combretastatin A4 phosphate on a 5-day schedule to patients with cancer: Magnetic resonance imaging evidence for altered tumor blood flow," *J. Clin. Oncol.*, vol. 21, no. 23, pp. 4428–4438, 2003.
[173] T. Fujiwara, E. a Grimm, T. Mukhopadhyay, W. W. Zhang, L. B. Owen-Schaub, and J. a Roth, "Induction of chemosensitivity in human lung cancer cells in vivo by adenovirus-mediated transfer of the wild-type p53 gene.," *Cancer Res.*, vol. 54, no. 9, pp. 2287–91, 1994.
[174] W. Stein, *The movement of molecules across cell membranes.* 2012.
[175] K. Simons and E. Ikonen, "Functional rafts in cell membranes.," *Nature*, vol. 387, no. 6633, pp. 569–72, 1997.
[176] G. Cevc and D. Gebauer, "Hydration-Driven Transport of Deformable Lipid Vesicles through Fine Pores and the Skin Barrier," *Biophys. J.*, vol. 84, no. 2, pp. 1010–1024, 2003.
[177] N. N. Alder and S. M. Theg, "Energetics of protein transport across biological membranes: A study of the thylakoid ΔpH-dependent/cpTat pathway," *Cell*, vol. 112, no. 2, pp. 231–242, 2003.
[178] M. A. Wilson and A. Pohorille, "Mechanism of unassisted ion transport across membrane bilayers," *J. Am. Chem. Soc.*, vol. 118, no. 28, pp. 6580–6587, 1996.
[179] K. Inoki, T. Zhu, and K.-L. L. Guan, "TSC2 mediates cellular energy response to control cell growth and survival.," *Cell*, vol. 115, no. 5, pp. 577–590, 2003.
[180] V. Müller, "Energy Conservation in Acetogenic Bacteria," *Applied and Environmental Microbiology*, vol. 69, no. 11. pp. 6345–6353, 2003.
[181] R. K. K. THAUER, K. Jungermann, and K. DECKER, "Energy conservation in chemotrophic anaerobic bacteria - ERRATUM," *Microbiol. Mol. Biol. Rev.*, vol. 41, pp. 100–180, 1977.
[182] P. Decuzzi and M. Ferrari, "Design maps for nanoparticles targeting the diseased microvasculature," *Biomaterials*, vol. 29, no. 3, pp. 377–384, 2008.
[183] S. M. Moghimi, A. C. Hunter, and T. L. Andresen, "Factors Controlling

Nanoparticle Pharmacokinetics: An Integrated Analysis and Perspective," *Annu. Rev. Pharmacol. Toxicol.*, vol. 52, no. 1, pp. 481–503, 2012.

[184] F. Gentile, C. Chiappini, D. Fine, R. C. Bhavane, M. S. Peluccio, M. M. C. Cheng, X. Liu, M. Ferrari, and P. Decuzzi, "The effect of shape on the margination dynamics of non-neutrally buoyant particles in two-dimensional shear flows," *J. Biomech.*, vol. 41, no. 10, pp. 2312–2318, 2008.

[185] P. Decuzzi, B. Godin, T. Tanaka, S. Y. Lee, C. Chiappini, X. Liu, and M. Ferrari, "Size and shape effects in the biodistribution of intravascularly injected particles," *J. Control. Release*, vol. 141, no. 3, pp. 320–327, 2010.

[186] R. Weissleder, K. Kelly, E. Y. Sun, T. Shtatland, and L. Josephson, "Cell-specific targeting of nanoparticles by multivalent attachment of small molecules.," *Nat. Biotechnol.*, vol. 23, no. 11, pp. 1418–1423, 2005.

[187] S. M. Moghimi, J. C. Murray, and A. C. Hunter, "Long-circulating and target specific nanoparticles: Theory to practice," *Pharmacol. Rev.*, vol. 53, no. 2, pp. 283–318, 2001.

[188] J. D. Hood, M. Bednarski, R. Frausto, S. Guccione, R. a Reisfeld, R. Xiang, and D. a Cheresh, "Tumor regression by targeted gene delivery to the neovasculature.," *Science*, vol. 296, no. 5577, pp. 2404–2407, 2002.

[189] Y. Geng, P. Dalhaimer, S. Cai, R. Tsai, M. Tewari, T. Minko, and D. E. Discher, "Shape effects of filaments versus spherical particles in flow and drug delivery," *Nat. Nanotechnol.*, vol. 2, no. 4, pp. 249–255, 2007.

[190] A. I. Prokhnevsky, V. V Peremyslov, A. J. Napuli, and V. V Dolja, "Interaction between long-distance transport factor and Hsp70-related movement protein of Beet yellows virus.," *J. Virol.*, vol. 76, no. 21, pp. 11003–11011, 2002.

[191] S. Santa Cruz, A. Roberts, D. Prior, S. Chapman, and K. Oparka, "Cell-to-cell and phloem-mediated transport of potato virus X. The role of virions," *Plant Cell*, vol. 10, no. 4, pp. 495–510, 1998.

[192] A. Albanese, P. S. Tang, and W. C. W. Chan, "The Effect of Nanoparticle Size, Shape, and Surface Chemistry on Biological Systems," *Annu. Rev. Biomed. Eng.*, vol. 14, no. 1, pp. 1–16, 2012.

[193] X. Huang, L. Li, T. Liu, N. Hao, H. Liu, D. Chen, and F. Tang, "The shape effect of mesoporous silica nanoparticles on biodistribution, clearance, and biocompatibility in vivo," in *ACS Nano*, 2011, vol. 5, no. 7, pp. 5390–5399.

[194] B. Ma, G. Zhang, J. Qin, and B. Lin, "Characterization of drug metabolites and cytotoxicity assay simultaneously using an integrated microfluidic device.," *Lab Chip*, vol. 9, no. 2, pp. 232–238, 2009.

[195] O. Mockers, D. Deroze, and J. Camps, "Cytotoxicity of orthodontic bands, brackets and archwires in vitro," *Dent. Mater.*, vol. 18, no. 4, pp. 311–317, 2002.

[196] R. S. Brown, P. Akhtar, J. Åkerman, L. Hampel, I. S. Kozin, L. A. Villerius, and H. J. C. Klamer, "Partition controlled delivery of hydrophobic substances in toxicity tests using poly(dimethylsiloxane) (PDMS) films," *Environ. Sci. Technol.*, vol. 35, no. 20, pp. 4097–4102, 2001.

[197] K. Ziolkowska, E. Jedrych, R. Kwapiszewski, J. Lopacinska, M. Skolimowski, and M. Chudy, "PDMS/glass microfluidic cell culture system for cytotoxicity tests and cells passage," *Sensors Actuators, B Chem.*, vol. 145, no. 1, pp. 533–542, 2010.

[198] J. M. Prot, A. Bunescu, B. Elena-Herrmann, C. Aninat, L. C. Snouber, L. Griscom,

F. Razan, F. Y. Bois, C. Legallais, C. Brochot, A. Corlu, M. E. Dumas, and E. Leclerc, “Predictive toxicology using systemic biology and liver microfluidic ‘on chip’ approaches: Application to acetaminophen injury,” *Toxicol. Appl. Pharmacol.*, vol. 259, no. 3, pp. 270–280, 2012.

[199] M. Gou, X. Zheng, K. Men, J. Zhang, B. Wang, L. Lv, X. Wang, Y. Zhao, F. Luo, L. Chen, X. Zhao, Y. Wei, and Z. Qian, “Self-assembled hydrophobic honokiol loaded MPEG-PCL diblock copolymer micelles,” *Pharm. Res.*, vol. 26, no. 9, pp. 2164–2173, 2009.

[200] T. Wang, X.-J. Jiang, Q.-Z. Tang, X.-Y. Li, T. Lin, D.-Q. Wu, X.-Z. Zhang, and E. Okello, “Bone marrow stem cells implantation with α-cyclodextrin/MPEG–PCL–MPEG hydrogel improves cardiac function after myocardial infarction,” *Acta Biomater.*, vol. 5, no. 8, pp. 2939–2944, 2009.

[201] K. Tanaka, T. Kanazawa, Y. Shibata, Y. Suda, T. Fukuda, Y. Takashima, and H. Okada, “Development of cell-penetrating peptide-modified MPEG-PCL diblock copolymeric nanoparticles for systemic gene delivery,” *Int. J. Pharm.*, vol. 396, no. 1–2, pp. 229–238, 2010.

[202] E. M. Sevick and R. K. Jain, “Microvascular Architecture in a Mammary Carcinoma: Branching Patterns and Vessel Dimensions,” *Cancer Res.*, vol. 51, no. 1, pp. 265–273, 1991.

[203] K. Fronek and B. W. Zweifach, “Microvascular pressure distribution in skeletal muscle and the effect of vasodilation.,” *Am. J. Physiol.*, vol. 228, no. 3, pp. 791–796, 1975.

[204] H. N. Mayrovitz and J. Roy, “Microvascular blood flow: evidence indicating a cubic dependence on arteriolar diameter,” *Am J Physiol*, vol. 245, no. 6, pp. H1031-8, 1983.

[205] D. Li, Z. Tang, Y. Gao, H. Sun, and S. Zhou, “A Bio-Inspired Rod-Shaped Nanoplatform for Strongly Infecting Tumor Cells and Enhancing the Delivery Efficiency of Anticancer Drugs,” *Adv. Funct. Mater.*, vol. 26, no. 1, pp. 66–79, 2016.

[206] L. Zeng, S. Balachandar, and P. Fischer, “Wall-induced forces on a rigid sphere at finite Reynolds number,” *J. Fluid Mech.*, vol. 536, pp. 1–25, 2005.

[207] J. P. Matas, J. F. Morris, and E. Guazzelli, “Lateral forces on a sphere,” *Oil Gas Sci. Technol.*, vol. 59, no. 1, pp. 59–70, 2004.

[208] M. P. Howard, A. Gautam, A. Z. Panagiotopoulos, and A. Nikoubashman, “Axial dispersion of Brownian colloids in microfluidic channels,” *Phys. Rev. Fluids*, vol. 1, no. 4, p. 044203, 2016.

[209] F. Takemura and J. Magnaudet, “The transverse force on clean and contaminated bubbles rising near a vertical wall at moderate Reynolds number,” *J. Fluid Mech.*, vol. 495, pp. 235–253, 2003.

[210] P. Vasseur and R. Cox, “The lateral migration of spherical particles sedimenting in a stagnant bounded fluid,” *J. Fluid Mech.*, vol. 80, no. 3, pp. 561–591, 1977.

[211] T. Chen, X. Guo, X. Liu, S. Shi, J. Wang, C. L. Shi, Z. Y. Qian, and S. B. Zhou, “A strategy in the design of micellar shape for cancer therapy,” *Adv. Healthc. Mater.*, vol. 1, no. 2, pp. 214–224, 2012.

[212] Y. Geng, P. Dalhaimer, S. Cai, R. Tsai, M. Tewari, T. Minko, and D. E. Discher, “Shape effects of filaments versus spherical particles in flow and drug delivery.,”

Nat. Nanotechnol., vol. 2, no. 4, pp. 249–55, 2007.

[213] A. J. Storm, C. Storm, J. Chen, H. Zandbergen, J. F. Joanny, and C. Dekker, “Fast DNA translocation through a solid-state nanopore,” *Nano Lett.*, vol. 5, no. 7, pp. 1193–1197, 2005.

[214] M. Wanunu, J. Sutin, B. McNally, A. Chow, and A. Meller, “DNA translocation governed by interactions with solid-state nanopores.,” *Biophys. J.*, vol. 95, no. 10, pp. 4716–25, 2008.

[215] A. J. Storm, J. H. Chen, H. W. Zandbergen, and C. Dekker, “Translocation of double-strand DNA through a silicon oxide nanopore,” *Phys. Rev. E - Stat. Nonlinear, Soft Matter Phys.*, vol. 71, no. 5, 2005.

[216] A. Meller, L. Nivon, and D. Branton, “Voltage-driven DNA translocations through a nanopore,” *Phys. Rev. Lett.*, vol. 86, no. 15, pp. 3435–3438, 2001.

[217] Y. Imamura, T. Mukohara, Y. Shimono, Y. Funakoshi, N. Chayahara, M. Toyoda, N. Kiyota, S. Takao, S. Kono, T. Nakatsura, and H. Minami, “Comparison of 2D- and 3D-culture models as drug-testing platforms in breast cancer,” *Oncol. Rep.*, vol. 33, no. 4, pp. 1837–1843, 2015.

[218] K. Stock, M. F. Estrada, S. Vidic, K. Gjerde, A. Rudisch, V. E. Santo, M. Barbier, S. Blom, S. C. Arundkar, I. Selvam, A. Osswald, Y. Stein, S. Gruenewald, C. Brito, W. Van Weerden, V. Rotter, E. Boghaert, M. Oren, W. Sommergruber, Y. Chong, R. De Hoogt, and R. Graeser, “Capturing tumor complexity in vitro: Comparative analysis of 2D and 3D tumor models for drug discovery,” *Sci. Rep.*, vol. 6, 2016.

[219] V. van Duinen, S. J. Trietsch, J. Joore, P. Vulto, and T. Hankemeier, “Microfluidic 3D cell culture: From tools to tissue models,” *Current Opinion in Biotechnology*, vol. 35. pp. 118–126, 2015.

[220] A. Y. Hsiao, Y. suke Torisawa, Y. C. Tung, S. Sud, R. S. Taichman, K. J. Pienta, and S. Takayama, “Microfluidic system for formation of PC-3 prostate cancer co-culture spheroids,” *Biomaterials*, vol. 30, no. 16, pp. 3020–3027, 2009.

[221] Y.-C. Toh, C. Zhang, J. Zhang, Y. M. Khong, S. Chang, V. D. Samper, D. van Noort, D. W. Hutmacher, and H. Yu, “A novel 3D mammalian cell perfusion-culture system in microfluidic channels,” *Lab Chip*, vol. 7, no. 3, p. 302, 2007.

[222] Y. Shin, S. Han, J. S. Jeon, K. Yamamoto, I. K. Zervantonakis, R. Sudo, R. D. Kamm, and S. Chung, “Microfluidic assay for simultaneous culture of multiple cell types on surfaces or within hydrogels,” *Nat. Protoc.*, vol. 7, no. 7, pp. 1247–1259, 2012.

[223] O. Costăchel, L. Fadei, and E. Badea, “Tumor cell suspension culture on non adhesive substratum,” *Z. Krebsforsch.*, vol. 72, no. 1, pp. 24–31, 1969.

[224] R. Z. Lin and H. Y. Chang, “Recent advances in three-dimensional multicellular spheroid culture for biomedical research,” *Biotechnology Journal*, vol. 3, no. 9–10. pp. 1172–1184, 2008.

[225] V. H. B. Ho, A. Barcza, R. Chen, K. H. Müller, N. J. Darton, and N. K. H. Slater, “The precise control of cell labelling with streptavidin paramagnetic particles,” *Biomaterials*, vol. 30, no. 33, pp. 6548–6555, 2009.

[226] T. G. Hammond and J. M. Hammond, “Optimized suspension culture: the rotating-wall vessel,” *Am. J. Physiol. Physiol.*, vol. 281, no. 1, pp. F12–F25, 2001.

[227] Z. Zhang, H. Wang, Q. Ding, Y. Xing, Z. Xu, C. Lu, D. Luo, L. Xu, W. Xia, C.

Zhou, and M. Shi, “Establishment of patient-derived tumor shpheroids for non-small cell lung cancer,” *PLoS One*, 2018.

[228] G. Vlachogiannis, S. Hedayat, A. Vatsiou, Y. Jamin, J. Fernández-Mateos, K. Khan, A. Lampis, K. Eason, I. Huntingford, R. Burke, M. Rata, D. M. Koh, N. Tunariu, D. Collins, S. Hulkki-Wilson, C. Ragulan, I. Spiteri, S. Y. Moorcraft, I. Chau, S. Rao, D. Watkins, N. Fotiadis, M. Bali, M. Darvish-Damavandi, H. Lote, Z. Eltahir, E. C. Smyth, R. Begum, P. A. Clarke, J. C. Hahne, M. Dowsett, J. De Bono, P. Workman, A. Sadanandam, M. Fassan, O. J. Sansom, S. Eccles, N. Starling, C. Braconi, A. Sottoriva, S. P. Robinson, D. Cunningham, and N. Valeri, “Patient-derived organoids model treatment response of metastatic gastrointestinal cancers,” *Science (80-.).*, vol. 359, no. 6378, pp. 920–926, 2018.

[229] N. Sachs, J. de Ligt, O. Kopper, E. Gogola, G. Bounova, F. Weeber, A. V. Balgobind, K. Wind, A. Gracanin, H. Begthel, J. Korving, R. van Boxtel, A. A. Duarte, D. Lelieveld, A. van Hoeck, R. F. Ernst, F. Blokzijl, I. J. Nijman, M. Hoogstraat, M. van de Ven, D. A. Egan, V. Zinzalla, J. Moll, S. F. Boj, E. E. Voest, L. Wessels, P. J. van Diest, S. Rottenberg, R. G. J. Vries, E. Cuppen, and H. Clevers, “A Living Biobank of Breast Cancer Organoids Captures Disease Heterogeneity,” *Cell*, vol. 172, no. 1–2, p. 373–386.e10, 2018.

[230] J. HAGEMANN, C. JACOBI, M. HAHN, V. SCHMID, C. WELZ, S. SCHWENK-ZIEGER, R. STAUBER, P. BAUMEISTER, and S. BECKER, “Spheroid-based 3D Cell Cultures Enable Personalized Therapy Testing and Drug Discovery in Head and Neck Cancer,” *Anticancer Res.*, vol. 37, no. 5, pp. 2201–2210, 2017.

[231] R. Wang, G. C. Y. Chu, S. Mrdenovic, A. A. Annamalai, A. E. Hendifar, N. N. Nissen, J. S. Tomlinson, M. Lewis, N. Palanisamy, H. R. Tseng, E. M. Posadas, M. R. Freeman, S. J. Pandol, H. E. Zhau, and L. W. K. Chung, “Cultured circulating tumor cells and their derived xenografts for personalized oncology,” *Asian Journal of Urology*, vol. 3, no. 4. pp. 240–253, 2016.

[232] J. Jabs, F. M. Zickgraf, J. Park, S. Wagner, X. Jiang, K. Jechow, K. Kleinheinz, U. H. Toprak, M. A. Schneider, M. Meister, S. Spaich, M. Sütterlin, M. Schlesner, A. Trumpp, M. Sprick, R. Eils, and C. Conrad, “Screening drug effects in patient-derived cancer cells links organoid responses to genome alterations,” *Mol. Syst. Biol.*, vol. 13, no. 11, p. 955, 2017.

[233] M. Van De Wetering, H. E. Francies, J. M. Francis, G. Bounova, F. Iorio, A. Pronk, W. Van Houdt, J. Van Gorp, A. Taylor-Weiner, L. Kester, A. McLaren-Douglas, J. Blokker, S. Jaksani, S. Bartfeld, R. Volckman, P. Van Sluis, V. S. W. Li, S. Seepo, C. Sekhar Pedamallu, K. Cibulskis, S. L. Carter, A. McKenna, M. S. Lawrence, L. Lichtenstein, C. Stewart, J. Koster, R. Versteeg, A. Van Oudenaarden, J. Saez-Rodriguez, R. G. J. Vries, G. Getz, L. Wessels, M. R. Stratton, U. McDermott, M. Meyerson, M. J. Garnett, and H. Clevers, “Prospective derivation of a living organoid biobank of colorectal cancer patients,” *Cell*, vol. 161, no. 4, pp. 933–945, 2015.

[234] M. Zanoni, F. Piccinini, C. Arienti, A. Zamagni, S. Santi, R. Polico, A. Bevilacqua, and A. Tesei, “3D tumor spheroid models for in vitro therapeutic screening: A systematic approach to enhance the biological relevance of data obtained,” *Sci. Rep.*, vol. 6, 2016.

[235] E. Garralda, K. Paz, P. P. López-Casas, S. Jones, A. Katz, L. M. Kann, F. López-Rios, F. Sarno, F. Al-Shahrour, D. Vasquez, E. Bruckheimer, S. V. Angiuoli, A. Calles, L. A. Diaz, V. E. Velculescu, A. Valencia, D. Sidransky, and M. Hidalgo, “Integrated next-generation sequencing and avatar mouse models for personalized cancer treatment,” *Clin. Cancer Res.*, vol. 20, no. 9, pp. 2476–2484, 2014.

[236] S. Habu, H. Fukui, K. Shimamura, M. Kasai, Y. Nagai, K. Okumura, and N. Tamaoki, “In vivo effects of anti-asialo GM1. I. Reduction of NK activity and enhancement of transplanted tumor growth in nude mice.,” *J. Immunol.*, vol. 127, no. 1, pp. 34–8, 1981.

[237] W. H. Sun, J. K. Burkholder, J. Sun, J. Culp, J. Turner, X. G. Lu, T. D. Pugh, W. B. Ershler, and N. S. Yang, “In vivo cytokine gene transfer by gene gun reduces tumor growth in mice,” *Proc.Natl.Acad.Sci.U.S.A*, vol. 92, no. 7, pp. 2889–2893, 1995.

[238] C. A. O’Brien, A. Pollett, S. Gallinger, and J. E. Dick, “A human colon cancer cell capable of initiating tumour growth in immunodeficient mice,” *Nature*, vol. 445, no. 7123, pp. 106–110, 2007.

[239] Food and Drug Administration, *Approved Drug Products with Therapeutic Equivalence Evaluations*. 2017.

[240] A. Quintás-Cardama and J. Cortes, “Therapeutic options against BCR-ABL1 T315I-positive chronic myelogenous leukemia,” *Clinical Cancer Research*, vol. 14, no. 14. pp. 4392–4399, 2008.

[241] A. N. Serafini, S. J. Houston, I. Resche, D. P. Quick, F. M. Grund, P. J. Ell, A. Bertrand, F. R. Ahmann, E. Orihuela, R. H. Reid, R. A. Lerski, B. D. Collier, J. H. McKillop, G. L. Purnell, A. P. Pecking, F. D. Thomas, and K. A. Harrison, “Palliation of pain associated with metastatic bone cancer using samarium-153 lexidronam: a double-blind placebo-controlled clinical trial.,” *J. Clin. Oncol.*, vol. 16, no. 4, pp. 1574–1581, 1998.

[242] J. S. De Bono, S. Oudard, M. Ozguroglu, S. Hansen, J. P. MacHiels, I. Kocak, G. Gravis, I. Bodrogi, M. J. MacKenzie, L. Shen, M. Roessner, S. Gupta, and A. O. Sartor, “Prednisone plus cabazitaxel or mitoxantrone for metastatic castration-resistant prostate cancer progressing after docetaxel treatment: A randomised open-label trial,” *Lancet*, vol. 376, no. 9747, pp. 1147–1154, 2010.

[243] N. K. Aaronson, S. Ahmedzai, B. Bergman, M. Bullinger, A. Cull, N. J. Duez, A. Filiberti, H. Flechtner, S. B. Fleishman, J. C. J. M. D. Haes, S. Kaasa, M. Klee, D. Osoba, D. Razavi, P. B. Rofe, S. Schraub, K. Sneeuw, M. Sullivan, and F. Takeda, “The European organization for research and treatment of cancer QLQ-C30: A quality-of-life instrument for use in international clinical trials in oncology,” *J. Natl. Cancer Inst.*, vol. 85, no. 5, pp. 365–376, 1993.

[244] P. M. Ellis and R. Vandermeer, “Delays in the diagnosis of lung cancer,” *J. Thorac. Dis.*, vol. 3, no. 3, pp. 183–188, 2011.

[245] M. Simunovic, A. Gagliardi, D. McCready, A. Coates, M. Levine, and D. DePetrillo, “A snapshot of waiting times for cancer surgery provided by surgeons affiliated with regional cancer centres in Ontario,” *CMAJ*, vol. 165, no. 4, pp. 421–425, 2001.

[246] G. Mehta, A. Y. Hsiao, M. Ingram, G. D. Luker, and S. Takayama, “Opportunities and challenges for use of tumor spheroids as models to test drug delivery and

efficacy," *J. Control. Release*, vol. 164, no. 2, pp. 192–204, 2012.

[247] Z. Xu, Y. Gao, Y. Hao, E. Li, Y. Wang, J. Zhang, W. Wang, Z. Gao, and Q. Wang, "Application of a microfluidic chip-based 3D co-culture to test drug sensitivity for individualized treatment of lung cancer," *Biomaterials*, vol. 34, no. 16, pp. 4109–4117, 2013.

[248] K. Kwapiszewska, A. Michalczuk, M. Rybka, R. Kwapiszewski, and Z. Brzózka, "A microfluidic-based platform for tumour spheroid culture, monitoring and drug screening," *Lab Chip*, vol. 14, no. 12, pp. 2096–2104, 2014.

[249] Y. Chen, D. Gao, H. Liu, S. Lin, and Y. Jiang, "Drug cytotoxicity and signaling pathway analysis with three-dimensional tumor spheroids in a microwell-based microfluidic chip for drug screening," *Anal. Chim. Acta*, vol. 898, pp. 85–92, 2015.

[250] M. C. W. Chen, M. Gupta, and K. C. Cheung, "Alginate-based microfluidic system for tumor spheroid formation and anticancer agent screening," *Biomed. Microdevices*, vol. 12, no. 4, pp. 647–654, 2010.

[251] I. Bairati, L. Fillion, F. A. Meyer, C. Héry, and M. Larochelle, "Women's perceptions of events impeding or facilitating the detection, investigation and treatment of breast cancer," *Eur. J. Cancer Care (Engl).*, vol. 15, no. 2, pp. 183–193, 2006.

[252] K. Bright, M. Barghash, M. Donach, M. G. de la Barrera, R. J. Schneider, and S. C. Formenti, "The role of health system factors in delaying final diagnosis and treatment of breast cancer in Mexico City, Mexico," *The Breast*, vol. 20, pp. S54–S59, 2011.

[253] A. Thomas, J. Tan, and Y. Liu, "Characterization of nanoparticle delivery in microcirculation using a microfluidic device," *Microvasc. Res.*, vol. 94, pp. 17–27, 2014.

[254] C. G. Uhl, Y. Gao, S. Zhou, and Y. Liu, "The shape effect on polymer nanoparticle transport in a blood vessel," *RSC Adv.*, vol. 8, no. 15, pp. 8089–8100, 2018.

[255] Y. J. Byun, B.-B. Park, E. S. Lee, K. S. Choi, and D. S. Lee, "A case of chronic myeloid leukemia with features of essential thrombocythemia in peripheral blood and bone marrow," *Blood Res.*, vol. 49, no. 2, p. 127, 2014.

[256] C. L. Sawyers, "Chronic myeloid leukemia.," *N. Engl. J. Med.*, vol. 340, no. 17, pp. 1330–40, 1999.

[257] C. Sullivan, C. Peng, Y. Chen, D. Li, and S. Li, "Targeted therapy of chronic myeloid leukemia," *Biochemical Pharmacology*, vol. 80, no. 5. pp. 584–591, 2010.

[258] K. Kumano, S. Arai, M. Hosoi, K. Taoka, N. Takayama, M. Otsu, G. Nagae, K. Ueda, K. Nakazaki, Y. Kamikubo, K. Eto, H. Aburatani, H. Nakauchi, and M. Kurokawa, "Generation of induced pluripotent stem cells from primary chronic myelogenous leukemia patient samples," *Blood*, vol. 119, no. 26, pp. 6234–6242, 2012.

[259] J. Tan, S. Shah, A. Thomas, H. D. Ou-Yang, and Y. Liu, "The influence of size, shape and vessel geometry on nanoparticle distribution," *Microfluid. Nanofluidics*, vol. 14, no. 1–2, pp. 77–87, 2013.

[260] P. Vaupel, F. Kallinowski, and P. Okunieff, "Blood flow, oxygen and nutrient supply, and metabolic microenvironment of human tumors: a review.," *Cancer Res.*, vol. 49, no. 23, pp. 6449–65, 1989.

[261] A. Pluen, Y. Boucher, S. Ramanujan, T. D. McKee, T. Gohongi, E. di Tomaso, E. B. Brown, Y. Izumi, R. B. Campbell, D. A. Berk, and R. K. Jain, "Role of tumor-host interactions in interstitial diffusion of macromolecules: Cranial vs. subcutaneous tumors," *Proc. Natl. Acad. Sci.*, vol. 98, no. 8, pp. 4628–4633, 2001.

[262] L. T. Baxter and R. K. Jain, "Transport of fluid and macromolecules in tumors. I. Role of interstitial pressure and convection," *Microvasc. Res.*, vol. 37, no. 1, pp. 77–104, 1989.

[263] S. C. Ferreira, M. L. Martins, and M. J. Vilela, "Reaction-diffusion model for the growth of avascular tumor," *Phys. Rev. E. Stat. Nonlin. Soft Matter Phys.*, vol. 65, no. 2, p. 21907, 2002.

[264] G. M. Thurber, M. M. Schmidt, and K. D. Wittrup, "Antibody tumor penetration: Transport opposed by systemic and antigen-mediated clearance," *Advanced Drug Delivery Reviews*, vol. 60, no. 12. pp. 1421–1434, 2008.

[265] F. L. Meyskens, S. P. Thomson, and T. E. Moon, "Quantitation of the Number of Cells within Tumor Colonies in Semisolid Medium and Their Growth as Oblate Spheroids," *Cancer Res.*, vol. 44, no. 1, pp. 271–277, 1984.

[266] R. K. Jain and L. T. Baxter, "Mechanisms of heterogeneous distribution of monoclonal antibodies and other macromolecules in tumors: Significance of elevated interstitial pressure," *Cancer Res.*, vol. 48, pp. 7022–7032, 1988.

[267] M. Ingram, G. B. Techy, R. Saroufeem, O. Yazan, K. S. Narayan, T. J. Goodwin, and G. F. Spaulding, "GROWTH PATTERNS OF VARIOUS HUMAN TUMOR CELL LINES IN SIMULATED MICROGRAVITY OF A NASA BIOREACTOR," *Vitr. Cell. Dev. Biol.--Animal*, vol. 33, no. 77058, pp. 459–66, 1997.

[268] M. Mareel, J. Kint, and C. Meyvisch, "Methods of study of the invasion of malignant C3H-mouse fibroblasts into embryonic chick heart in vitro," *Virchows Arch. B Cell Pathol.*, vol. 30, no. 1, pp. 95–111, 1979.

[269] C. R. Thoma, M. Zimmermann, I. Agarkova, J. M. Kelm, and W. Krek, "3D cell culture systems modeling tumor growth determinants in cancer target discovery," *Advanced Drug Delivery Reviews*, vol. 69–70. pp. 29–41, 2014.

[270] Y. KIM, M. A. STOLARSKA, and H. G. OTHMER, "A HYBRID MODEL FOR TUMOR SPHEROID GROWTH IN VITRO: THEORETICAL DEVELOPMENT AND EARLY RESULTS," *Math. Model. Methods Appl. Sci.*, vol. 17, no. supp01, pp. 1773–1798, 2007.

[271] J. P. F. R. M. Sutherland, J. Freyer, and R. Sutherland, "Regulation of growth saturation and development of necrosis in EMT6/Ro multicellular spheroids by the glucose and oxygen supply," *Cancer Res.*, no. July, pp. 3504–3512, 1986.

Vita

Christopher Uhl was born to Bruce and Melinda Uhl on February 19th, 1991 in Allentown, PA. He attended King's College and obtained his Bachelor of Science degree in Biology with minors in Mathematics and Chemistry in 2013. He then joined Dr. Yaling Liu's group at Lehigh University to pursue his Doctoral degree in Bioengineering. His research was focused on the development of microfluidic devices designed to mimic blood vessels and cancer in an effort to study drug delivery.

EDUCATION:

Ph.D. in Bioengineering P.C. Rossin Engineering College, Lehigh University (2013.08 – 2018.08)

B.S. in Biology College of Biological Sciences, King's College (2009 – 2013)

PUBLICATIONS & PRESENTATIONS DURING PhD:

JOURNAL PAPERS:

C. Uhl, V. Muzykantov, Y. Liu, "Biomimetic microfluidic platform for the quantification of transient endothelial monolayer permeability and therapeutic transport under mimicked cancerous conditions", Biomicrofluidics, vol.12, no.1, 2018.

C. Uhl, Y. Gao, S. Zhou, Y. Liu, "The shape effect on polymer nanoparticle transport in a blood vessel", RSC Adv., vol.8, no.15, p.8089, 2018.

C. Uhl, W. Shi, Y. Liu, "Organ-on-Chip Devices towards Applications in Drug Development and Screening: A Review", Journal of Medical Devices, in press, 2018.

CG. Uhl, A Glaser, R. Becker, Y. Liu. Assessment of PEGylated cancer targeting solid lipid nanoparticles in a microfluidic device. In preparation.

W. Shi, S Wang, A Maarouf, **CG Uhl**, R He, D Yunus, Y Liu. "Magnetic particles assisted capture and release of rare circulating tumor cells using wavy-herringbone structured microfluidic devices," Lab Chip, vol. 17, no. 19, pp. 3291–3299, Sep. 2017.

W Shi, J Kwon, Y Huang, **C Uhl**, R He, Y Liu. "Facile tumor spheroids formation with controllable size in large quantity and high uniformity. Sci. Rep., vol. 8, Article number: 6837, May 2018.

R. He, D. Yunus, **C. Uhl**, W. Shi, S. Sohrabi, and Y. Liu, "Fabrication of circular microfluidic channels through grayscale dual-projection lithography," Microfluid. Nanofluidics, vol. 21, no. 1, p. 13, Jan. 2017.

J. Xu, J. Yang, N. Huang, **C. Uhl**, Y. Zhou, Y. Liu, "Mechanical response of cardiovascular stents under vascular dynamic bending", Biomed. Eng. Online, vol. 15, no. 1, p. 21, 2016.

K. Sirorattanakul, H. Huang, **C. Uhl**, D. Ou-Yang, "On Determination of the Equation of State of Colloidal Suspensions", in APS March Meeting, 2016.

W Shi, L Reid, **C Uhl**, R He, Y Liu. Bi-layered microfluidic devices for tumor drug screening based on 3D tumor spheroids. In preparation.

POSTER PRESENTATIONS:

Poster Presentation, Rossin College Doctoral Open House, "Biomimetic Microfluidic Device for Evaluation of Drug Delivery", March 2018, Lehigh University, Pennsylvania, USA

Poster Presentation, NJ Tech Council's Tech Day, "High-Speed All Dimensional 3D Printing", December 2016, Rutgers University, New Jersey, USA

Poster presentation, Life Sciences Future, "Microfluidic Chips for Drug Evaluation and Disease Diagnosis", October 2014, Philadelphia, PA, USA

Commercialization, NSF I-Corps, Entrepreneurial Lead for "Pharmaflux", January-February 2016, Newark, New Jersey, USA

SKILLS:

Interdisciplinary knowledge base: Biology, Microfluidics, MEMS/NEMS, Physiology, Chemistry, Molecular Biology, Chemical Engineering, Biochemistry, Oncology, Micro/Nano-Technology, Drug Delivery, 3D printing, Computational Modeling.

Software: MatLab, SolidWorks, ImageJ/FIGI, IBM SPSS Stats

Bio-related Skills: Immunofluorescent microscopy, Immunoaffinity Assay, confocal microscopy, Tumor cell isolation and growth, Cell culture, etc.

Characterization: Fluorescence, Confocal, UV-Vis, SEM, AFM, etc.

Applications: Microfluidic design and fabrication, nanoparticle fabrication and characterization, drug delivery characterization, computational modeling